Τμήμα Μαθηματικών & Εφαρμοσμένων Μαθηματικών

ΠΑΝΕΠΙΣΤΗΜΙΟ ΚΡΗΤΗΣ

University of Crete
Department of Mathematics and Applied Mathematics

PhD Thesis in Applied Mathematics

Velocity estimation using cross-correlations of ambient noise recordings.

'Θεωρητική και αριθμητική μελέτη του προβλήματος ανάκτησης μεταβολών της σχετικής ταχύτητας διάδοσης στο υπέδαφος με χρήση του θορύβου περιβάλλοντος'

Emmanouil Daskalakis

supervised by
Dr. Chrysoula Tsogka

Evaluation committee
Christos Evangelidis
Josselin Garnier
Vagelis Harmandaris
George Makrakis
George Papanicolaou
Michael Plexousakis
Chrysoula Tsogka

July 5, 2016

.

Abstract

The main subject of this thesis is the use of cross-correlations of noise recordings for estimating the velocity and the velocity variations in a medium. The cross-correlation function of the noise recordings at two sensor locations is related to the Green's function between these two sensors. This relation largely depends on the spatial distribution and the frequency content of the noise sources.

In part I we investigate how seasonal variations in the spatial distribution and the frequency content of the noise affect the measurement of the velocity variation in a medium and we suggest a possible treatment to that problem which works under some assumptions on the seasonal variations.

In part II we study the problem of velocity tomography using noise recordings. In particular we study the Eikonal Tomography and more specifically the impact that different interpolation schemes have on the estimation obtained by Eikonal tomography. We also introduce the Kriging interpolation method as an alternative approach to the classical deterministic methods.

In part III we use noise recordings (Structural Vibrations) from sensors positioned at a historic masonry bell-tower in Perugia for Structural Health Monitoring (SHM). We introduce a new method to detect changes in the natural frequencies of the structure which are associated with structural damage.

Περιγραφή

Το κυρίως θέμα αυτής της διατριβής είναι η χρήση της συσχέτισης καταγραφών θορύβου για την εκτίμηση της ταχύτητας και μεταβολών της ταχύτητας σε ένα μέσω. Η συνάρτηση συσχέτισης καταγραφών θορύβου σε δύο αισθητήρες έχει σχέση με τη συνάρτηση Green μεταξύ των δύο αισθητήρων. Αυτή η σχέση εξαρτάται από την κατανομή στον χώρο και στο συχνοτικό περιεχόμενο, των πηγών θορύβου.

Στο πρώτο μέρος μελετάμε πως εποχιακές μεταβολές στην κατανομή στο χώρο και στο συχνοτικό περιεχόμενο του θορύβου επηρεάζουν της μετρήσεις των μεταβολών της ταχύτητας ενός μέσου και προτείνουμε πιθανό τρόπο για να εξαλείψουμε αυτό την επηροή κάτω από ορισμένες προϋποθέσεις για τις εποχιακές μεταβολές.

Στο δεύτερο μέρος μελετάμε το πρόβλημα της απεικόνησης της ταχύτητας ενός μέσου χρησιμοποιώντας καταγραφές θορύβου. Συγκεκριμένα μελετάμε το πρόβλημα Eikonal Tomography. Επιπλέον εισάγουμε την μέθοδο παρεμβολής Kriging ως εναλακτική προσέγγιση στις παραδοσιακές ντετερμινιστικές μεθόδους παρεμβολής.

Στη τρίτο μέρος τέλος χρησιμοποιούμε καταγραφές θορύβου (δονήσεις κατασκευής) από αισθητήρες τοποθετημένοι σε Ιστορικό καμπαναριό στην Περούτζια για παρακολούθηση της κατάστασης της κατασκευής. Εισάγουμε μιά νέα μέθοδο που εντοπίζει αλλαγές στις φυσικές συχνότητες της κατασκευής οι οποίες συσχετίζονται με ζημιές στην κατασκευή.

.

Acknowledgments

First and foremost, I would like to express my deepest sense of Gratitude to my advisor Prof. Chrysoula Tsogka, who offered her continuous advice and encouragement throughout the course of this thesis. I thank her for the systematic guidance and great effort he put into training me in the scientific field.

A very special thanks goes out to Prof. George Papanicolaou and Prof. Josselin Garnier for their guidance and assistance they provided at all levels of the research projects. From the Institute of Geodynamics at the National Observatory of Athens I would like to deeply thank Dr. Christos Evangelidis and Dr Nikolaos Melis for the assistance and for helping me familiarize with geophysics and seismology and for a wonderful collaboration. From the University of Perugia I would like to thank Dr. Gabriele Comanducci and Prof. Filippo Ubertini for giving us the opportunity to work on a very interesting project during our collaboration in this thesis.

I am thankful to Prof. Vasileios Dougalis for his selfless support and encouragement given to me during the course of my master thesis at the University of Athens, in which I gain knowledge essential for my PhD studies later on.

I am also thankful to many people at the University of Crete and the FoRTH for their support throughout this last almost 4 years. Many thanks for my fellow graduate students.

I would like to thank the rest of my evaluation committee: Prof. Vagelis Harmandaris, Prof. George Makrakis, and Dr. Michael Plexousakis, for dedicating their valuable time serving as my committee members.

Finally, I take this opportunity to express the profound gratitude from my deep heart to my family for their love and continuous support – both spiritually and materially.

Contents

Chapter 1

Introduction

Getting information about key properties of the interior of a medium without placing sensors inside the medium is very useful and practical. Technological achievements from the simple X-ray (invented back in late 1800s) to the medical MRI (invented by Paul C. Lauterbur in 1971) are brilliant examples of the necessity to be able to "see" inside the human body without having to perform any kind of surgery. Back in the 1970s we were projecting that soon we will run out of oil, nowadays we have more fossil fuel than we really need and the reason for that is that we have developed new technologies for extracting these natural resources and most importantly we have radically improved the imaging techniques.

In the context of geophysics, imaging techniques have been developed which are used to monitor volcanoes and study the major earthquakes post-seismic effects in the velocity of the earth around the epicentre. Also, non-destructive testing of materials and structural health monitoring are areas where the scientific community has put a lot of effort. In all these examples the common denominator is the need to "see" inside a medium.

1.1 Imaging the subsurface of the Earth

In this thesis we consider the problem of imaging the subsurface velocity of the Earth. Up until the mid 1990s the basic configuration had two main components, the source and the receiver (see Figure 1.1). The source was usually an earthquake or a small explosion in the case of active imaging. A detailed image of the subsurface can be obtained as the different layers of the earth reflect the seismic wave that had been generated at the position of the source. The travel-time can be extracted and used to obtain a velocity estimation. This process usually requires a large number of sources and receivers.

In this thesis we are also interested to estimate velocity changes in a medium. Back in 1984 [52] introduces the 'doublet' method for comparing recordings of two earthquake events of similar magnitude and similar location, as recorded by a distant seismic station. The earthquakes had happened in different times and with the 'doublet' method it was possible to detect small changes in the velocity of seismic waves that happened in the time interval between the two earthquakes.

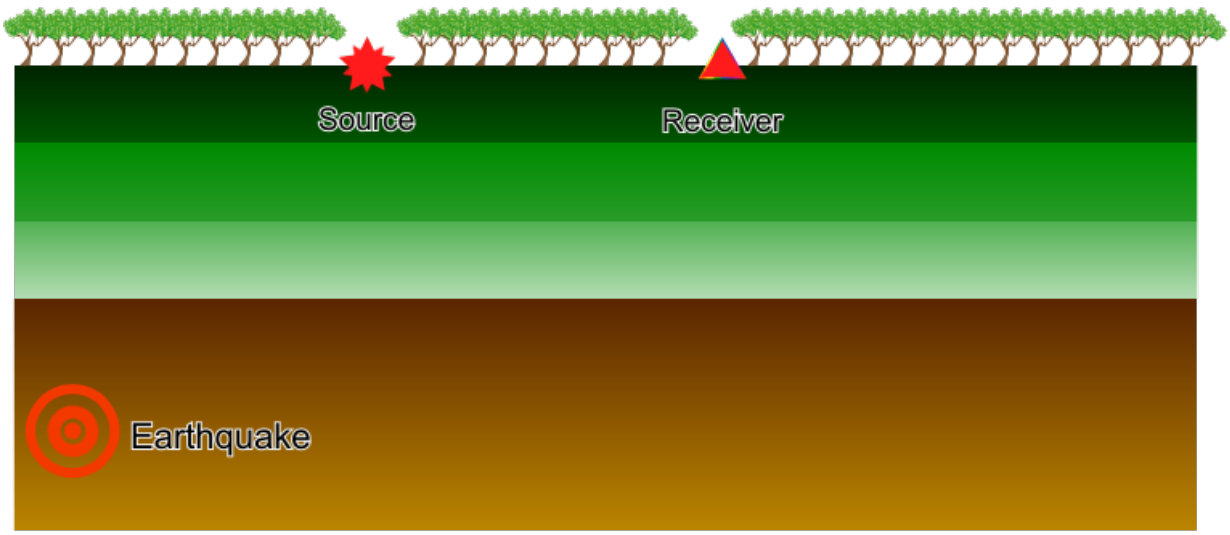

Figure 1.1: Active configuration: The basic configuration requires an array sources-receivers. The source can be an manmade seismic explosion or an earthquake.

In order to use the 'doublet' method to systematically monitor faults and volcanoes we would need earthquakes to occur quite often and at the same locations, which is not realistic. At mid 1990s an alternative approach to this problem resurfaced where seismic noise was being used.

1.1.1 Usage of noise data.

"Noise" in general isn't a good thing to have in your data and numerous studies and research has been carried out so as noise can be removed from the data. Seismic noise is generated mainly by ocean waves (frequencies below 1Hz) and by human activities such as road traffic (above 1Hz). The idea to use seismic noise to study ground properties is actually very old, dated back to 1950s [2] but the implementation of those ideas wasn't possible due to the low precision of the seismic stations at the time. Improvements in instrumentation in the mid 1990s led to the resurrection of those old ideas in the late 1990s.

In the configuration of Figure 1.1 the signal recorded at the receiver characterizes the propagation from the source to the receiver (this points to the Green's function from the source to the receiver). So the question is: can we reconstruct the Green's function in a "passive" configuration such as in Figure 1.2 where we no longer have source but we only have pairs of receivers that record the noise field?

The answer is positive, yes we can reconstruct the Green's function and this is achieved using the cross correlation function. Assuming noise recordings at receiver locations $\mathbf{x}_1$ and $\mathbf{x}_2$ and given a uniform distribution of noise sources and long enough recording time, it has

been shown that

$$\frac{\partial}{\partial \tau} C_T(\tau, \mathbf{x}_1, \mathbf{x}_2) \simeq G(\tau, \mathbf{x}_1, \mathbf{x}_2) - G(-\tau, \mathbf{x}_1, \mathbf{x}_2),$$

where T is the length of the recordings and C_T is the cross correlation function between the sensors at $\mathbf{x}_1$ and $\mathbf{x}_2$.

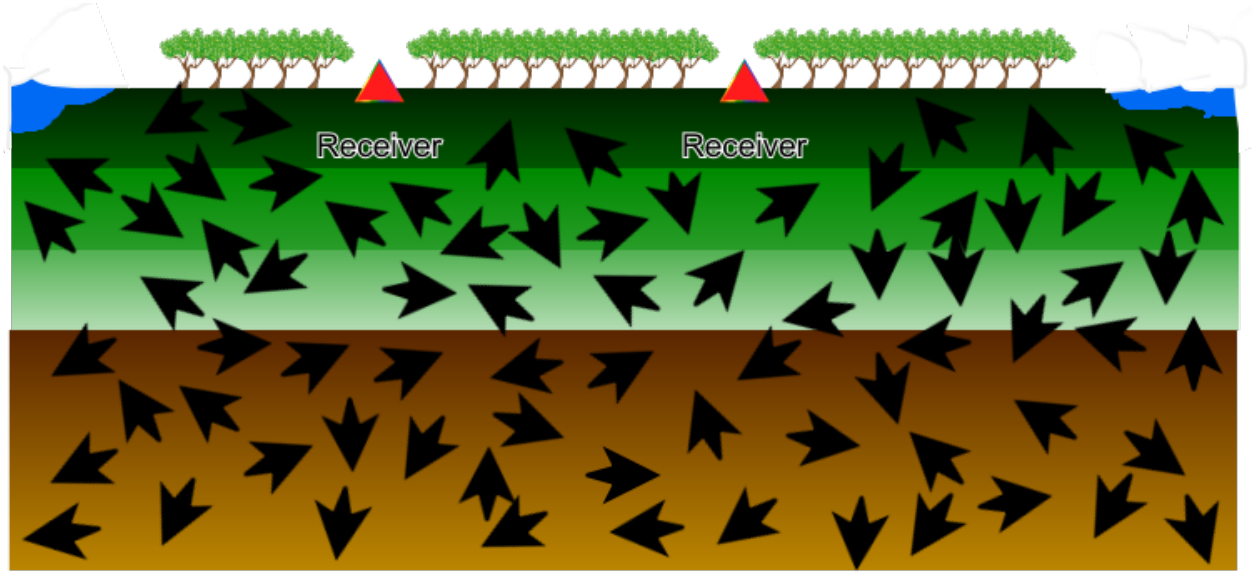

Figure 1.2: Passive configuration: This configuration requires the present of a seismic noise field.

The relation above is not an equality and requires a large recording time T, corresponding to several days or even sometimes months, in order for the cross correlation to converge to the symmetrized Green's function. However in order to obtain information about the travel-time or the velocity change, just a few days of recordings are usually enough.

The estimation of the velocity change in the medium is performed using two methods, the Stretching method (SM) and a modification of the 'doublet' method which is called Moving window cross spectral (MWCS) method. The methods are applied not on the recordings of the stations but in specially constructed cross correlation functions. These methods are introduced in detail at chapter 3.

The travel-time between the two receivers can be obtained by estimating the time at which the cross correlation function (or its envelop) has a peak. Given a network of sensors this will eventually produce all the pair-wise travel times which can be used for constructing a velocity map of the medium.

In part I we investigate how we can estimate velocity changes in a medium using cross correlations of noise recordings and the quality of that estimation regarding the spatial and frequency distribution of noise sources.

In part II we study the problem of velocity tomography using correlations of noise recordings between pairs of sensors in a network of sensors.

1.2 Noise signals in Structural Health Monitoring

The efficient management of aging infrastructure network, as well as the preventive conservation of civil structures and, in particular, of heritage ones, that are exposed to various natural and anthropogenic hazards, are stimulating scientific research towards the development of automated structural condition assessment strategies. Similar strategies are commonly referred to as Structural Health Monitoring (SHM) systems, whose main goal is using field observations of the response of a structure in operational conditions for damage diagnosis and health prognosis [28].

Several strategic bridges worldwide are equipped with SHM systems [10, 44], while in application to historic structures, challenges related to invasiveness and architectural respect, as well as to the choice of the proper sensing hardware and signal processing strategies still need to be addressed. Several authors worldwide are working to overcome these challenges by developing appropriate tools for SHM of monumental buildings. Among the most relevant applications, one can mention historic bridges [7], monumental buildings [13, 55] and masonry towers [40, 34].

Among the various approaches available for SHM, vibration-based strategies are especially popular, owing to their fully non-destructive and global nature. Many vibration-based SHM tools look for anomalies in modal parameters, typically natural frequencies, whose estimates are continuously extracted from monitoring data using automated output only modal analysis techniques [3, 21, 45]. Similar approaches can benefit of reliable output only modal identification techniques currently available in the literature [46, 57, 67], modal tracking procedures [57] and statistical methods able to remove the effects of changing environmental conditions from identified modal frequencies [74, 75, 4] and to automatically detect anomalies in the frequency time series, possibly related to some structural damage [73, 74, 27, 45, 48, 19, 22, 17]. These techniques, however, can result in heavy computations that require a de-centralized computer that further complicates the real time early warning task. Therefore, the development of SHM tools that are less expensive in terms of computational cost is much needed at present, which can also allow implementation in smart sensors with embedded electronics.

In part III we proposes a novel vibration-based SHM method which is inspired by the Stretching method used in parts I and II and uses continuous recordings of monitoring data ensuing from a small number of sensors installed on site, and provides a direct measurement of changes in natural frequencies of the structure.

Chapter 2

The Wave Equation and the Cross-Correlation Function

In this chapter, we first briefly recall some material about the wave equation and the Green's function. We also introduce the cross-correlation function of noisy recordings at two points and review the basic results that establish its relation with the Green's function between the two points. In this Thesis what we call "noise" is typically a seismic wave that travels through the medium which we desire to study. We call it noise because it is due to microseismic activity caused by natural phenomena, such as the interaction of water waves with the coast and it is of small amplitude.

2.1 The Wave Equation and its Green's function

To model the propagation of seismic waves we consider the wave equation in an inhomogeneous medium:

$$\frac{1}{c(\mathbf{x})}\frac{\partial^2 u(\mathbf{x},t)}{\partial t^2} - \Delta_{\mathbf{x}} u(\mathbf{x},t)) = n(\mathbf{x},t), \quad \mathbf{x} \in \mathbb{R}^d \tag{2.1}$$

where $u(\mathbf{x},t)$ denotes the pressure at point $\mathbf{x}$ in time t, $c(\mathbf{x})$ is the propagations speed in the medium and $n(\mathbf{x},t)$ is the noise source function. To precisely model the wave propagation of seismic waves in the Earth we should use the three dimensional elastic wave equation, we however use the simplified acoustic wave equation.

The noise sources are modelled by $n(\mathbf{x},t)$, which is a zero mean, stationary random process with correlation function:

$$E\{n(\mathbf{x}_1,t_1)n(\mathbf{x}_2,t_2)\} = \mathcal{F}(t_1-t_2)K(\mathbf{x}_1)\delta(\mathbf{x}_1-\mathbf{x}_2), \tag{2.2}$$

where $K(\mathbf{x})$ characterizes the spatial support of the sources, which are very often considered to be point sources ($K(\mathbf{x}_1) = \delta(\mathbf{x}_1)$). The time distribution of the noise is characterized by the correlation function $\mathcal{F}$.

In the case of a homogeneous medium ($c(\mathbf{x}) = c_0$) we can express the solution of (2.1) using the Green's function, which in two dimensions is given (in the frequency domain) by

$$\hat{G}(\omega, \mathbf{x}, \mathbf{y}) = \frac{i}{4} H_0^{(1)}(\omega \frac{|\mathbf{x} - \mathbf{y}|}{c_0}), \tag{2.3}$$

where $H_0^{(1)}$ is the Hankel function of first type and zero order and $\hat{}$ denotes the Fourier transform. In three dimensions the Green's function is given by

$$\hat{G}(\omega, \mathbf{x}, \mathbf{y}) = \frac{1}{4\pi|\mathbf{x} - \mathbf{y}|} e^{i\frac{\omega}{c_0}|\mathbf{x}-\mathbf{y}|}. \tag{2.4}$$

The solution of (2.1) can be now written as

$$u(\mathbf{x}, t) = \int\int n(\mathbf{y}, t - s) G(s, \mathbf{x}, \mathbf{y}) ds dy, \tag{2.5}$$

where $G(t, \mathbf{x}, \mathbf{y})$ is the Green's function in the time domain or else the inverse Fourier transform of (2.3) or (2.4).

2.2 The cross correlation function

In the case of an inhomogeneous medium we can't have the Green's function in an explicit form. Instead we can retrieve information about the Green's function using the cross correlation function. Considering $u(\mathbf{x}_1, t)$ and $u(\mathbf{x}_2, t)$ to be the solution of (2.1) as recorded by two sensors at positions $\mathbf{x}_1$ and $\mathbf{x}_2$, then the empirical cross correlation function is given by

$$C_T(\tau, \mathbf{x}_1, \mathbf{x}_2) = \int_0^T u(\mathbf{x}_1, t) u(\mathbf{x}_2, t + \tau) dt, \tag{2.6}$$

where T is the length in time of the two solutions. The empirical cross correlation function is a statistical stable quantity meaning that for large T it is independent of the realization of the noise sources with respect to the distribution of the sources. In particular in [29] it is proved the following proposition (Proposition 4.1 in [29]).

Proposition 2.2.1 *1. The expectation of C_T (with respect to the distribution of the sources) is independent of T:*

$$E\{C_T(\tau, \mathbf{x}_1, \mathbf{x}_2)\} = C^{(1)}(\tau, \mathbf{x}_1, \mathbf{x}_2), \tag{2.7}$$

where $C^{(1)}$ is given by

$$C^{(1)}(\tau, \mathbf{x}_1, \mathbf{x}_2) = \int dy \int d\omega \overline{\hat{G}}(\omega, \mathbf{x}_1, \mathbf{y}) \hat{G}(\omega, \mathbf{x}_1, \mathbf{y}) \hat{\mathcal{F}}(\omega) e^{-i\omega\tau} K(\mathbf{y}). \tag{2.8}$$

2. The empirical cross correlation C_T is a self-averaging quantity:

$$C_T(\tau, \mathbf{x}_1, \mathbf{x}_2) \xrightarrow{T\to\infty} C^{(1)}(\tau, \mathbf{x}_1, \mathbf{x}_2), \tag{2.9}$$

in probability with respect to the distribution of the sources. More precisely, the fluctuations of C_T around its mean value $C^{(1)}$ are of the order $T^{-1/2}$ for T large compared to the decoherence time of the sources.

The implications of this proposition are crucial. First (2.9) implies that for large T the empirical cross correlation converges to the statistical cross correlation $C^{(1)}$. Also (2.8) suggests that there is a connection between the cross correlation C_T and the Green's function which we will study in section 2.3. In geophysics there is a priori no information about the Green's function since we regard the earth as a complex inhomogeneous medium. The only information we usually have is the solution of (2.1) in a limited number of points and using the cross correlation function we can extract information about the Green's function between the given points. We will also investigate how the information we extract is useful in order to make estimations about the velocity or changes in the velocity of the medium.

2.3 The relation between the Green's function and the cross correlation function

To investigate the relation between the cross correlation and the Green's function of the wave equation we begin with the simpler case, which is the homogeneous medium case with the most generous conditions about the noise sources: We assume that the sources are a space-time stationary random field that is delta correlated in space and time (more general cases have been considered in [29]). Then it has been shown that

$$\frac{\partial}{\partial\tau}C_T(\tau,\mathbf{x}_1,\mathbf{x}_2)\simeq G(\tau,\mathbf{x}_1,\mathbf{x}_2)-G(-\tau,\mathbf{x}_1,\mathbf{x}_2), \tag{2.10}$$

where T is sufficient large. That means that the derivative of the cross correlation function will converge, for large enough T, to the symmetrized Green's function given a uniform distribution of sources.

To illustrate this, let us set up the following experiment: we distribute the sources on a circle of radius of 25Km and we locate two sensors 10 Km apart as we can see at Figure 2.1

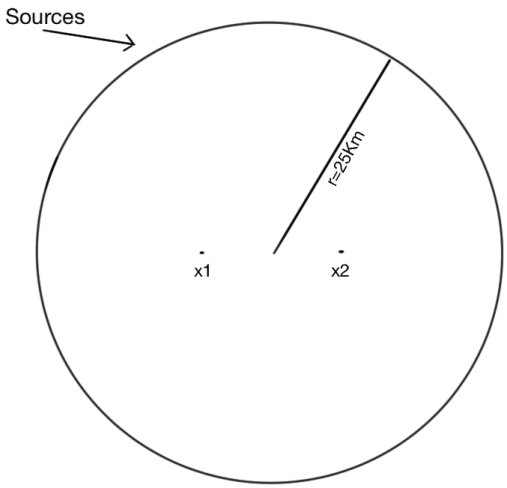

Figure 2.1: Location of the noise sources on a circle, $\mathcal{C}$, of radius 25Km and the two receivers at $\mathbf{x}_1$ and $\mathbf{x}_2$. The distance between the two receivers is 10Km.

In addition we assume that the background medium is homogeneous with velocity $1Km/s$. The cross correlation function of the recordings at $\mathbf{x}_1$ and $\mathbf{x}_2$ is expected to have two peaks, one at the time that corresponds to the travel-time between the two sensors and another peak at negative the travel-time between the two sensors. In the case of a an inhomogeneous medium we expect the same behaviour with a more noisy time series due to multiple scattering. In Figure 2.2 we can see a comparison of these two cases.

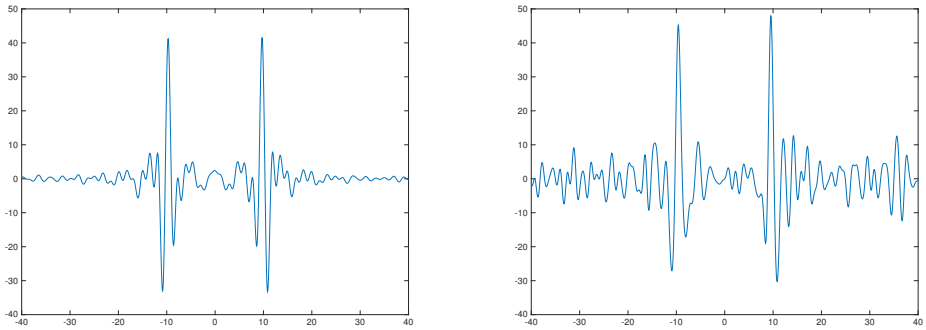

Figure 2.2: In the left we can see the cross correlation function in a homogeneous medium and in the right we can see the cross correlation function obtained in an inhomogeneous medium.

Now we consider the inhomogeneous medium and we will use sources located at preselected locations of the circle as it is showed in Figure 2.3.

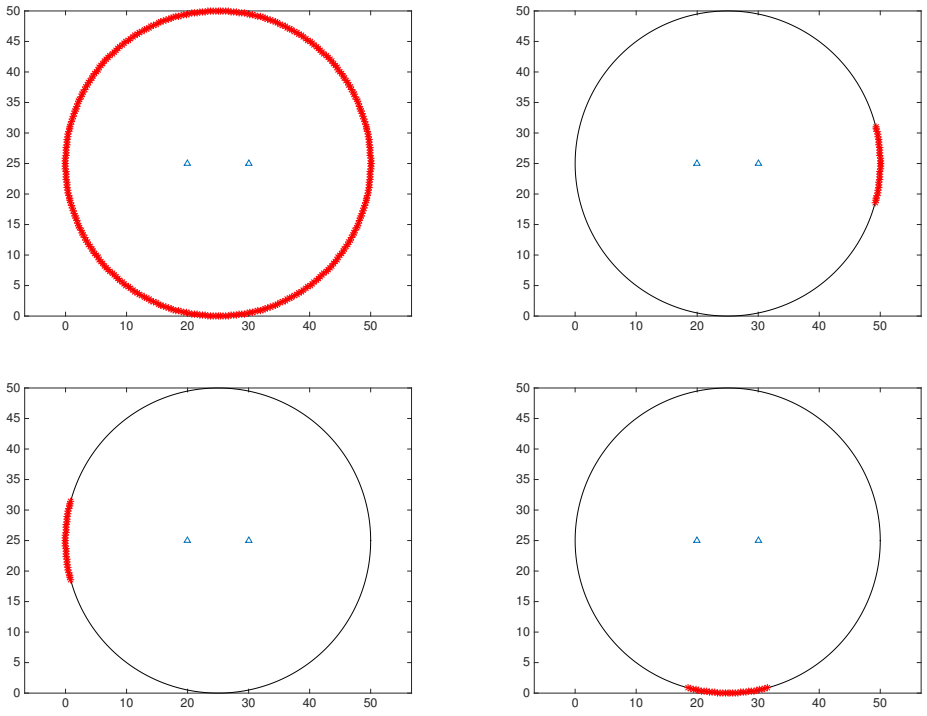

Figure 2.3: Case 1 (Up Left): The sources are located at all directions on the circle. Case 2 (Up Right): The sources are located on a 30 degree arc at the right side of the circle. Case 3 (Down Left): The sources are located on a 30 degree arc at the left side of the circle. Case 4 (Down Right): The sources are located on a 30 degree arc at the bottom part of the circle.

We study four cases and we want to investigate when we can retrieve information about the Green's function between the two receivers depending on the direction from where the noisy field is emanating (sources location). A stationary phase analysis [29] suggests that the we can recover some information about the Green's function only when the ray that connects that two receivers extends into the source region. As we can see in Figure 2.4 if the distribution of sources is uniform then we observe both peaks. Only one of the peaks can be recovered when the sources are located at the same direction as the orientation of the receivers (Case 2 and 3). As it is expected in the last case (Case 4) we are unable to retrieve any of the two peaks.

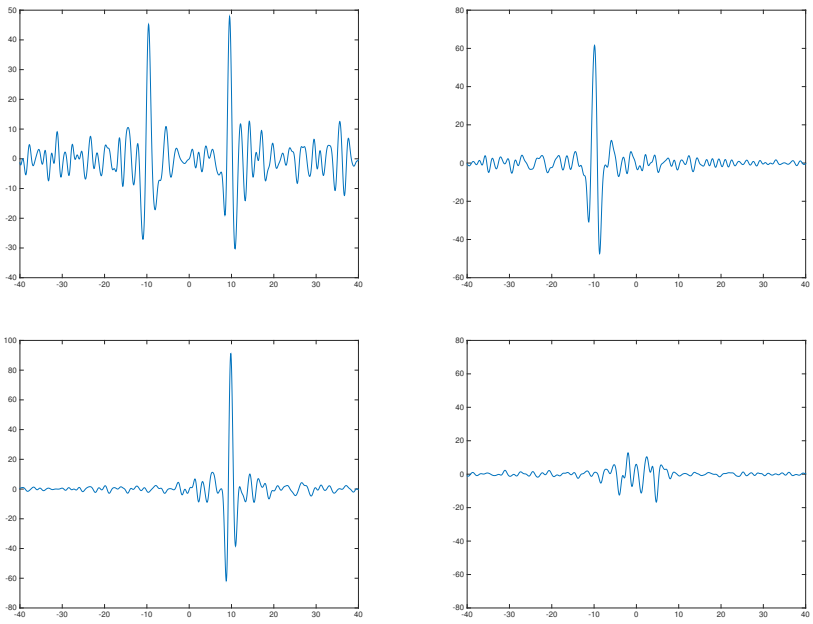

Figure 2.4: The cross correlation functions that corresponds to the distribution of sources of Figure 2.3.

2.3.1 Cross correlations from real data.

We will use now real data from two seismic stations to see how a cross correlation behaves. The two stations (see Figure 2.5) are located on two Aegean islands, Naxos and Santorini, the inter station distance is about 78Km.

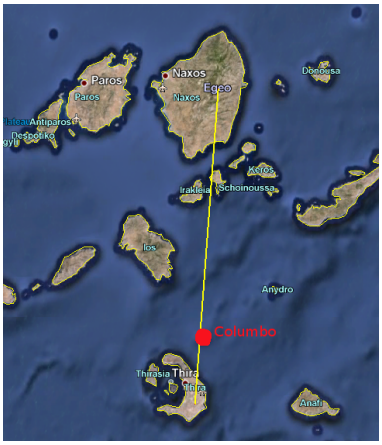

Figure 2.5: The stations in Naxos and Santorini. The inter station path pass over the underwater volcano Columbo.

After we filtered the data on the band $[0.2 \;\; 0.4]Hz$ we compute the daily cross correlations for several periods and then average. In Figure 2.6 we can see the cross correlation computed for three different periods. We observe that the cross correlation is different depending on the season. That phenomenon could be the result of different distribution of sources due to weather conditions and we will investigate in depth this phenomenon in Section 4.1.

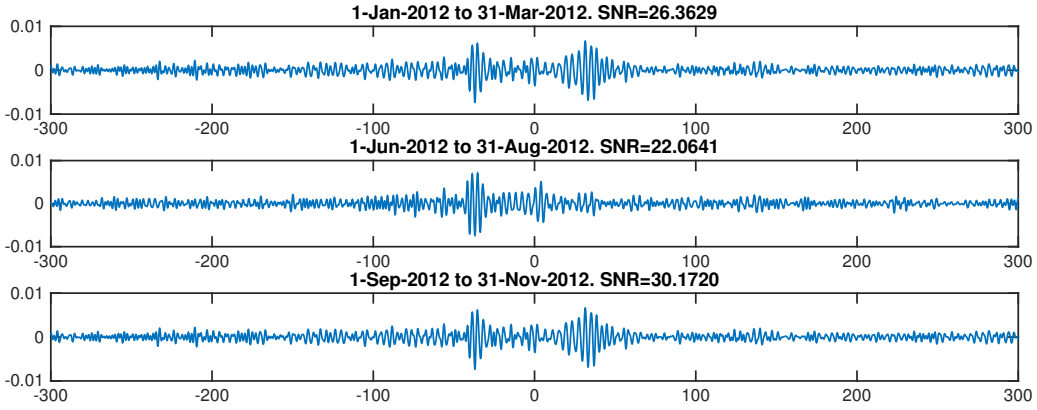

Figure 2.6: Cross-correlation function between the two stations. From top to bottom the season changes from winter to summer and fall. .

Part I

Estimating Velocity changes

Chapter 3

The MWCS and the Stretching method

Two methods have been predominately used for estimating velocity variations in the earth's crust: the Stretching Method (SM) and the Moving Window Cross-Spectral (MWCS) method [15]. In both methods, relative changes in the velocity of the medium are estimated by comparing two waveforms: the reference and the current cross-correlation functions which are obtained by cross-correlating the signals recorded at two different receivers over a certain period of time. The reference cross-correlation is usually the average of the daily cross-correlations over a long period of time of the order of a year. The current cross-correlation is a local average of the daily cross-correlation over a few days.

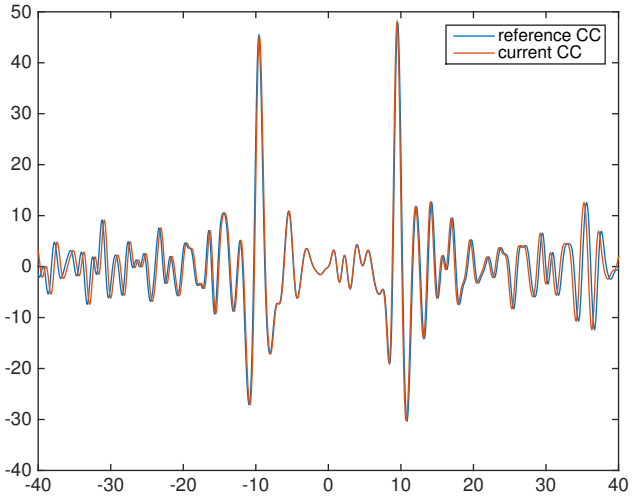

Figure 3.1: Reference cross correlation function in blue and an artificially stretched (-1%) version of it in red, so called current cross correlation function.

3.1 Stretching Method

The Stretching method (SM) has recently gained a lot of popularity as a method for measuring dv/v changes using cross correlation functions of seismic noise recordings. SM computes the stretching parameter that maximizes the correlation coefficient between two waveforms in a pre-selected time window $[t_1, t_2]$,

$$C(\epsilon) = \frac{\int_{t_1}^{t_2} CC_{c,\epsilon}(t) CC_r(t) dt}{\sqrt{\int_{t_1}^{t_2} (CC_{c,\epsilon}(t))^2 dt} \sqrt{\int_{t_1}^{t_2} (CC_r(t))^2 dt}}. \tag{3.1}$$

Here $CC_r(t)$ denotes the reference quantity and $CC_c(t)$ the current one, while $CC_{c,\epsilon}(t) = CC_c(t(1+\epsilon))$ is the stretched version of $CC_c(t)$. The time window $[t_1, t_2]$ is usually selected so as to contain the coda part of the cross-correlation function and not the first arrival.

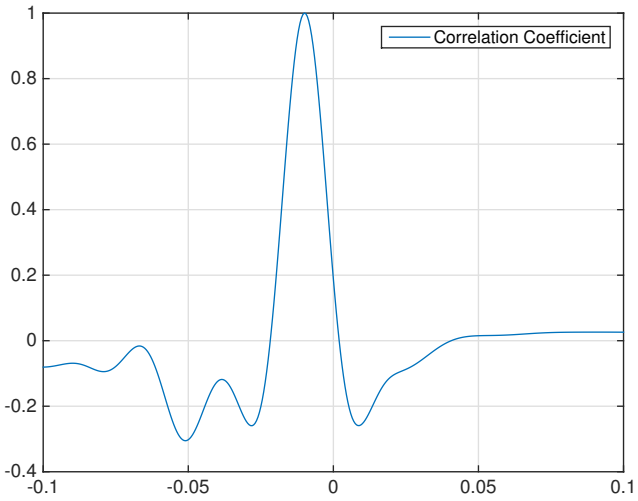

Figure 3.2: The correlation coefficient ($C(\epsilon)$) of the cross correlation functions of Figure 3.1. We observe that the correlation coefficient admits its maximum at 0.01 which corresponds to the 1% artificial inserted dv/v. NOTE: The maximum in practice is attained at a single point but usually corresponds to a value less than one.

We search the stretching parameter ϵ in an interval $[\epsilon_1, \epsilon_2]$, with a rough initial discretisation, after finding ϵ_0 that maximizes (3.1) we refine our search in a smaller region around ϵ_0 with a smaller discretisation. We repeat the refinement process until we archieve the desired accuracy, *i.e.*, until the discretisation is sufficiently small.

3.2 MWCS Method

The MWCS is widely used in signal processing in order to compute the time shift dt between a signal and a delayed version of the same signal. The MWCS method operates in the frequency domain. The idea is very simple, as the velocity of the medium changes any signal that propagates through the medium will appear to have a slightly different phase. The MWCS method can detect and use this small change in phase to extract the velocity variation in the propagation medium. The MWCS method is described in detail in [15] and basically consists in computing time delays (dt_i) in different time windows and then estimating dt/t using a linear regression model. The relative velocity change in the medium is deduced by the relationship $dv/v = -dt/t$. The estimation of the time delays dt_i between the reference and the current cross-correlation is performed by computing phase differences in the frequency domain.

We divide each cross-correlation function into N_w windows, with each window centered around time t_i, $i = 1, ..., N_w$. For each central time t_i we get a measurement dt_i using the corresponding windowed segments of CC_r and CC_c. Those segments after being window tapered, they are being fourier transformed and called $F_r(\nu) = \mathcal{F}(CC_r)$ and $F_c(\nu) = \mathcal{F}(CC_c)$ respectively. The Fourier transform is defined as,

$$(\mathcal{F}f)(\nu) = \int f(t)e^{i2\pi\nu t}dt.$$

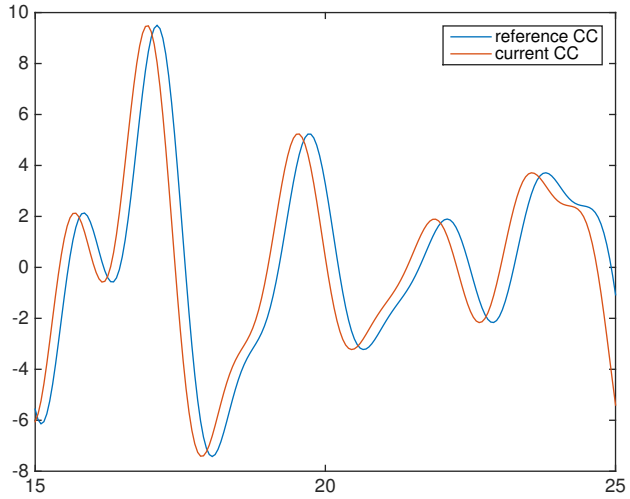

Figure 3.3: The windowed, sections of the cross-correlations at Figure 3.1.

Then the cross-spectrum is calculated as

$$X(\nu) = F_r(\nu)\ F_c^*(\nu), \tag{3.2}$$

and the cross-coherence as

$$C(\nu) = \frac{|\overline{X(\nu)}|}{\sqrt{|\overline{F_r(\nu)}|^2 |\overline{F_c(\nu)}|^2}}. \tag{3.3}$$

Here * denotes complex conjugate and overline denotes that the signal have passed from a Hanning window. Then we confine the frequency in the bandwidth of interest and we estimate the time delay of the two signals from the phase of the cross-spectrum $\phi_i(\nu)$,

$$\phi_i(\nu_j) = 2\pi \ \delta t_i \ \nu_j, \tag{3.4}$$

with δt_i the time shift corresponding to the central time t_i of the i^{th} window and where ν_j are the frequencies of interest, $j = 1, \ldots, N_w$.

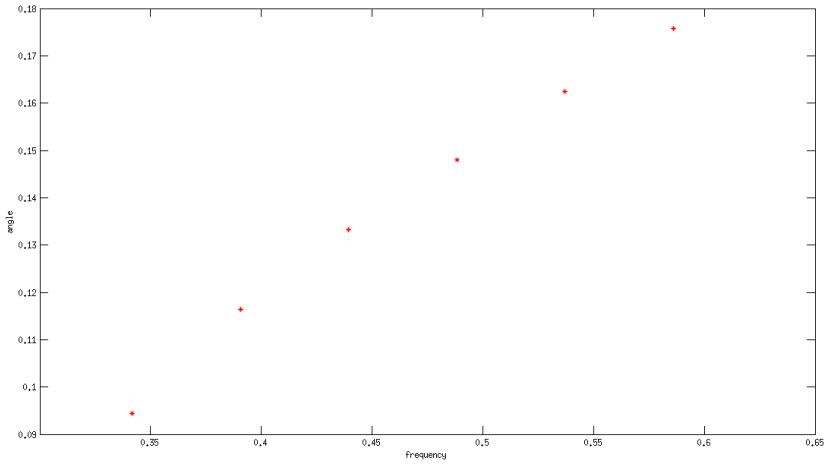

Figure 3.4: The phase of the cross spectrum at the frequency range of interest.

The time shift δt_i is estimated using a weighted least squares inversion,

$$\delta t_i = \frac{1}{2\pi} \frac{\sum_j w_j \nu_j \phi_i(\nu_j)}{\sum_j w_j \nu_j^2}, \tag{3.5}$$

with the weights w_j defined by,

$$w_j = \sqrt{\frac{C(\nu_j)^2}{1 - C(\nu_j)^2} \sqrt{|X(\nu_j)|}}. \tag{3.6}$$

The error $e_{\delta t_i}$ associated with the measurement for δt_i can be calculated by,

$$e_{\delta t_i} = \frac{1}{2\pi} \sqrt{\sum_j \left(\frac{w_j \nu_j}{\sum_i w_i \nu_i^2} \right)^2 \frac{\sum_j (\phi_i(\nu_j) - 2\pi \delta t_i \nu_j)^2}{N_\nu - 1}}, \tag{3.7}$$

where N_ν is the length of the frequency vector for the frequencies of interest. After we repeat the calculation for all the windows we gain N_w $(t_i, \delta t_i)$ couples. To calculate the slope $\delta t/t$ we apply another weighted linear regression using the weights: $p_i = 1/e^2_{\delta t_i}$. The resulting estimate is

$$\frac{\delta t}{t} = \frac{\sum_i p_i(t_i - \langle t \rangle)\delta t_i}{\sum_i p_i(t_i - \langle t \rangle)^2}, \tag{3.8}$$

with

$$\langle t \rangle = \frac{\sum_i p_i t_i}{\sum_i p_i}$$

Finally the velocity variation is just $\delta v/v = -\delta t/t$.

As we already said the data we used above are synthetic in the sense that the change in dv/v is artificially inserted. An example of the MWCS estimation for a measurement contacted in real data is presented at Figure 3.5.

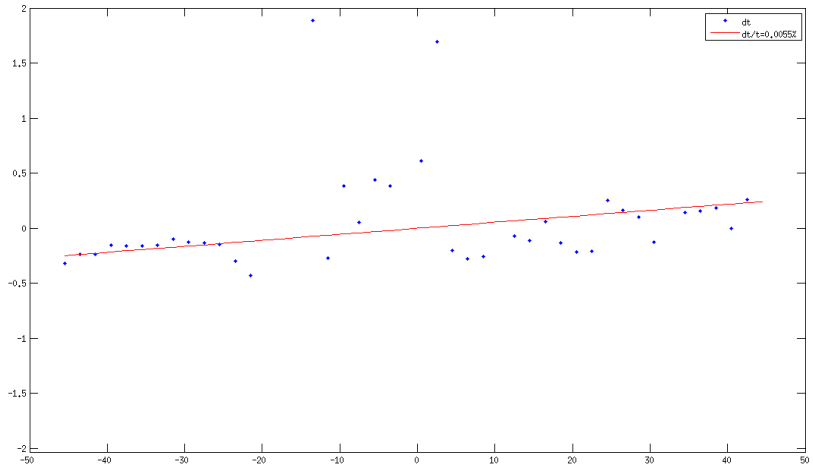

Figure 3.5: An example of the MWCS estimation for a real measurement.

3.3 Comparison of the two methods

The Stretching method and the MWCS method are fundamentally different in the way they produce the result of dv/v, the Stretching method operates in the time domain and so it is affected both by amplitude and phase changes, while the MWCS method operates in the frequency domain (measuring phase shifts and associates the change to δt measurement). Except from that the two methods have their advantages and their disadvantages.

The Stretching method is very simple, has an easy implementation, uses the whole coda part and it is more stable than MWCS. The disadvantage of the Stretching method is first of all that it assumes a homogeneous velocity change and by design can't resolve inhomogeneous

changes. In addition, if implemented poorly, it can become very slow. The bigger problem as we will see in the next chapter is the fact that since it operates in the time domain, it can be affected by variations at the amplitude of the noise sources.

On the other hand the MWCS method is very flexible, can potentially detect inhomogeneous velocity changes and since it operates in the frequency domain it is not affected by variations in the amplitude (at least not as much as the Stretching method). However the MWCS is more unstable than Stretching method, it requires more days of average for the current quantity and it is more difficult to operate for very low frequencies.

In practice the Stretching method used more often in studies with long inter-station distances and studies on earthquakes, while the MWCS is dominantly used in volcano monitoring studies.

Chapter 4

Estimating velocity changes in a medium

A version of this chapter has been published to Geophysics Journal International, entitled as "Robust seismic velocity change estimation using ambient noise recordings ".

We are interested in monitoring volcanic structures from temporal changes of the velocity of seismic waves. When magma pressure increases inside a volcano, the added pressure results into its inflation, and small cracks around the magma chamber will decrease the velocity of seismic waves. That small decrease in velocity can be detected using travel-time tomography of seismic waves and up until very recently only the seismic waves generated by natural events like earthquakes could be used [52, 56, 37]. There are however limitations that make the use of such seismic events not suitable for monitoring, such as the repeat rate or the unknown source position. More recently ambient seismic noise recordings have been successfully used instead of seismic events [9, 24].

The idea exploited is that information about the Green's function, or the travel-time, between two seismic stations can be obtained from cross-correlations (CC) of ambient noise recordings [18, 59, 29, 68, 69]. A number of passive imaging studies based on this idea are now used in volcano monitoring [9, 24], in seismic fault studies [8, 1] and more generally in studying the structure of the crust [1, 14]. In the case of volcano monitoring, there are several studies concerning Piton de la Fournaise, which is a shield volcano on the eastern side of Reunion island in the Indian Ocean. The goal in this setting is to measure relative velocity changes (dv/v) of surface waves, which are precursors to specific events (volcanic eruptions). Two techniques have been used for dv/v measurements, the moving window cross spectral (MWCS) method [15] and the Stretching Method (SM).

Both MWCS and SM use two waveforms, the reference and the current CC functions which are obtained by averaging daily CC functions over a large, respectively a small, period of time. Changes in the velocity of the medium are estimated from differences in these two CC functions. In MWCS, dv/v is obtained by estimating the time delays dt_i in different time windows. The time delay estimation is performed in the frequency domain using the cross spectrum of the windowed wavefront segments. Then $dv/v(= -dt/t)$ is computed using

a linear regression approach. SM operates in the time domain by solving an optimization problem which determines the stretching parameter that maximizes the correlation between the two waveforms.

A comparison between the SM and MWCS was carried out in [39] where SM was found to be more stable with respect to additive δ-correlated noise in the data. A more detailed study of the accuracy of SM with respect to noise was presented in [70] where the authors derived an expression for the root mean square (rms) error of the apparent velocity variation due to noise. The noise in [70] is assumed stationary and the rms value can be used to distinguish between physical and erroneous velocity variations. In this paper we study the effect that the non-stationarity, *i.e.*, the seasonal variations, of the noise sources may have on the stretching method's estimation.

There are some factors such as the quality and the distribution of the noise sources that can affect the temporal resolution of the measurements. The volcano of Piton de la Fournaise is a very well instrumented area with lots of high quality stations. Moreover the type of the volcano (shield volcano), which is erupting very frequently, makes it an ideal case for study. That is not so for many other volcanoes, especially for volcanic islands and "ring of fire volcanoes" which are often poorly instrumented and which erupt rarely. Another difficulty is that in some cases, and especially in the case we will consider in this paper, the evolution of the volcano is very slow and therefore long term fluctuations such as seasonal variations [76, 47] can hide velocity variations that are actually related to volcanic activity.

4.1 Seasonal variations and the effectiveness of spectral whitening

In [76] it is argued that the seasonal variations in the cross-correlations and the estimated velocity as observed in [47] are caused by seasonal variations of the amplitude spectra of the ambient noise sources. Since SM operates directly in the time domain it is much more likely to be affected by those seasonal variations than the MWCS method which only relies on the phase spectra of the cross-correlations. The stability of MWCS to spatio-temporal variations of the noise sources is studied in [16]. It is shown that in scattering media azimuthal variations in the intensity distribution of the noise sources does not affect the MWCS measurement when the coda part of the cross-correlation is used. This is because the anisotropy of the noise sources is reduced by the multiple scattering of the waves by the medium inhomogeneities.

We present here a set of numerical simulations suggesting that indeed the stretching method can produce apparent velocity variations caused by seasonal spatio-temporal fluctuations of the amplitude spectra of the noise sources. These variations are reduced by considering the coda part of the cross-correlations but they still persist. When the seasonal fluctuations are uniform with respect to the noise source locations, an hypothesis that is reasonable when the measurements are from the same area, the apparent velocity variations can be effectively removed by an adequate normalization (spectral whitening) of the

cross-correlated signals. Our approach significantly improves the signal to noise ratio of the stretching method as illustrated by numerical simulations and real measurements.

By measuring velocity variations for a long enough period using the stretching method in [47], small seasonal variations were observed, which were attributed to hydrological and thermoelastic variations. In contrast, [76] suggest that such variations are not necessarily due to changes in the medium and could be caused by seasonal fluctuations in the amplitude spectra of the noise sources. We investigate here this question using numerically simulated data, as well as seismic noise recordings. Let us first briefly review the MWCS and the SM methods.

4.1.1 The numerical model

We carry out a set of numerical simulations that are based on a mathematical model of wave propagation. In our numerical model we consider the acoustic wave equation:

$$\frac{1}{c(\mathbf{x})^2}\frac{\partial^2 u}{\partial t^2}(t,\mathbf{x}) - \Delta_{\mathbf{x}} u(t,\mathbf{x}) = n(t,\mathbf{x}), \tag{4.1}$$

where $n(t,\mathbf{x})$ models the noise sources which are located on a circle, $\mathcal{C}$, of radius 25km as illustrated in Figure 4.1. We assume that the wave field is recorded at two receivers $\mathbf{x}_1 = (-5,0)$km and $\mathbf{x}_2 = (5,0)$km.
The function $n(t,\mathbf{x})$ in equation (4.1) models the noise sources. We assume that it is a zero-mean random process. We also assume that the process is stationary in time with a covariance function that is delta correlated in space. Therefore, the covariance function of the noise sources has the form

$$\langle n(t_1,\mathbf{y}_1), n(t_2,\mathbf{y}_2)\rangle = \Gamma(t_2 - t_1, \mathbf{y}_1)\delta(\mathbf{y}_2 - \mathbf{y}_1). \tag{4.2}$$

Here $\langle\cdot\rangle$ stands for statistical averaging. The function $t \to \Gamma(t,\mathbf{y})$ is the time correlation function of the noise signals emitted by the noise sources at location $\mathbf{y}$. The Fourier transform $\omega \to \hat{\Gamma}(\omega,\mathbf{y})$ is their power spectral density (by Wiener-Khintchine theorem). The function $\mathbf{y} \to \Gamma(0,\mathbf{y})$ characterizes the spatial support of the sources. In our case we assume that the sources are uniformly distributed on a circle $\mathcal{C}$ of radius $R_{\mathcal{C}} = 25$km as illustrated in Figure 4.1:

$$\Gamma(t,\mathbf{y}) = \frac{1}{2\pi R_{\mathcal{C}}}\Gamma_0(t,\mathbf{y})\delta_{\mathcal{C}}(\mathbf{y}).$$

The solution of (4.1) at a given point $\mathbf{x}$ can be written as,

$$u(t,\mathbf{x}) = \int\int G^j(t-s,\mathbf{x},\mathbf{y})n(s,\mathbf{y})d\mathbf{y}ds, \tag{4.3}$$

or equivalently in the frequency domain,

$$\hat{u}(\omega,\mathbf{x}) = \int \hat{G}^j(\omega,\mathbf{x},\mathbf{y})\hat{n}(\omega,\mathbf{y})d\mathbf{y}. \tag{4.4}$$

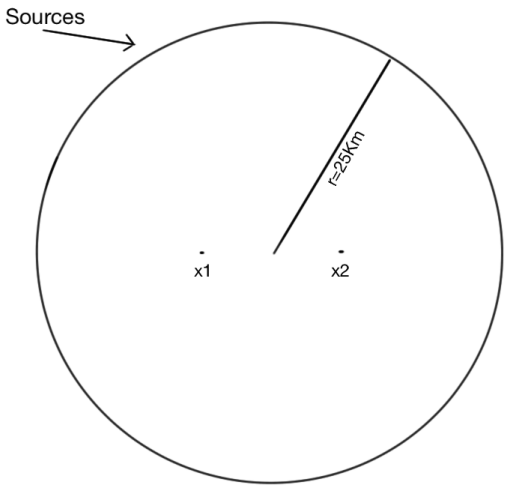

Figure 4.1: Location of the noise sources on a circle, $\mathcal{C}$, of radius 25Km and the two receivers at $\mathbf{x}_1$ and $\mathbf{x}_2$. The distance between the two receivers is 10Km.

Here j denotes the dependence on the day, hat denotes the Fourier transform and $\hat{G}^j(\omega, \mathbf{x}, \mathbf{y})$ is the Green's function. For simplicity of the computation we consider first a homogeneous medium in which case $\hat{G}^j(\omega, \mathbf{x}, \mathbf{y})$ is given by

$$\hat{G}^j(\omega, \mathbf{x}, \mathbf{y}) = \frac{1}{4\pi|\mathbf{x}-\mathbf{y}|} e^{i\frac{\omega}{c^j}|\mathbf{x}-\mathbf{y}|}. \tag{4.5}$$

In (4.5), we use the 3d expression for the Green's function of the wave equation instead of the Hankel function. In our setup the distance between the receivers is relatively large with respect to the wavelength so this does not affect the results since we are interested in the phase of the Green's function. In (4.5), the velocity is allowed to change as a function of time on the scale of a day. We denote by c^j the homogeneous velocity of the medium on day j. To illustrate the generality of our approach we also consider inhomogeneous scattering media for which the Green's function $\hat{G}^j(\omega, \mathbf{x}, \mathbf{y})$ is computed by solving numerically the wave equation (4.1) in the time domain using the code Montjoie (http://montjoie.gforge.inria.fr/).

Obtaining the time-series data at $\mathbf{x}_1$ and $\mathbf{x}_2$.

To obtain data at $\mathbf{x}_1$ and $\mathbf{x}_2$ we define the exact distribution and power spectral density of the sources. From now on we assume that the statistics of the noise sources change from one day to another and we denote by $\Gamma_0^j(t, \mathbf{y})$ its covariance function at day j. We take $N_s = 180$ point sources uniformly distributed on the circle $\mathcal{C}$ and then the equation (4.4) becomes

$$\hat{u}^j(\omega, \mathbf{x}) = \frac{1}{N_s} \sum_{i=1}^{N_s} \hat{G}^j(\omega, \mathbf{x}, \mathbf{y}_i) \hat{n}_i^j(\omega), \tag{4.6}$$

where $\hat{n}_i^j(\omega)$ is the frequency content of the noise sources at $\mathbf{y}_i$ during day j, which is random such that $\left\langle \hat{n}_i^j(\omega) \right\rangle = 0$ and

$$\left\langle \hat{n}_i^j(\omega)\overline{\hat{n}_i^j}(\omega') \right\rangle = 2\pi\hat{\Gamma}_0^j(\omega, \mathbf{y}_i)\delta(\omega - \omega').$$

At first we consider that the noise sources do not have any seasonal variations and therefore their power spectral density does not depend on j. Later on that will be changed according to the model of seasonal variations we want to study. In either case, the last step in order to obtain the time series recorded at location $\mathbf{x}$ is to apply the inverse Fourier transform to (4.6).

Reference and Current cross-correlation function

Our main tool, the daily cross-correlation function is given by

$$\mathrm{CC}^j(\tau, \mathbf{x}_1, \mathbf{x}_2) = \frac{1}{T}\int_0^T u^j(t+\tau, \mathbf{x}_1)u^j(t, \mathbf{x}_2)dt, \tag{4.7}$$

with $T = 24$ hours.
For both SM and MWCS methods, variations in the velocity are estimated by comparing two waveforms: the reference and the current cross-correlation functions. The reference cross-correlation is the average of all the available daily cross-correlation functions,

$$\mathrm{CC}_r(\tau, \mathbf{x}_1, \mathbf{x}_2) = \frac{1}{N_d}\sum_{j=1}^{N_d} \mathrm{CC}^j(\tau, \mathbf{x}_1, \mathbf{x}_2), \tag{4.8}$$

where N_d is the total number of days, while the current cross-correlation function that corresponds to the j-th day is the average of a small number of daily cross-correlation functions around the j-th day,

$$\mathrm{CC}_c^j(\tau, \mathbf{x}_1, \mathbf{x}_2) = \frac{1}{2s+1}\sum_{k=j-s}^{j+s} \mathrm{CC}^k(\tau, \mathbf{x}_1, \mathbf{x}_2). \tag{4.9}$$

The total number of daily cross-correlations used for the current cross-correlation is $N_{ccc} = 2s + 1$. Usually a few days ($N_{ccc} = 3$ to 10) are used for the current cross-correlation while the reference one is computed for a much longer period of the order of a year [15].

Velocity Model and selected bandwidth

We will work in the frequency bandwidth $[0.15 - 0.65]$Hz and with total number of days $N_d = 360$ (a year). For our simulations we consider two different velocity models. In the first case the velocity of the medium does not change with time and is equal to 1Km/s while in the second case there is a small change in the velocity of the order of 1% that takes place between days 80 to 110. The velocity increases linearly the first 15 days until it reaches the

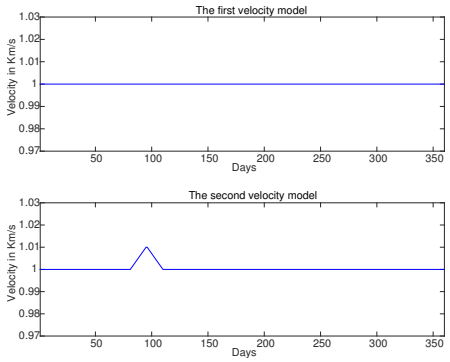

Figure 4.2: The two velocity models. In the top plot the velocity does not change with time and is equal to 1Km/s. In the bottom plot the velocity increases linearly between days 80 and 95 to reach the value of 1.01Km/s and then decreases linearly with the same rate to reach its original value of 1Km/s at day 110.

maximal value of 1.01Km/s and then decreases linearly with the same rate to its original value of 1Km/s as illustrated in Figure 4.2 (bottom plot). These numbers are realistic and similar to those in the seismic noise recordings of the Santorini volcano considered in section §4.2. We have chosen the numerical set up to be comparable to the experimental one so that the numerical results may support the conclusions drawn from the seismic data.

Estimation of the relative change in the velocity

We have implemented both the SM and MWCS methods using as reference cross-correlation the average of all daily cross-correlation (360 days) and as current cross-correlation a N_{ccc} = 7-day average around the day we make the measurement.

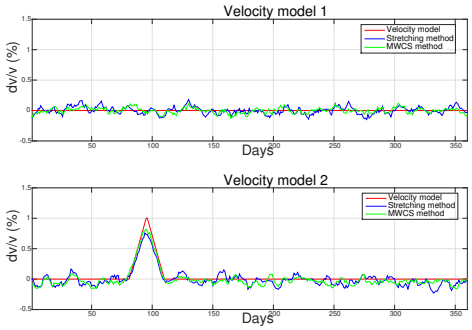

Figure 4.3: Relative velocity change estimation using SM (blue) and MWCS (green) for the constant (top) and the variable (bottom) velocity models of Figure 4.2.

The results obtained by both methods for the two velocity models are shown in Figure

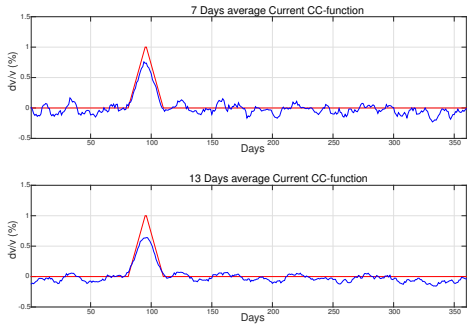

Figure 4.4: In the top plot $N_{ccc} = 7$ days are used in computation of the reference CC while $N_{ccc} = 13$ days are used in the bottom plot. In red is the true velocity variation and in blue the estimated one. Using $N_{ccc} = 7$ days gives a more precise estimation for the maximal value of dv/v while with $N_{ccc} = 13$ days the fluctuations around zero are decreased.

4.3. We can see that the results are comparable and both methods can recover the relative velocity change up to a small error. We chose for the current cross-correlation a $N_{ccc} = 7$-day average because here is a direct relation between the number of days N_{ccc} that are used in the current CC function and the standard deviation of the measurement error. When there is no velocity variations ($dv/v = 0\%$), the obvious answer is that the standard deviation of the error is reduced by increasing the number of days used in the computation of the current CC. However, this results to a loss in precision in the estimation of $dv/v \neq 0$ as illustrated by the results in Figure 4.4. An optimal value for the number of days to be used can be obtained by studying how the error changes as we increase the number of days N_{ccc}. The value we selected is 7 since for this value we have a minimum in the error as suggested by the plots in Figure 4.5.

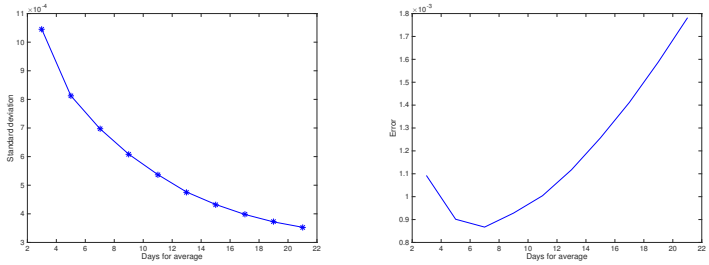

Figure 4.5: Left: The standard deviation of the error in the period where $dv/v = 0$ (days 1 to 80 and 110 to 360) as a function of number of days N_{ccc} stacked for the Current CCfunction. Right: The error for the days 80 to 110 using the norm $\|x\| = \sqrt{\sum_{i=1}^{m} |x_i|^2}$, where $x \in \mathbf{R}^m$ as a function of N_{ccc}.

4.1.2 Seasonal variations in the noise sources and their influence to the relative velocity change measurements

Let us write equation (4.7) in the frequency domain using equations (4.2) and (4.4),

$$\begin{aligned}\widehat{\mathrm{CC}}^j(\omega,\mathbf{x}_1,\mathbf{x}_2) = \\ \int d\mathbf{y}\ \overline{\hat{G}^j(\omega,\mathbf{x}_1,\mathbf{y})}\hat{G}^j(\omega,\mathbf{x}_2,\mathbf{y})\hat{\Gamma}^j(\omega,\mathbf{y}).\end{aligned} \tag{4.10}$$

Here $\omega \to \hat{\Gamma}^j(\omega,\mathbf{y})$ is the power spectral density of the noise sources at location $\mathbf{y}$ during day j. As a complex function, the cross-correlation can be written as a product of an amplitude and a phase

$$\hat{\mathrm{CC}}_j(\omega,\mathbf{x}_1,\mathbf{x}_2) = A_j(\omega,\mathbf{x}_1,\mathbf{x}_2)e^{i\phi_j(\omega,\mathbf{x}_1,\mathbf{x}_2)}. \tag{4.11}$$

We will use a normalization (spectral whitening) of the cross-correlation functions which consists in replacing the amplitude $A_j(\omega,\mathbf{x}_1,\mathbf{x}_2)$ by 1 in the frequency range where it is above a threshold. Therefore we get,

$$\hat{\mathrm{CC}}_j(\omega,\mathbf{x}_1,\mathbf{x}_2) = e^{i\phi_j(\omega,\mathbf{x}_1,\mathbf{x}_2)}. \tag{4.12}$$

After this spectral whitening we expect that seasonal variations that affect only the amplitude spectra of the cross-correlation function will not have an impact on the measurement of dv/v.

Uniform and non-uniform seasonal variations.

Our model for the power spectral density of the noise sources is

$$\hat{\Gamma}_0^j(\omega,\mathbf{y}) = \hat{F}(\omega)\hat{s}^j(\omega,\mathbf{y}),$$

Here the unperturbed noise source distribution is uniform over the circle $\mathcal{C}$ and has power spectral density $\hat{F}(\omega)$, and $\hat{s}^j(\omega,\mathbf{y})$ is the daily perturbation of the power spectral density at location $\mathbf{y}$. We have two different representations for $\hat{s}^j$:

1. The daily perturbation is uniform with respect to the locations of the sources:

$$\hat{s}^j(\omega,\mathbf{y}) = \hat{f}^j(\omega)l(\mathbf{y}), \tag{4.13}$$

2. The daily perturbation is not uniform and we cannot write it in a separable form.

In the first case equation (4.10) becomes

$$\begin{aligned}\hat{\mathrm{CC}}^j(\omega,\mathbf{x}_1,\mathbf{x}_2) = \hat{F}(\omega)\hat{f}^j(\omega) \\ \times\int_{\mathcal{C}} d\sigma(\mathbf{y})\ \overline{\hat{G}^j(\omega,\mathbf{x}_1,\mathbf{y})}\hat{G}^j(\omega,\mathbf{x}_2,\mathbf{y})l(\mathbf{y}),\end{aligned} \tag{4.14}$$

and it is clear that after spectral whitening, any daily perturbation in the power spectral density of the noise sources will be eliminated since the perturbation is contained into the amplitude spectra of the cross-correlation function. In the second case we cannot separate the terms due to the sources and take them out of the integral.
Instead of equation (4.6), we use,

$$\begin{aligned}\hat{u}^j(\omega,\mathbf{x}) &= \frac{1}{N_s}\sum_{i=1}^{N_s}\hat{n}_i^j(\omega)\hat{G}^j(\omega,\mathbf{x},\mathbf{y}_i)\\ &\times(1-\delta\hat{g}(\omega)\sin(2\pi j/N_d)),\end{aligned} \tag{4.15}$$

with $\delta = 0.4$ and

$$\hat{g}(\omega) = \begin{cases} 1 & \text{if } \omega_1 \le \omega \le \omega_1 + \pi B,\\ 0 & \text{if } \omega_1 + \pi B < \omega \le \omega_1 + 2\pi B,\end{cases}$$

to simulate uniform seasonal variations with

$$\hat{s}^j(\omega,\mathbf{y}) = (1-\delta\hat{g}(\omega)\sin(2\pi j/N_d))^2. \tag{4.16}$$

In the simulations we take $\hat{F}(\omega) = \mathbf{1}_{[\omega_1,\omega_1+2\pi B]}(|\omega|)$, $B = 0.5$Hz and $\omega_1 = 2\pi\, 0.15$rad.s^{-1}. To add anisotropy we multiply (4.15) by a function that depends on the source azimuth, $\theta(\mathbf{y})$. More precisely, we take

$$\begin{aligned}\hat{u}^j(\omega,\mathbf{x}) &= \frac{1}{N_s}\sum_{i=1}^{N_s}\hat{n}_i^j(\omega)\hat{G}^j(\omega,\mathbf{x},\mathbf{y}_i)\\ &\times(1-\delta\hat{g}(\omega)\sin(2\pi j/N_d))(1-0.6\cos(2\theta(\mathbf{y}_i))),\end{aligned} \tag{4.17}$$

which results to a model for $\hat{s}^j(\omega,\mathbf{y})$ in (4.14) of the form

$$\hat{s}^j(\omega,\mathbf{y}) = (1-\delta\hat{g}(\omega;\theta(\mathbf{y})+2\pi j/N_d)\sin(2\pi j/N_d))^2(1-0.6\cos(2\theta(\mathbf{y})))^2, \tag{4.18}$$

where $\theta(\mathbf{y})$ is the angle of $\mathbf{y}$ on the circle $\mathcal{C}$. This is a quite extreme case of anisotropy cf. [71, 16] which allows us to illustrate the robustness of the proposed filtering. For the non-uniform case, we use,

$$\begin{aligned}\hat{u}^j(\omega,\mathbf{x}) &= \frac{1}{N_s}\sum_{i=1}^{N_s}\hat{n}_i^j(\omega)\hat{G}^j(\omega,\mathbf{x},\mathbf{y}_i)\\ &\times(1-\delta\hat{g}(\omega;2\pi i/N_s+2\pi j/N_d)\sin(2\pi j/N_d)),\end{aligned} \tag{4.19}$$

where

$$\hat{g}(\omega;\theta) = \begin{cases} 1 & \text{if } \omega_1 \le \omega \le \omega(\theta),\\ 0 & \text{if } \omega(\theta) < \omega \le \omega_1 + 2\pi B,\end{cases} \tag{4.20}$$

with

$$\omega(\theta) = \omega_1 + \pi B + \pi B\sin(\theta). \tag{4.21}$$

This models non-uniform seasonal variations with

$$\hat{s}^j(\omega, \mathbf{y}) = (1 - \delta\hat{g}(\omega; \theta(\mathbf{y}) + 2\pi j/N_d)\sin(2\pi j/N_d))^2. \tag{4.22}$$

As shown above, when the seasonal variations of the noise sources are spatially uniform, then they affect only the amplitude spectra of the cross-correlations. Treating successfully the uniform case is important since we expect this behavior to hold in most cases of interest where the receivers are close together geographically so that the seasonal variations are affecting in the same way, more or less, the ambient noise sources.

However, if the seasonal variations affect also the phase spectra of CC then the spectral whitening will not ensure that the measurement of dv/v is free of apparent velocity changes due to seasonal variations of the noise sources. Our numerical model can simulate the daily perturbation of the power spectral density of the sources so as to be uniform or non-uniform with respect to the locations of the sources.

4.1.3 Numerical simulations in a homogeneous medium

We use here our numerical model with two different types of seasonal variations (uniform and non-uniform) and we study how these seasonal variations affect the estimations of the relative change in velocity when we use the stretching and the MWCS methods. We add first seasonal variations of a separable form as in equation (4.15). Then (4.10) becomes

$$\hat{\mathrm{CC}}^j(\omega, \mathbf{x}_1, \mathbf{x}_2) = \hat{F}(\omega)\hat{f}^j(\omega)\int_{\mathcal{C}} d\sigma(\mathbf{y})\overline{\hat{G}^j(\omega, \mathbf{x}_1, \mathbf{y})}\hat{G}^j(\omega, \mathbf{x}_2, \mathbf{y})l(\mathbf{y}), \tag{4.23}$$

and we first take $l(\mathbf{y}) = 1$.

In this case only the amplitude of the cross-correlation is affected by the seasonal variations of the noise sources and therefore we expect only the stretching method to be affected. Indeed, as we observe in Figure 4.6 only the stretching method reflects the seasonal variations of the noise sources into seasonal variations on the measurement of dv/v. MWCS operates in the frequency domain and measures the phase difference between the two waveforms. Therefore, seasonal variations in the amplitude spectra of the cross-correlation do not affect the MWCS estimation.

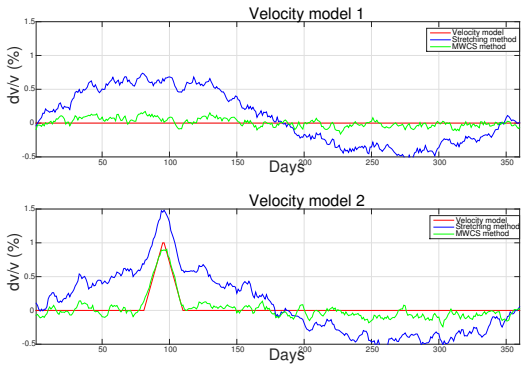

Figure 4.6: Relative velocity change for the first (top) and the second (bottom) velocity model using SM (blue) and MWCS (green) for the velocity models of Figure 4.2. Only the stretching method is affected by the seasonal variations since those are uniform with respect to the locations of the noise sources.

By using spectral whitening we correct for the seasonal variations in the amplitude of the cross-correlation function and as a result we expect to no longer observe seasonal variations in the measurements of dv/v when we use the stretching method. This is illustrated with our numerical results in Figure 4.7.

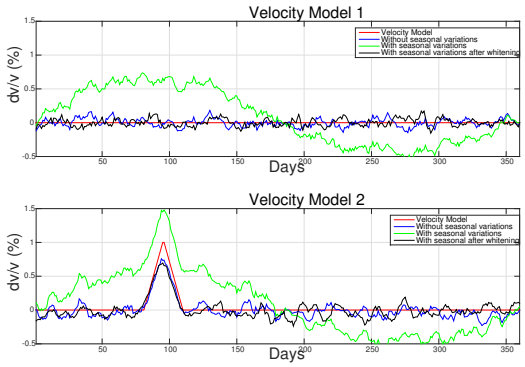

Figure 4.7: Comparison between the estimation obtained for the model without seasonal variations in blue (equation (4.6)), the model with uniform seasonal variations in green (equation (4.15)) and the effect of spectral whitening to the estimation in black for both velocity models. All estimations here are produced using the stretching method.

We do not expect to get the same result when the seasonal variations are of non-separable form as in equation (4.19). In this case, (4.10) becomes (for $l(\mathbf{y}) = 1$)

$$\hat{\mathbb{CC}}^j(\omega, \mathbf{x}_1, \mathbf{x}_2) = \hat{F}(\omega) \int_{\mathcal{C}} d\sigma(\mathbf{y}) \overline{\hat{G}^j(\omega, \mathbf{x}_1, \mathbf{y})} \hat{G}^j(\omega, \mathbf{x}_2, \mathbf{y}))(1 - \delta \hat{g}(\omega; \theta(\mathbf{y}) + 2\pi j/N_d) \sin(2\pi j/N_d))^2,$$

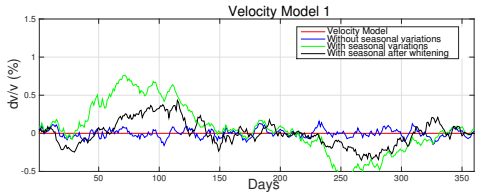

Figure 4.8: The estimation produced by the stretching method for the numerical model without seasonal variations in blue (equation (4.6)), the model of uniform seasonal variations in green (equation (4.19)) and the effect of spectral whitening to the estimation in black.

where $\theta(\mathbf{y})$ is the angle of $\mathbf{y}$ on the circle $\mathcal{C}$, $\delta = 0.4$ and $\hat{g}$ is defined in equations (4.20,4.21).

Indeed, we as we observe in Figure 4.8, spectral whitening cannot remove the seasonal variations any longer since those variations affect both the amplitude and phase spectra of the cross-correlation.

4.1.4 Simulations in a scattering medium

The results presented in the previous section are for a homogeneous medium and are obtained using the direct waves in the cross-correlations. More precisely we used the time window $[10.5, 20.5]$s (this includes the direct arrival since the pulsewidth is 2s and the travel-time between the sensors is $10s$). To illustrate the generality of our approach we consider here the case of a scattering medium. The Green's function is computed now by solving the wave equation in a square domain of 50Km$\times$50Km (see Figure 4.9) filled with a scattering medium with an average velocity of 1Km/s and 10% fluctuations. The medium fluctuations here may produce less scattering than the circular inclusions with a contrast of 50% considered in [16] but our fluctuations model seems quite realistic in the geophysical context. The wave equation is solved with the software Montjoie (http://montjoie.gforge.inria.fr/) using seventh order finite elements for the discretization in space and fourth order finite differences in time. The computational domain is surrounded by a perfectly matched absorbing layer model (PML).

In Figure 4.10-left we compare the reference CC function with the Green's function between the two receivers obtained by emitting a pulse from one receiver and recording it at the other. We have very good agreement between the two signals up until ≈ 42s. In Figure 4.10-right we compare the reference CC function in the scattering medium with the one in the homogeneous medium. The oscillations before and after the main peak of the pulse in the homogeneous medium are due to the limited bandwidth of the noise sources. Note that the two signals differ significantly after 12.5s.

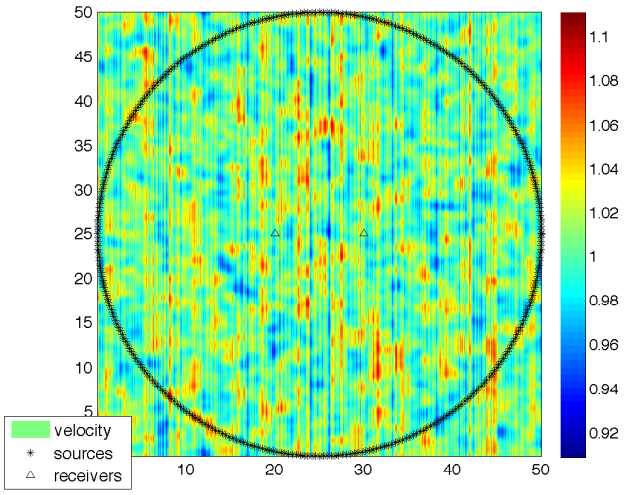

Figure 4.9: Highly scattering medium. The positions of the sources/receivers are the same as in the homogeneous case (see Figure 4.1).

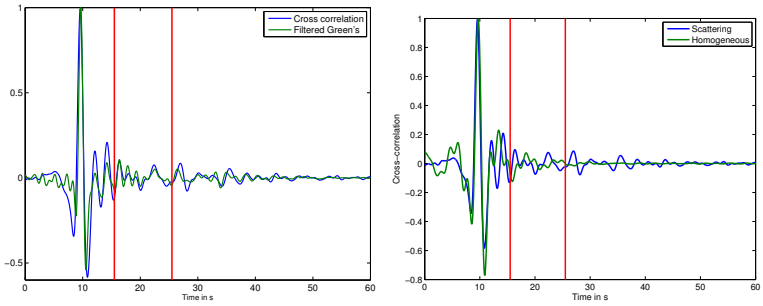

Figure 4.10: Left: The reference CC in the scattering medium compared with the Green's function between the two receivers filtered by the power spectral density of the noise sources. Amplitudes are normalized. Right: The reference CC in the homogeneous and the scattering medium. In both plots, the two red vertical lines indicate the window $[15.5 - 25.5]$s.

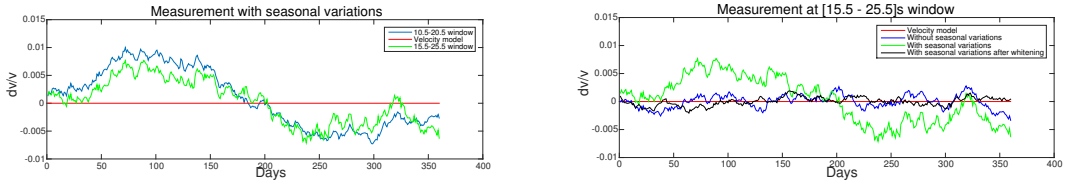

Figure 4.11: Scattering medium. Left: SM estimation of dv/v in the present of seasonal variations of a separable form using two different time windows. Right: The seasonal variations are removed using spectral whitening ($[15.5 - 25.5]$s window).

We consider now seasonal variations of separable form as in (4.23) with $l(\mathbf{y}) = 1$ and estimate dv/v with the stretching method using two different time windows: first the same window as before $[10.5 - 20.5]$s, and second, the window $[15.5 - 25.5]$s. As we can see in Figure 4.11-left the apparent false variations in dv/v are reduced by using the coda part of the CC but they still persist. The proposed spectral whitening of CC efficiently removes the fluctuations as illustrated in Figure 4.11-right. Let us emphasize that spectral whitening will be efficient for any spatio-temporal variation of the noise sources of separable form since such variations affect only the amplitude of CC, regardless of the underlying medium (homogeneous or scattering).

Simulations for anisotropic noise distributions

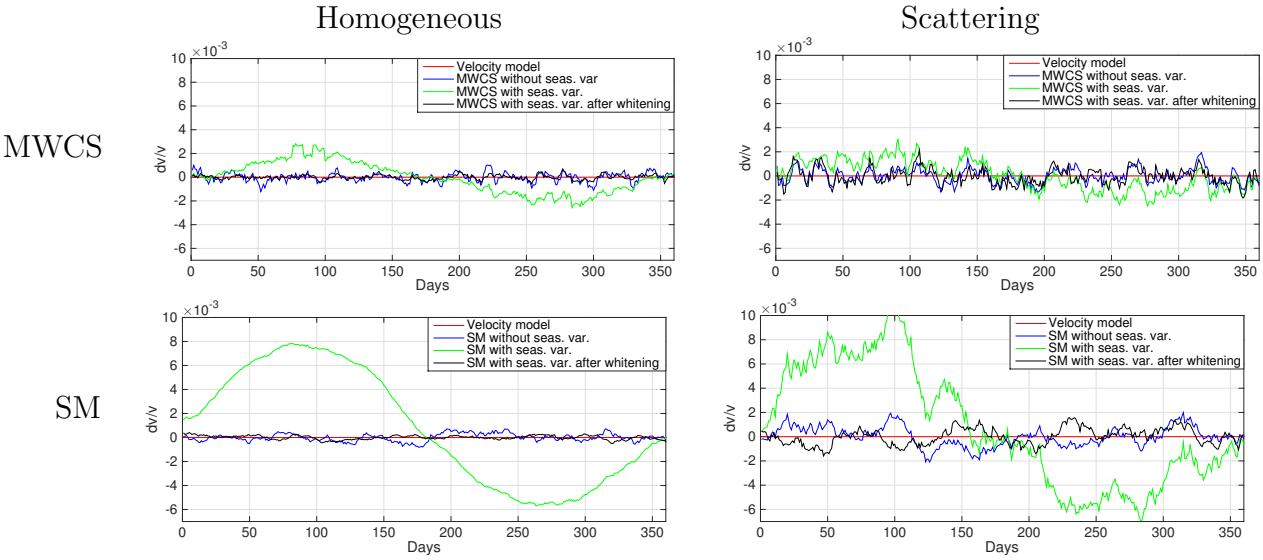

Figure 4.12: Removing the seasonal variations using spectral whitening. The noise sources have anisotropic spatio-temporal fluctuations as described by (4.17)-(4.18). For the SM method, the measurements in the homogeneous medium are performed using the $[10.5-20.5]$s window while in the scattering medium the $[15.5 - 25.5]$s window is used.

To further illustrate the robustness of the proposed filtering we add now anisotropy to the noise sources. Following [16] we consider a rather extreme case of anisotropy using (4.17) which amounts to cross-correlations as in (4.23) with azimuthal intensity distributions of the form,

$$l(\mathbf{y}) = (1 - 0.6\cos(2\theta(\mathbf{y})))^2,$$

with $\theta(\mathbf{y})$ the source azimuth, *i.e.*, the angle of $\mathbf{y}$ on the circle $\mathcal{C}$. The results obtained with MWCS and SM in homogeneous and scattering media before and after spectral whitening are shown in Figure 4.12. As expected the MWCS estimation is less affected by the spatio-temporal variations of the noise sources since to the leading order the phase of the

cross-correlation remains unchanged [71]. The amplitude of the cross-correlation however is affected and this leads to erroneous estimates with SM. The results of both methods are greatly improved with spectral whitening. In the scattering medium the anisotropy effect of the noise sources is reduced through multiple scattering of the waves with the medium inhomogeneities. This corrects for the anisotropy effect on the phase of the cross-correlation but not on the amplitude. Therefore SM estimation remains bad while the MWCS estimation is better in the scattering medium. Again the results of both methods are improved with spectral whitening.

In the results show in Figure 4.12 we have not included attenuation in the propagation medium, however similar results have been obtained when attenuation is taken into account. The main observation is that attenuation affects the amplitude of the recorded signals and not the phases. Moreover, the one bit quantization treatment of the data [5] removes the attenuation effect as suggested in [53], and thus the conclusions drawn above carry over when attenuation is present.

4.1.5 Seasonal variations examined in the island of Milos

Using the developed methodology we investigate here relative velocity changes in the quiet volcanic island of Milos, in Greece. Two broadband seismic stations (codes: MHLO and MHLA) operate there in real time, monitoring seismicity in the Aegean volcanic arc for the National Observatory of Athens, Institute of Geodynamics (NOAIG) (Figure 4.13). The two stations are part of the Hellenic National Seismic Network (network code: HL) and they are deployed 6km apart and above the Milos island geothermal reservoir.

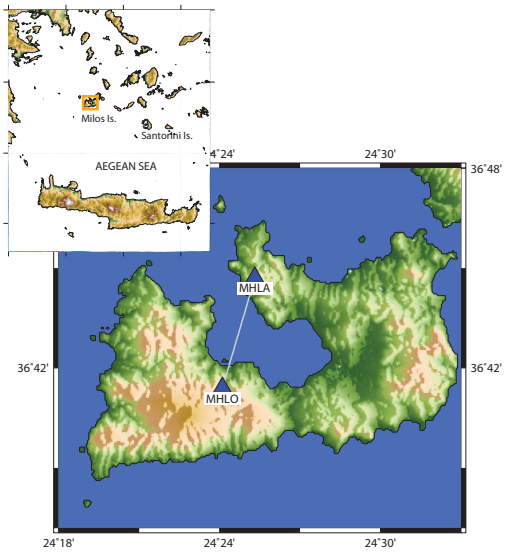

Figure 4.13: The volcanic island of Milos and the locations of the two NOAIG broadband seismic stations used in this study. The inset at the left hand side of the map shows the location of Milos island (orange rectangle) within the Aegean sea.

We gather seismic noise recordings for the last days of 2011 and the entire 2012 and 2013 (827 days in total). During the examined period there was no significant local earthquake activity in the area. In Figure 4.14-left we observe the seasonal variations on the Power Spectral Density (PSD) of the station MHLA and we want to investigate if the stretching method is affected by these variations. The seasonal variations can be attributed to local sea–weather conditions within a range of a few hundred kilometers from the stations [26].

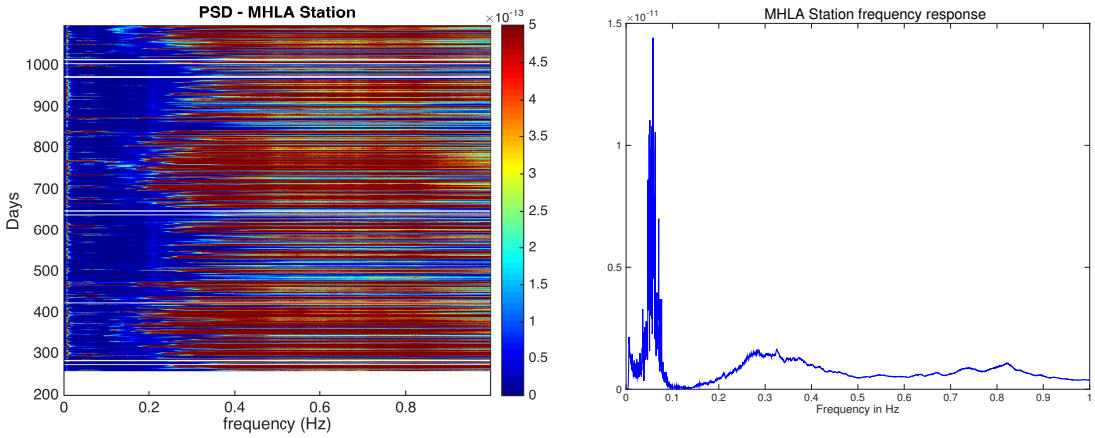

Figure 4.14: Left: The Power Spectrum Density of the station MHLA at Milos. Right: The frequency response of the MHLA station calculated by averaging the daily frequency response of all available days.

The data are filtered from $0.1 - 1.0$Hz a bandwidth for which we have microseismic activity as suggested by Figure 4.14-right. This frequency bandwidth is used for Santorini in the next section since the power spectral density of the recorded signals is more or less the same.

As we see in Figure 4.15, the proposed normalization (spectral whitening) has the desirable effect on seasonal variations just as the numerical simulations suggest. Considering the apparent velocity fluctuations induced by seasonal variations of the noise sources, as measurement noise, we obtain a decrease in the noise level by a factor of 3, after using the proposed normalization. Using the stretching method with spectral whitening, we observe residual fluctuations in the estimated velocity of the order of $\pm 0.1\%$. We also plot in Figure 4.15 the results obtained using MWCS (green). As expected MWCS is not affected by the seasonal variations and gives similar results, albeit more noisy, than the ones obtained with SM after normalization.

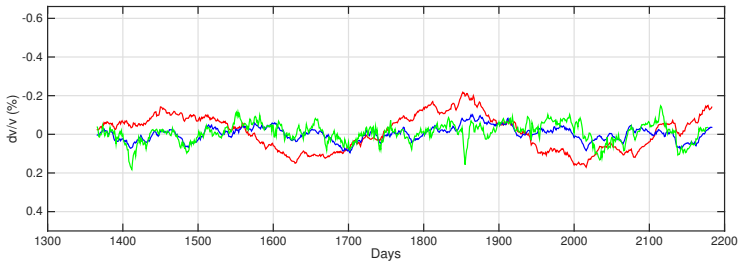

Figure 4.15: The estimation between the pair MHLO-MHLA located on the island of Milos when we use spectral whitening (blue) and when we do not use it(red). Here $N_{ccc} = 21$ Days. We also plot with green the estimation of the MWCS method which is not affected by the seasonal variations.

4.2 Investigation of the Santorini island seismic unrest 2011-2012

During the time period January 2011 to March 2012, high microseismic activity was observed in the caldera of the Santorini island (Figure 4.18). This also coincided with a 10cm uplift measured by GPS stations deployed in the area, monitoring continuously crustal deformation [50]. During the unrest period, several portable seismic stations were deployed in the area by research institutions and universities. However, due to the urgency to capture the ongoing unrest, the portable stations were deployed mainly to monitor seismicity in near real time and thus, their data quality and/or availability was not suitable for ambient noise monitoring. Prior to the unrest, only two digital broadband seismic stations were in operation (Figure 4.16). These two were found useful for investigating variations in dv/v with the stretching method. Their inter-station path crosses the edge of the uplifted area within the caldera which is also the source region of the majority of the observed seismic clusters [41].

The unrest was studied in [42] and [58] using GPS data and the results suggest elevation at the volcano mainly at periods of high seismicity. More specifically the seismic activity was high from January 2011 until August 2011 and then again from October 2011 to February 2012. Those two periods of high seismicity are the same periods during which GPS data suggest that there is an elevation of the caldera.

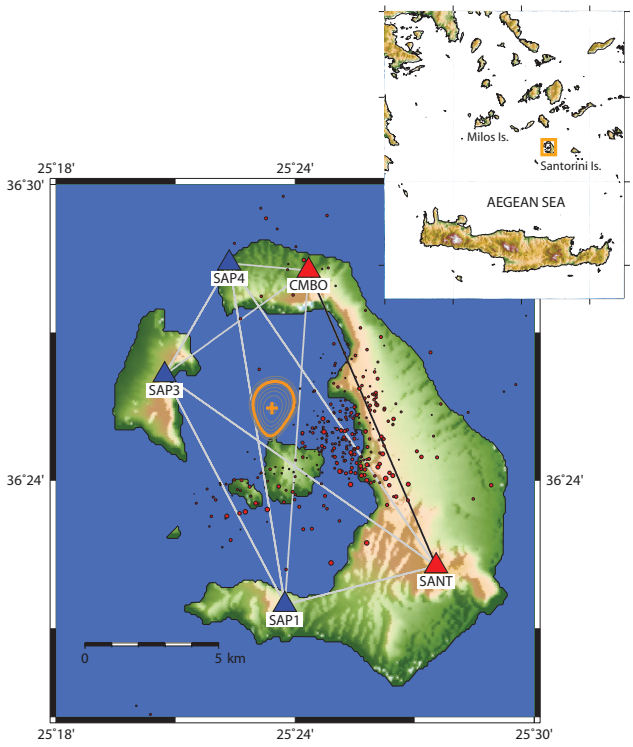

Figure 4.16: Network of seismic stations in Santorini and the inter-station paths. Stations that were in operation prior to the unrest are marked in red. Stations that became operational during or after the unrest are marked in blue. Red circles indicate the relocated seismicity according to [41] with their size being proportional to the event local magnitude (M_L) as measured by NOAIG. The orange cross marks the geographic location of the modeled volumetric growth at 4 km depth [50] with their 95% confidence level (concentric circle). The inset at the right hand side of the map shows the location of Santorini island (orange rectangle) within the Aegean sea.

4.2.1 Data Treatment

For each pair of stations we follow these steps. First we separate the 24-hours long segment of each station into eight 3-hours segments. If a 3-hours long segment has more than 10% of gaps then it is rejected and is not used in the calculations of the cross-corellation (CC). Otherwise, we filter the data in the band $[0.1 - 1.0]$Hz. Then we apply one-bit quantization and we cross-correlate with the corresponding segment from the paired station. For each day we expect at most eight Cross-Correlation functions. If a 3-hour segment is rejected then we miss one cross-correlation and only if for one day we miss three or fewer cross-correlation functions we proceed and average the 3-hours segments to get the daily cross-correlation function. A final step that helps us to deal under some conditions with seasonal variations in the power spectral density of the noise sources is to apply spectral whitening on the cross-

correlations inside the bandwidth of interest, i.e., $[0.1 - 1.0]$Hz.

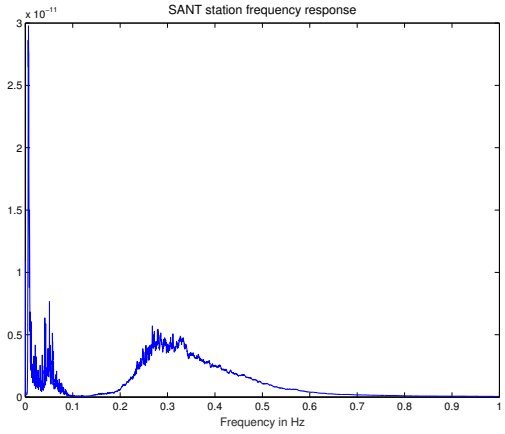

Figure 4.17: The frequency response of the SANT station calculated by averaging the daily frequency response of all available days.

For the reference cross-correlation function we use the mean of all available daily cross-correlation functions. The current cross-correlation function on the other hand is the mean of $N_{ccc} = 21$ days around the day where we want to make the measurement.

The data treatment that we follow is a procedure as described in [5] with an additional post-whitening step on the cross-correlations inside the bandwidth of interest. The pre-whitening step [5] is used on the recorded signal because ambient noise is not flat in the frequency domain of interest and aims to broaden the band of micro-seismic noise and remove the effect of any monochromatic source that may be dominant. The post-whitening step is used on the cross-correlations and aims at removing any amplitude variations that they may have so that only phase information remains to be used in the stretching method's estimation.

4.2.2 Results

Our implementation of the stretching method is configured to make two measurements of dv/v using the positive and the negative time axis in a time window that is focused on the coda part. ($[15, 35]$s and $[-35, -15]$ in our case). The final result is the average of the two measurements as long as the correlation coefficient is higher than 0.7 otherwise the result is rejected.

The drop of the dv/v is maximal in May 2011, associated with a considerable drop of the CC coefficient (Fig. 4.18). This implies a change in the scattering medium at least for these days.

Unfortunately we do not have data that cover the entire period of the unrest but as we can see in Figure (4.18) we can compare the available data with GPS data (from the GPS station NOMI, located roughly in the middle of the inter-station path between SANT and CMBO).

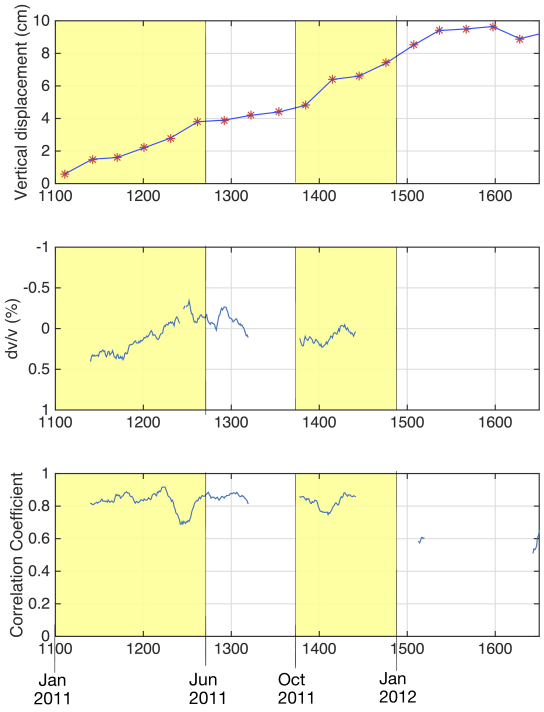

Figure 4.18: Top: Accumulated elevation of the GPS station NOMI in Santorini [58]. Middle: The estimation of dv/v using the stretching method. Bottom: The correlation coefficient of the stretching method.

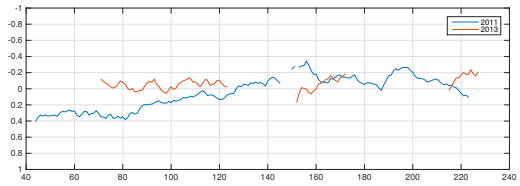

Figure 4.19: Results using the stretching method in two different years, for Julian dates between 40 and 240.

The result shown in Figure 4.18 middle plot is quite close to the GPS measurements, at least during the periods that we have available data and for the periods with high seismic

activity (high seismic activity corresponds to the yellow background). We can also see that the elevation increases mainly at the periods of high seismic activity according to the GPS data (top plot at Figure 4.18).
Based on the data for Milos (Figure 4.15) and for Santorini in 2013 (Figure 4.19, red), the estimated velocity has random fluctuations of the order of $\pm 0.1\%$, resulting from residual seasonal variations and errors in the estimation. Therefore, any change of more than $\pm 0.1\%$ can be considered as significant, *i.e.*, resulting from physical changes in the velocity distribution. This is what happens in Santorini in 2011 (Figure 4.19, blue).

4.3 Conclusions

In this chapter we considered the problem of seismic velocity change estimation based on passive noise recordings. Using simple but realistic numerical simulations as a tool, we study how the estimation produced by the stretching method is affected by seasonal spatio-temporal fluctuations of the amplitude spectra of the noise sources [76, 47]. Moreover, we show that the use of the coda part of the cross-correlation may be not enough to compensate for the seasonal fluctuations when scattering is moderate and an adequate normalization (spectral whitening) of the cross-correlation functions reduces the effect of the seasonal fluctuations of the noise sources. We also study the Santorini unrest event of 2011-2012, a slow event that spans a period of several months, and for which it would have been extremely difficult to follow the variations of dv/v without removing the seasonal fluctuations. Our results show a decrease in the velocity of seismic waves in the caldera of Santorini which is correlated with the accumulated elevation measured with GPS. This illustrates the potential of developing monitoring tools which provide accurate results even with sparse seismic networks with careful signal processing of passive noise recordings.

Part II

Velocity Tomography

Chapter 5

Velocity tomography using seismic noise

The procedure of producing an image of a cross-section (slice) of an object, without cutting it, through the use of some penetrating wave is called tomography. There are numerous applications of tomography such as X-ray tomography in medicine or seismic travel-time tomography in geophysics. The type of the penetrating wave can vary, so positron emission is used in Positron Emission Tomography (PET), X-rays are used in X-ray tomography (CT,CATScan), seismic waves are used in seismic tomography, etc. In this chapter we focus on seismic travel-time tomography where we want to estimate the velocity in the earth from travel-time measurements.

5.1 Introduction

Travel-time tomography is a very hard, nonlinear problem and numerous methods have been developed for dealing with this inverse problem. These methods not only produce the "image" of the velocity, but also provide information about the validity of the reconstructed image. The validity information is used to decide which method is more suitable for a specific problem [6]. Seismic tomography uses seismic waves generated by earthquakes and explosions to create maps of the velocity of the Earth's interior. The last two decades it became very popular the use of seismic noise instead, and we will follow that approach here.

More precisely, in this chapter following the work of [36, 43] we will use the eikonal tomography approach. The term "eikonal" comes from the eikonal equation,

$$\frac{1}{c_i(r)^2} = |\nabla\tau(r_i, r)|^2 - \frac{\nabla^2 A_i(r)}{A_i(r)\omega^2},$$

which is the key ingredient of the method. The idea in eikonal tomography is to use travel-time measurements $\tau(r_i, r_j)$ between pairs of points $r_i,\ r_j$ to produce travel-time surfaces $\tau(r_i, r)$. Then the local speed $c_i(r)$ at an arbitrary point r is estimated using the eikonal equation. The second term that contains the amplitude, $A_i(r)$, in the eikonal equation is

neglected in practice. This is justified only at high frequencies ω or when $A_i(r)$ slowly varies with respect to the position r. There are some intermediate steps in this methodology which should be carefully addressed. For example to calculate the travel-time surfaces, from a set of travel-time measurements, the use of an interpolation method is needed. The choice of the interpolation method plays a significant role on the reliability of the final reconstructed image. Eikonal tomography, despite its limitations, is a very simple method to implement and computationally cheap.

The travel-time measurements is another concern for us. In this chapter we will use travel-time measurements computed from ambient noise recordings. The tool in hand is the cross-correlation function, defined in (2.6),

$$C_T(\tau, x_1, x_2) = \frac{1}{T}\int_0^T u(t, x_1)u(t+\tau, x_2)\mathrm{d}t,$$

where $u(t, x_1)$ and $u(t, x_2)$ are the noise recordings at receivers x_1 and x_2 respectively and T is the length of the recordings.

As we discussed in section 2.3, given a recording time T large enough and with some requirements on the spatial distribution of the ambient noise sources, the cross-correlation function converges to the symmetrized Green's function between the two receivers [29] and therefore travel-time information can be extracted from the cross-correlation function. For the travel-time estimation we provide two alternative methods: The envelope function and the stretching method.

5.2 Problem setup: the wave equation

To make this chapter to a certain extent self contained, we review in this section some material on the wave equation, the Green's function and the cross-correlation of noisy recordings.

To describe wave propagation in the earth, one should consider the elastic (or visco-elastic) wave equation in three dimensions. We consider here instead the scalar wave equation which is often used as a simplified model,

$$\frac{1}{c^2(x)}\frac{\partial^2 u}{\partial t^2}(t, x) - \Delta_x u(t, x) = n(t, x),$$

where $u(x, t)$ is the acoustic pressure field, $n(t, x)$ is the source function and $c(x)$ denotes the propagation speed in the medium assumed to be constant outside a domain with compact support.

The noise source $n(x, t)$ will play an important role in our setup. Usually $n(x, t)$ is a deterministic source compactly supported in space (often a point source is used) which emits a compactly supported pulse in time. Recently there has been a lot of interest in the development of passive correlation based methods that rely on the use of ambient noise recordings for extracting information about the medium in which the waves propagate. In the previous chapters we've discussed most of the aspects and in this setting, the sources

are randomly distributed in space and they emit long noisy signals. A reasonable model for the source is therefore to assume that $n(x,t)$ is a space-time stationary random field which is delta correlated in space and time. The delta-correlated assumption is not very realistic and can be relaxed. We refer the reader to the seminal work of Michel Campillo and his collaborators on passive seismology "a new way of imaging the earth's interior using only noise" [61, 60, 35, 25, 12] as well as to the work of George Papanicolaou et al on the mathematical analysis of correlation based methods [29, 30, 31, 32].

It is useful at this point to reintroduce the following quantities from chapter 2, beginning with the time-dependent Green's Function $G(t,x,y)$ for the wave equation which is the solution of

$$\frac{1}{c^2(x)}\frac{\partial^2 G}{\partial t^2}(t,x,y) - \Delta_x G(t,x,y) = \delta(t)\delta(x-y).$$

Assuming that $G(t,x,y) = 0, \ \ \forall t < 0$, we get a unique solution which is the causal Green's function. The Green's function is therefore the response at point x and time t due to a delta function pulse emitted at time 0 from a point source located at y.
If the medium is homogeneous $c(x) \equiv c_0$, then

$$G(t,x,y) = \frac{1}{4\pi|x-y|}\delta(t - \frac{|x-y|}{c_0}), \quad t > 0.$$

The time-harmonic Green's function, defined as the Fourier transform of $G(t,x,y)$,

$$\hat{G}(\omega,x,y) = \int G(t,x,y)e^{i\omega t}\mathrm{d}t,$$

is the solution of the Helmholtz equation,

$$\Delta_x \hat{G}(\omega,x,y) + \frac{\omega^2}{c^2(x)}\hat{G}(\omega,x,y) = -\delta(x-y),$$

with the Sommerfeld radiation condition ($c(x) = c_0$ at infinity),

$$\lim_{|x|\to\infty} |x|(\frac{x}{|x|}\nabla_x - i\frac{\omega}{c_0})\hat{G}(\omega,x,y) = 0.$$

If the medium is homogeneous $c(x) \equiv c_0$, then

$$\hat{G}(\omega,x,y) = \frac{1}{4\pi|x-y|}e^{i\frac{\omega}{c_0}|x-y|}.$$

We can express now the solution of the wave equation with a source $n(t,x)$ in terms of the Green's function through the convolution,

$$u(t,x) = \int\int G(t-s,x,y)n(s,y)\mathrm{d}y\mathrm{d}s,$$

or, in the frequency domain,

$$\hat{u}(\omega, x) = \int \hat{G}(\omega, x, y)\hat{n}(\omega, y)\mathrm{d}y,$$

where $\hat{u}(\omega, x)$ is

$$\hat{u}(\omega, x) = \int u(t, x)e^{i\omega t}\mathrm{d}t.$$

Let us also recall the following two properties of the Green's function [29],

i. Reciprocity:

$$\hat{G}(\omega, x, y) = \hat{G}(\omega, y, x).$$

ii. The Helmholtz-Kirchhoff identity:

If the medium is homogeneous with velocity c_0 outside $B(0, D)$, then $\forall x_1, x_2 \in B(0, D)$ we have for $L \gg D$,

$$\hat{G}(\omega, x_1, x_2) - \overline{\hat{G}(\omega, x_1, x_2)} = \frac{2i\omega}{c_0} \int_{\partial B(0,L)} \mathrm{d}S(y)\overline{\hat{G}(\omega, x_1, y)}\hat{G}(\omega, x_2, y). \tag{5.1}$$

More precisely, (ii) is an approximate identity with an error $O(1/L)$ (cf. [29]).

Using the Helmholtz-Kirchhoff identity one can show that the Green's function can be recovered from cross correlations of ambient noise recordings. The proof relies on the assumption that the noise sources are isotropically distributed on a sphere that surrounds the region of interest [29]. The precise mathematical result is that the time-derivative of the Green's function between two points can be obtained from the cross-correlations of ambient noise recordings at these two points. Specifically, let $u(t, x_1)$ and $u(t, x_2)$ denote the time-dependent wave fields recorded by two sensors at x_1 and x_2 . Their cross correlation function over the time interval $[0, T]$ with time lag τ is given by,

$$\mathrm{CC}_T(\tau, x_1, x_2) = \frac{1}{T}\int_0^T u(t, x_1)u(t + \tau, x_2)\mathrm{d}t, \tag{5.2}$$

we then have that

$$\frac{\partial}{\partial\tau}\mathrm{CC}_T(\tau, x_1, x_2) \simeq G(\tau, x_1, x_2) - G(-\tau, x_1, x_2), \tag{5.3}$$

where G is the Green's function.

This result is obtained given that the integration time T in (5.2) is large enough to guarantee the statistical stability of the cross-correlation function. It was first observed experimentally in [72] where the authors measured the Green's function in a closed cavity using only passive noise recordings due to thermal noise. Their theoretical analysis is based on a normal mode expansion of the displacement and therefore is limited to closed systems.

Another theoretical explanation can be obtained in open systems using stationary phase analysis [62].

We illustrate with a numerical example in Figure 5.1 the cross-correlation of noisy recordings at two sensors located at x_1 and x_2 . We observe that a symmetric function is obtained that has two peaks at the positive and negative lag time that corresponds to the travel-time between the two receivers $\tau(x_1, x_2)$.

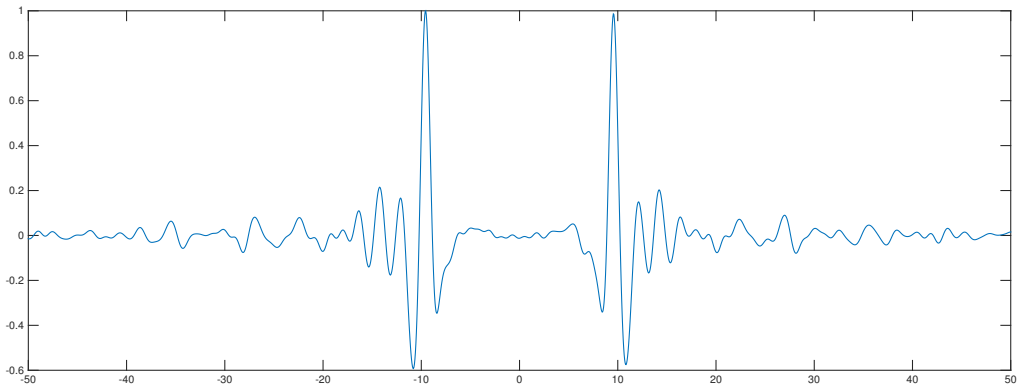

Figure 5.1: An example of the a cross correlation function. The two peaks are located at $-\tau(x_1, x_2)$ and $\tau(x_1, x_2)$.

These results are very important in applications as they suggest that we can recover the Green's function by computing cross correlations of noise recordings. Most importantly we can recover the travel-time $\tau(x_1, x_2)$ from the peaks of the cross-correlations as illustrated at Figure 5.1.

5.3 Eikonal Tomography

Eikonal tomography is a method proposed in [43] that uses the eikonal equation in order to estimate the velocity in the propagation medium from travel-time measurements. To explain the method, let us assume that we have a network of N seismic stations on which we record noise. Let us call r_i one of the sensors that will play at this step the role of the source and call all other sensors r. We compute the cross correlations $\mathcal{CC}_{r_i r}$ between sensor r_i and all sensors r, $r = 1, \ldots, N$ and estimate from the cross-correlations the travel-time surfaces, $\tau(r_i, r)$, for positions r relative to the effective source located at r_i. Eikonal tomography is based on the equation

$$\frac{1}{c_i(r)^2} = |\nabla \tau(r_i, r)|^2 - \frac{\nabla^2 A_i(r)}{A_i(r)\omega^2}, \tag{5.4}$$

where ω is the frequency and A is the amplitude of the wave at position r. Equation (5.4) can be further simplified by assuming that we are in a high frequency regime or that the

spatial variation of the amplitude field is small compared with the gradient of the travel-time surface. We then by dropping the second term of the right side of (5.4), obtain

$$\frac{\hat{k}_i}{c_i(r)} \cong \nabla\tau(r_i, r), \tag{5.5}$$

where c_i is the phase speed for travel-time surface i at position r and $\hat{k}_i$ is the unit wave number vector for the travel-time surface i at position r.

From (5.5) the local slowness can be computed by,

$$s_i(r) = |\nabla\tau(r_i, r)|, \quad i = 1, \ldots, N. \tag{5.6}$$

Since we have as many measurements for the slowness as effective sources r_i, $i = 1, \ldots, N$, we can then calculate the mean slowness,

$$s_o(r) = \frac{1}{N}\sum_{i=1}^{N} s_i(r),$$

and finally the velocity c_0 is,

$$c_o(r) = \frac{1}{s_o(r)}. \tag{5.7}$$

To evaluate the uncertainty of the c_0, we first define the standard deviation of the mean slowness

$$\sigma_{s_o}^2(r) = \frac{1}{N(N-1)}\sum_{i=1}^{N}(s_i(r) - s_o(r))^2,$$

and thus

$$\sigma_{c_o}(r) = \frac{1}{s_o^2(r)}\sigma_{s_o}(r)$$

Our objective is to use this method on seismic noise recordings. To do so we first need to estimate travel-times between pairs of sensors and then compute the local slowness using (5.6). This requires the computation of the gradient of the travel times. The final step is to estimate the velocity from (5.7). In the next sections we explain how we implemented these steps.

5.4 Travel-time estimation

In this section our goal is to estimate the travel-time between pairs of sensors and we will present two techniques for achieving this. The first technique and the most intuitive is to compute the cross correlation for each pair of sensors and estimate the travel-time as the time at which the envelope function of the cross-correlation admits its maximal value. The second one is a bit more evolved and uses the stretching method. In that case, we first estimate travel-time differences between cross-correlations of multiple pairs of sensors and then by inverting the difference operator we obtain the travel-times.

5.4.1 Envelope Function

The cross correlation function (5.2) is a symmetric function assuming a uniform distribution of noise sources and for a large enough T. In geophysics however a uniform distribution of noise sources is usually the exception so we often define the symmetrized cross correlation function which is the average of CC_T over the positive and negative lag times:

$$\mathrm{CC}_{T,sym}(\tau) = \frac{\mathrm{CC}_T(\tau) + \mathrm{CC}_T(-\tau)}{2}, \quad 0 \leq \tau \leq T$$

We then use the envelope function:

$$env(\tau) = |H(\mathrm{CC}_{T,sym}(\tau)| \tag{5.8}$$

where H is the Hilbert transform. Travel-time is estimated as the time t at which the envelope function admits its maximal value. The envelope function is non-negative and has less oscillations than the original signal, therefore it is more convenient for estimating the travel time.

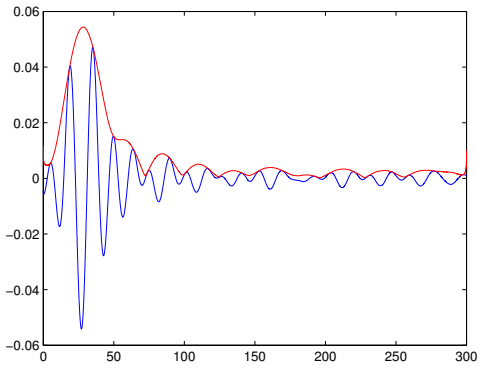

Figure 5.2: An example of the envelope function. The red line represents the envelope function and the travel-time is the time t at which it admits its maximal value. The blue line is $\mathrm{CC}_{T,sym}(\tau)$.

5.4.2 Stretching method for travel-time estimation

An alternative method for estimating the travel-times is based on the stretching method (see chapter 3.1). The idea is to recover travel-times between all available sensors from travel time differences estimated using the stretching method.

Let us consider a random sensor s which will play the role of the source and two other sensors, r and r' which will be the receivers. We compute the cross correlations CC_{sr} between sensor s and r and $\mathrm{CC}_{sr'}$ between sensor s and r' respectively. We obtain two waveforms CC_{sr} and $\mathrm{CC}_{sr'}$, whose travel time difference is denoted $\Delta t^s_{r,r'}$. We want to estimate this

travel-time difference $\Delta t^s_{r,r'}$ using the stretching method which consists in seeking for ε that maximizes the following quantity:

$$C(\varepsilon) = \frac{\int_{t_1}^{t_2} \mathrm{CC}_{sr}(t+\varepsilon)\mathrm{CC}_{sr'}(t)\mathrm{d}t}{\sqrt{\int_{t_1}^{t_2} \mathrm{CC}^2_{sr}(t+\varepsilon)\mathrm{d}t}\sqrt{\int_{t_1}^{t_2} \mathrm{CC}^2_{sr'}(t)\mathrm{d}t}}$$

The next step is to estimate the travel-times from travel-time differences. For each source s, the relationship between the travel-time differences between the receivers and the effective source s and the travel-times from s to the receivers can be written as,

$$Dt^s = \Delta t^s \tag{5.9}$$

where D is a differentiation matrix of size $N \times N(N-1)/2$ (N being the number of sensors), $t^s = (t^s_i)_{i=1\ldots N}$ is the vector of the travel-times for each sensor and $\Delta t^s = (\Delta t^s_{ij} = t^s_j - t^s_i)_{i=1..N, j=1\ldots N}$ is the vector of estimated travel-time differences between receivers.

System (5.9) can be solved with the quasi-Newton method,

$$t^s \approx \tilde{D}^{-1}\Delta t^s,$$

where $\tilde{D}^{-1}$ is the pseudo-inverse of the differentiation matrix D, that can be written as,

$$\tilde{D}^{-1} = (D^T C_D^{-1} D + C_M^{-1})^{-1} D^T C_D.$$

For C_D we use a diagonal matrix whose elements are proportional to the measurement error in Δt^s_{ij} and we choose a second order differentiation matrix for C_M^{-1} [36].

5.4.3 Travel time computations: The fast marching method

When we deal with real measurements, the travel-times between all the available sensors can be estimated using one of the methods suggested in the previous subsections (envelope function or stretching method). However we first consider numerical data and compute the travel-times between pairs of sensors using the fast marching method (FMM). In particular we use an implementation of the multi-stencil FMM (MSFM) [23].

Our computational domain is a square 2-D medium $40km \times 40km$. The wave speed is defined by,

$$\frac{1}{c^2(x)} = \frac{1}{c_0^2}\left(1 + \sigma\mu(\frac{x}{l})\right) \tag{5.10}$$

where $c_0 = 1$Km/s is the mean speed of propagation and μ is a random variable with a Gaussian correlation function, mean zero and standard deviation 1. The strength of the medium variations is determined by σ and l denotes the correlation length which corresponds to the length scale at which the medium fluctuates.

The receivers are random uniformly spread points over our square domain. Using the MSFM method we compute the matrix of travel-times whose i, j element correspond to the travel time from sensor i to sensor j. Note that the travel time matrix is symmetric and has zero on its diagonal.

5.4.4 Interpolation and final calculations

We discussed previously that the sensors are located randomly in the computational domain and so the travel times are estimated on an irregular grid and we want to estimate the velocity using the eikonal equation on a regular grid. In this process we need to compute the gradient of the travel times (see eq.(5.6))and to do so efficiently the approach in [43] proposes the use of a finite difference stencil which requires the interpolation of the travel-times on a regular grid.

Although the interpolation step is systematically overlooked, it is an important source of error in this process. We will test here three interpolation schemes, a triangulation based linear interpolation, a triangulation based cubic interpolation and a spline interpolation. After the interpolation, we can compute the gradient of the travel-times. We implemented a classical finite difference stencil.
Internal nodes:

$$\begin{aligned} F_x(x_i, y_j) &= \frac{F(x_{i+1}, y_j) - F(x_{i-1}, y_j)}{2\Delta x}, \\ F_y(x_i, y_j) &= \frac{F(x_i, y_{j+1}) - F(x_i, y_{j-1})}{2\Delta y}. \end{aligned}$$

Boundary nodes:

$$\begin{aligned} F_x(x_1, y_j) &= \frac{F(x_2, y_j) - F(x_1, y_j)}{\Delta x}, \\ F_y(x_i, y_1) &= \frac{F(x_i, y_2) - F(x_i, y_1)}{\Delta y}, \\ F_x(x_n, y_j) &= \frac{F(x_n, y_j) - F(x_{n-1}, y_j)}{\Delta x}, \\ F_y(x_i, y_n) &= \frac{F(x_i, y_n) - F(x_i, y_{n-1})}{\Delta y}. \end{aligned}$$

It is now useful to recap the process described above into the following algorithm:

Algorithm 5.4.1 *Eikonal tomography implementation steps:*

1. *Travel-time generation (using MSFM).*
2. *Interpolation: from travel-times on the sensors we estimate travel-times on a regular grid.*
3. *Compute the mean slowness from the gradient of travel-times using the finite difference scheme to compute the gradient.*
4. *Compute the velocity estimation using equation (5.7).*

5.5 Results and discussion

We compare the three different interpolation schemes in Figure 5.3. We show the results obtained on a 200×200 grid using linear, cubic and spline interpolation. These are the final

estimation results after applying all the steps of the algorithm. The strength of the medium variations is $\sigma = 0.05$, the correlation length of the medium is $l = 8km$ and we used 400 sensors. As we can see the interpolation error plays a significant role in the reconstruction of the velocity.

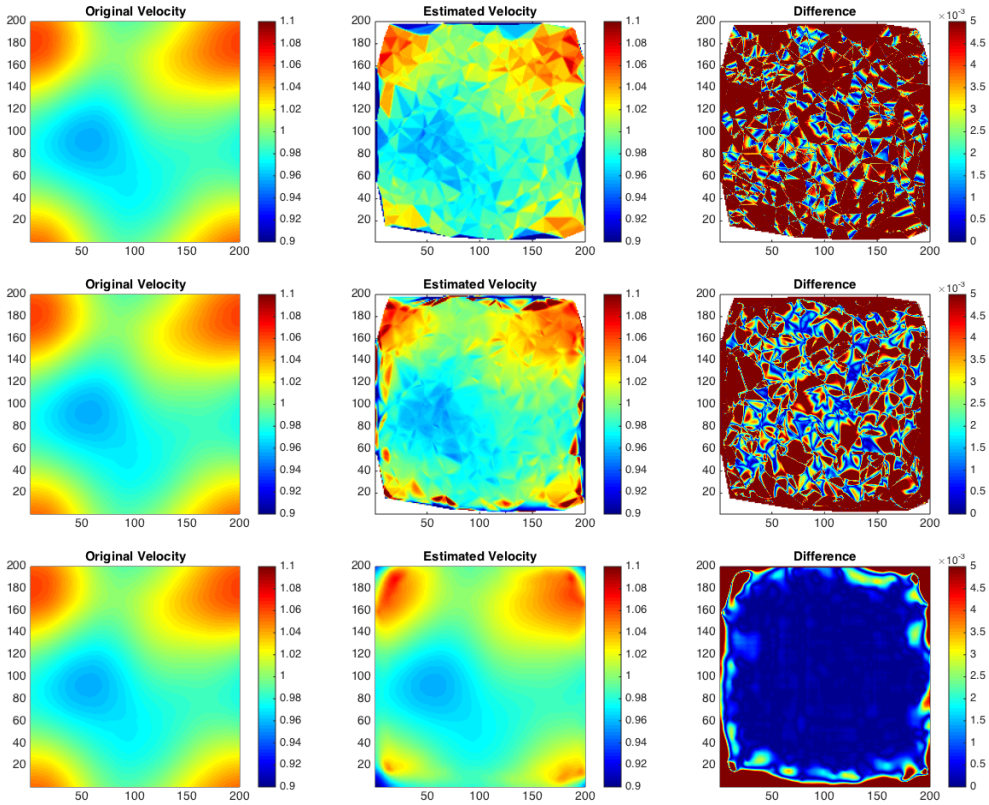

Figure 5.3: Here the first column is the original velocity profile, the second is the reconstructed velocity and the third is the difference between the reconstructed and the original velocity. First row is obtained using the linear interpolation scheme, the second one with the cubic and the third one with the spline interpolation.

The best results are obtained with the spline interpolation method. We fix now the interpolation method to be the spline and we increase the number of sensors. As expected the error decreases by increasing the number of sensors, step by step we increase the number of sensors from 900 all the way to 3600 sensors.

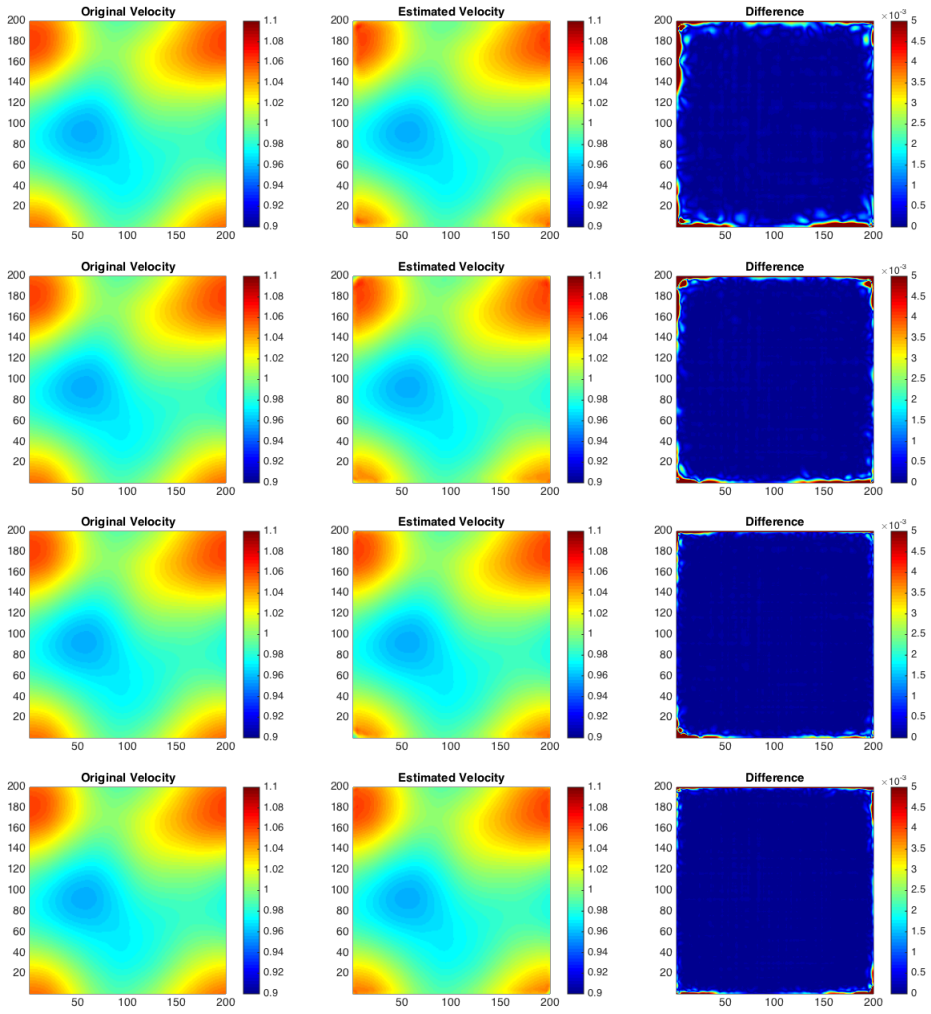

Figure 5.4: We use the spline interpolation for different number of sensors each time and we test the difference between the original velocity and the estimated one for the medium with $8km$ correlation length and 5% variance (see equation (5.10)). From the top to the bottom the number of sensors is 900, 1600, 2500, 3600 respectively.

Furthermore, we want to better quantify the error between the maps of the original velocity and the estimated one. We have a grid with dimensions 200×200. We do not expect a good measurement in the areas that we do not have sufficient coverage so we create a smaller square inside our grid with dimensions $nd \times nd$. We start with $nd = 50$ and we gradually increase it in order to quantify the error as a function of nd. We compute the error in the L_∞-norm and the L_2-norm.

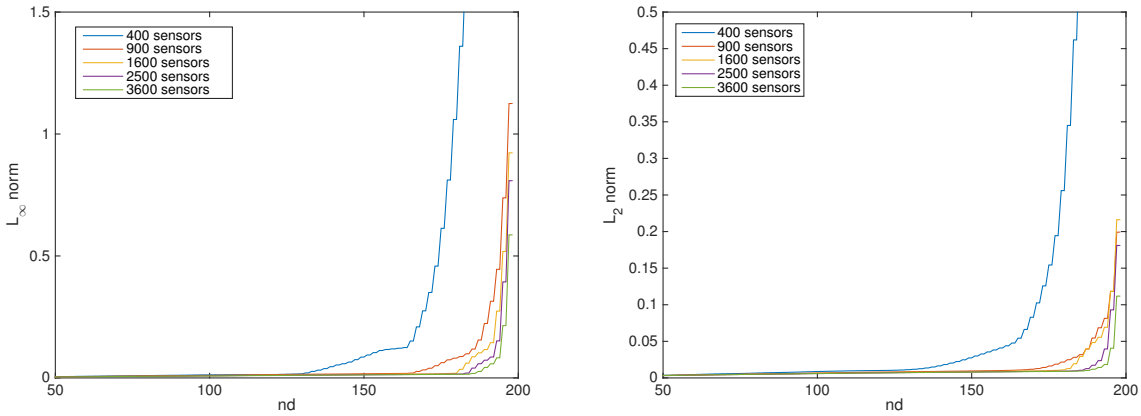

Figure 5.5: On the left picture we plot the error for all the sensors using the $L_\infty - norm$; while on the right one the error using the $L_2 - norm$ is displayed.

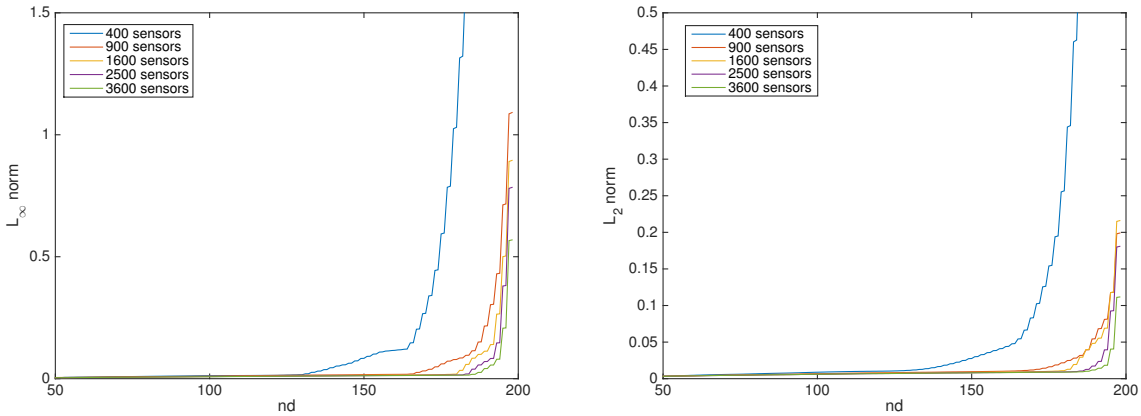

Figure 5.6: On the left picture we see the relative error for all the sensors using the L_∞-norm ; while on the right one the error using the L_2-norm is displayed.

We observe in figures 5.5-5.6 that the error is small for $nd < 150$ and increases for larger nd. However by increasing the number of sensors we measure smaller error for larger nd up to the edge of the domain where the coverage isn't guaranteed even for bigger number of sensors.

We want now to add smaller structures in the velocity profile. We consider the following perturbation of $c(x)$ previously used,

$$\frac{1}{c_p^2(x)} = \frac{1}{c^2(x)} \left(1 + \sigma\mu(\frac{x}{l})\right),$$

with $\sigma = 0.01$ and $l = 1Km$.

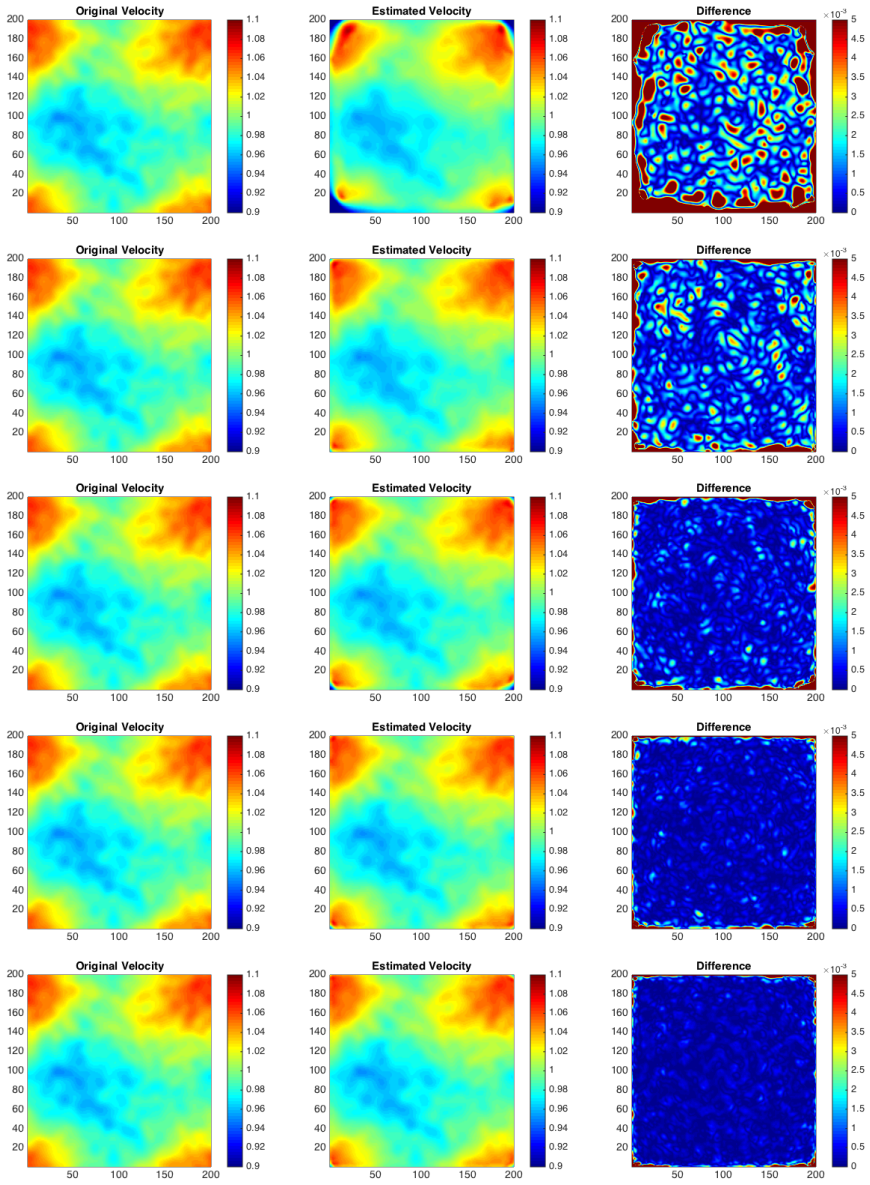

Figure 5.7: We use the spline interpolation for different number of sensors each time to estimate the perturbed velocity profile c_p. From top to bottom the number of sensors is 400, 900, 1600, 2500, 3600 respectively and from left to right are the original velocity, the reconstructed velocity and their difference (absolute value).

In eikonal tomography it is the sensor spacing that controls the accuracy of the method and determines the size of the smaller scale features that can be reconstructed. This is illustrated with the results obtained for the perturbed velocity profile. Indeed as can be

seen by the results of Figure 5.7 the small scale features in $c_p(x)$ cannot be reconstructed with sparse networks of sensors (900 sensors for example). To better quantify the difference between the reconstruction of $c(x)$ and $c_p(x)$ we fix the number of stations to 900 and we measure the error as a function of nd. We observe that the error is significantly larger for the medium with the smaller structures.

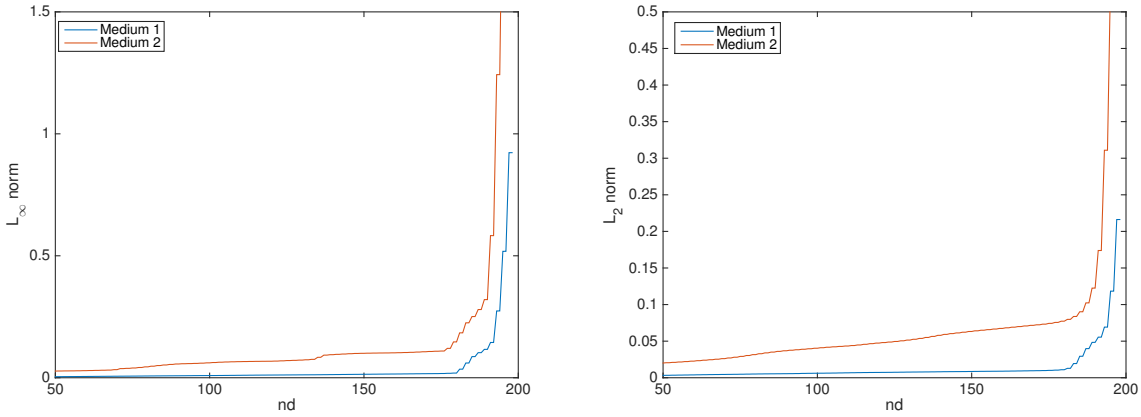

Figure 5.8: On the left picture we compare the error between the two mediums with the $L_\infty - norm$. On the right we plot the error using the $L_2 - norm$.

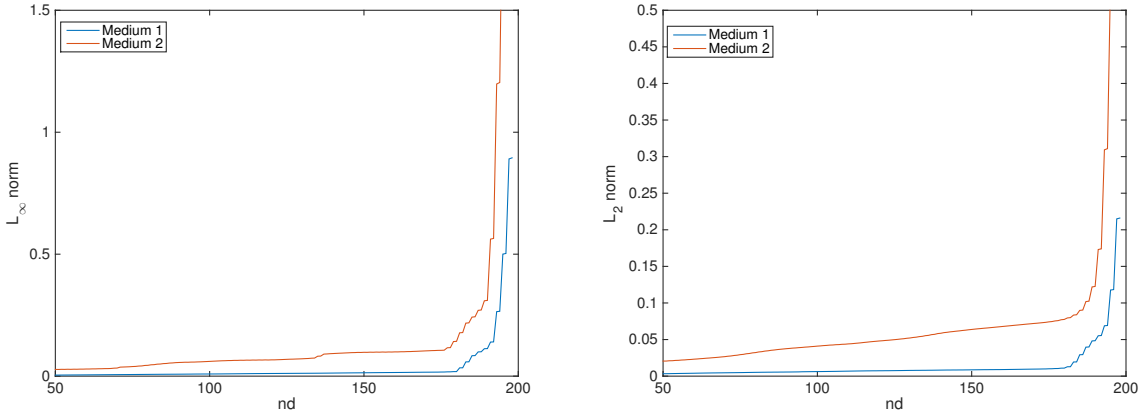

Figure 5.9: On the left picture we compare the relative error between the two mediums with the $L_\infty - norm$. On the right, it is the relative error using the $L_2 - norm$.

5.5.1 Discussion.

In this chapter we had the opportunity to investigate numerically the effectiveness of the eikonal tomography. We showed that in order to be able to reconstruct small scale features

of the medium we have to consider a dense enough network of sensors. We should also note the poor reconstruction of the velocity near the boundary of the domain where the station coverage is not good enough even for an unrealistically large number of sensors. The interpolation scheme played an important role in this process but none of the interpolation schemes tested was efficient for the most realistic number of sensors (400 sensors) especially near the boundary.

Driven from the conclusions of this chapter, we will investigate more advanced interpolation techniques in the next chapter.

Chapter 6

Velocity tomography using statistic interpolation schemes.

In the previous chapter we investigated the velocity tomography problem using the Eikonal Tomography approach as suggested by [43] and we encountered difficulties in reconstructing the velocity near the boundary of the computational domain and more general in areas without good sensor coverage. Also we needed a large number of sensors, at least 400, in order to obtain an acceptable result.

In this chapter we will introduce a modification of the Eikonal Tomography using a statistic interpolation scheme, called Kriging. Our preliminary results are very encouraging and suggest that better reconstructions with a smaller number of sensors can be achieved. This investigation is work in progress.

6.1 Introduction to Kriging

The statistic interpolation method we consider is called "Kriging Interpolation". Kriging is based on Gaussian regression against values of nearby scattered data points, weighted according to statistical relationships among the measured points. One of the advantages of Kriging is that it compensates for the effects of data clustering by assigning to individual points within a cluster smaller weights than to isolated data points. This is expected to improve the reconstruction results in areas with poor sensor coverage.

We will modify the methodology of the previous chapter by changing the steps 2 and 3 of the Algorithm 5.4.1. In step 2 we will use the Kriging interpolation instead of the deterministic methods of the previous chapter and in step 3 we will use the equation (6.3) to calculate the gradient of each travel-time surface instead of the finite difference scheme.

Algorithm 6.1.1 *Eikonal tomography with Kriging implementation steps:*

1. *Travel-time generation (using MSFM),*
2. *Interpolation: from travel-times on the sensors we estimate travel-times on a regular grid using Kriging interpolation,*

3. *Compute the mean slowness from the gradient of travel-times which is estimated using* (6.3).

4. *Compute the velocity estimate using equation (5.7).*

For our computations of the Kriging interpolation, we used the UQlab MatLab package. The first step to implement the Kriging Interpolation using this package is to determine the dependancy rules, in other words, we need to built a model that determines the spatial dependancy of the interpolation weights (using correlation fitting). We then use this model to make predictions at any given point. We seek for predictions over a regular grid.

6.1.1 The model

Now it is necessary to adapt the Kriging interpolation into the Eikonal tomography problem. In Eikonal tomography we are interested (as we did in section 5.3 of the previous chapter) in reconstructing travel-time surfaces from scattered data. For each sensor r_i, also called "effective source", we have estimations of travel times to all the other sensors r_j, $j = 1, 2, \ldots, N$, which are placed in N vectors $\tau(r_i, r_j)$, $r_j, r_i \in \mathbb{R}$, $j = 1, \ldots, N$ and N being the number of sensors. We introduce the functions

$$f_i(r) = \frac{\tau(r_i, r)}{|r_i - r|}, \quad i = 1, \ldots, N, \tag{6.1}$$

so this time we will interpolate these functions instead of the travel-time surfaces $\tau(r_i, r)$. We also do not take into account the points that are closer than 5Km to the virtual source r_i in order to avoid singularities. The choice implies that the velocity will be isotropic and that will eventually give better results. The model for f_i is of the form:

$$\mathbf{F}_i(r) = \beta_i(r) + Z_i(r), \tag{6.2}$$

where Z is a random process with mean zero, variance σ^2, and the covariance selected between a number of different correlation functions (fitting models). The selection of the correlation function, the variance σ^2 and the trend $\beta_i(r)$ is very important. For the trent β_i we select

$$\beta_i(r) = \beta_0(r),$$

where $\beta_0(r)$ is a known constant (in this case the mean (over i) of the observations $f_i(r_j)$, $j = 1. \ldots, N$), this selection of the trent is called "Simple Kriging".

Since we need the local slowness at point r we compute the derivative of the travel-time surfaces at any point of the grid, avoiding the computational cost of applying a finite difference stencil, using the following relationship:

$$\nabla_r \tau(r_i, r) = \frac{r_i - r}{|r_i - r|}\mathbf{F}_i(r) + |r_i - r|\nabla_r \mathbf{F}_i(r). \tag{6.3}$$

The covariance of the random process Z_i is given by

$$C(r, r') = \sigma^2 R(r, r') \tag{6.4}$$

where σ^2 is the variance of the random process. The selection of the appropriate correlation function R is an important decision, and we can choose from a wide spectrum of correlation functions.

Linear correlation function

The most simple correlation function is the linear correlation function given by the formula:

$$R(r, r') = \max\{0, 1 - \frac{|r - r'|}{l_c}\}, \tag{6.5}$$

where l_c is the hypothetical correlation length of the medium.

Exponential correlation function

The next correlation function we consider is the exponential correlation function which is defined by

$$R(r, r') = \exp(-\frac{|r - r'|}{l_c}), \tag{6.6}$$

where again l_c is the hypothetical correlation length of the medium.

Matérn family of correlation functions

Matérn is a family of correlation functions which depends on a shape parameter $\upsilon \geq 1/2$ and is defined by

$$R(r, r'; \upsilon) = \frac{1}{2^{\upsilon-1}\Gamma(\upsilon)}(2\sqrt{\upsilon}\frac{|r - r'|}{l_c})^{\upsilon}\mathcal{K}_{\upsilon}(2\sqrt{\upsilon}\frac{|r - r'|}{l_c}), \tag{6.7}$$

where again l_c is the hypothetical correlation length of the medium, Γ is the Euler Gamma function and K_{υ} is the modified Bessel function of the second kind. We will see results for two Matérn functions, for $\upsilon = 3/2$ and for $\upsilon = 5/2$.

6.2 Results and Discussion

Here we present results of Eikonal Tomography using Kriging interpolation with the correlation functions mentioned above. In the previous chapter we used at least 400 sensors for the deterministic interpolation schemes but in this case we will use only 40 sensors. Using such a small number of sensors is actually a far more realistic scenario since building and maintaining large seismic networks has a very high economic cost.

Another reason to use only 40 sensors in our computations is that any difference between the correlation functions will be more obvious. The number of 40 sensors is a challenging small number with respect to the results of the previous chapter and will be useful to observe the effectiveness of Kriging Interpolation.

6.2.1 Selection of Correlation function

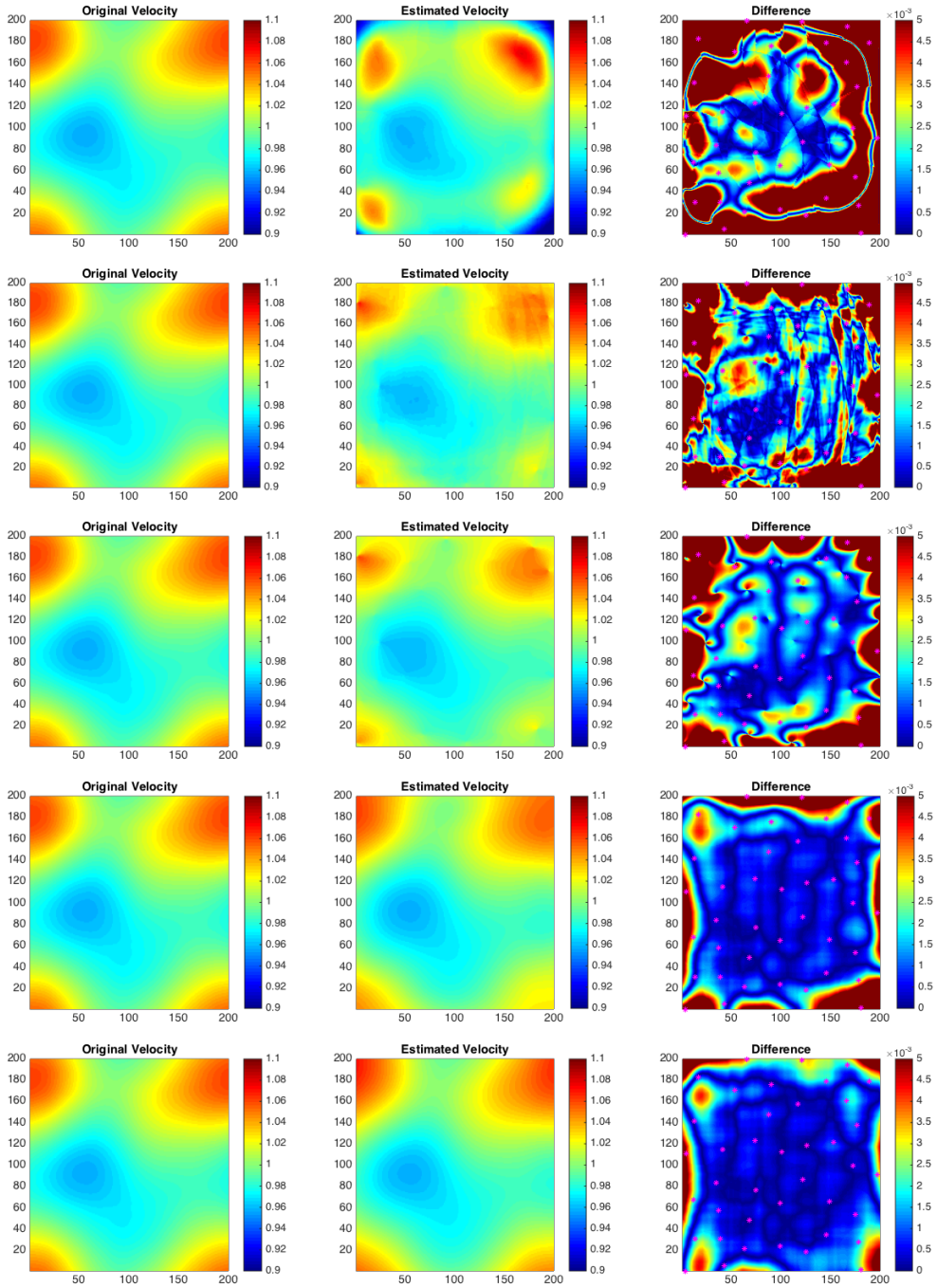

Figure 6.1: Here the first column is the original velocity profile, the second is the reconstructed velocity and the third is the difference between the reconstructed and the original velocity. First row is obtained using the Spline interpolation scheme, the second one with the linear correlation function, the third one with the exponential correlation function, the fourth and the fifth are the Matérn-3/2 and Matérn-5/2 respectively. The pink dots represents the location of the sensors.

The first task is to determine which is the appropriate correlation function to use for the Eikonal Tomography problem. To do so we are using 40 sensors on a $40Km \times 40Km$ domain, the strength of the medium variations is $\sigma = 0.05$, the correlation length of the medium is $l = 8km$ (see equation 5.10). In Figure 6.1 we compare the results obtained with the four Kriging correlation functions with the results obtained using the Spline interpolation. It is clear that Kriging interpolation is far more successful than Spline interpolation for such a small number of sensors. We also observe that the Matérn correlation functions have surprising well reconstructed the velocity especially near the boundary of the domain.

As we can see at Figure 6.2 the Matérn-5/2 provides better reconstruction near the boundary than Spine while it uses 10 times less sensors.

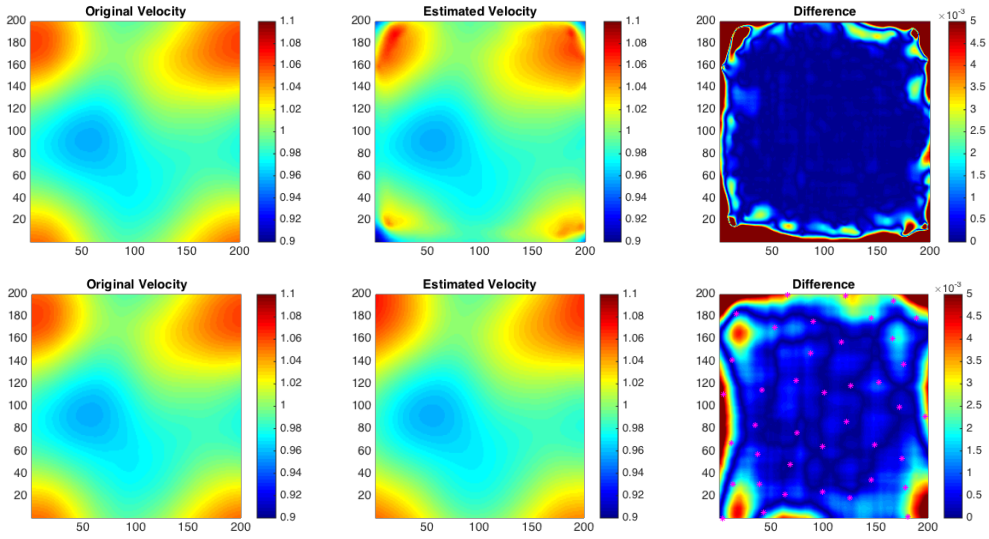

Figure 6.2: Here the first column is the original velocity profile, the second is the reconstructed velocity and the third is the difference between the reconstructed and the original velocity. First row is obtained using the Spline interpolation scheme using 400 sensors, the second one uses the Matérn-5/2 and only 40 sensors.

The results above (Figures 6.1 and 6.2) suggest that the appropriate correlation function is the Matérn-5/2 while the Matérn-3/2 provides good results as well. The Kriging interpolation with linear correlation function and the exponential correlation function, even though they give better reconstructions than the Spline interpolation, they perform worse than the Matérn correlation functions. From now on and until the end of this chapter we will continue to investigate only the Matérn correlation functions given their superiority over the linear and the exponential correlation functions.

Now we increase the number of sensors back to 400 sensors, this will determine if the Matérn-5/2 will continue to give better results than the the Matérn-3/2. It will also also be interesting to see if the Kriging interpolation will continue to perform better for larger number of sensors as expected. In Figure 6.3 we compare the Spline interpolation with the

Kriging interpolation using the Matérn correlation functions with $\upsilon = 3/2$ and $\upsilon = 5/2$ for the same set of 400 sensors.

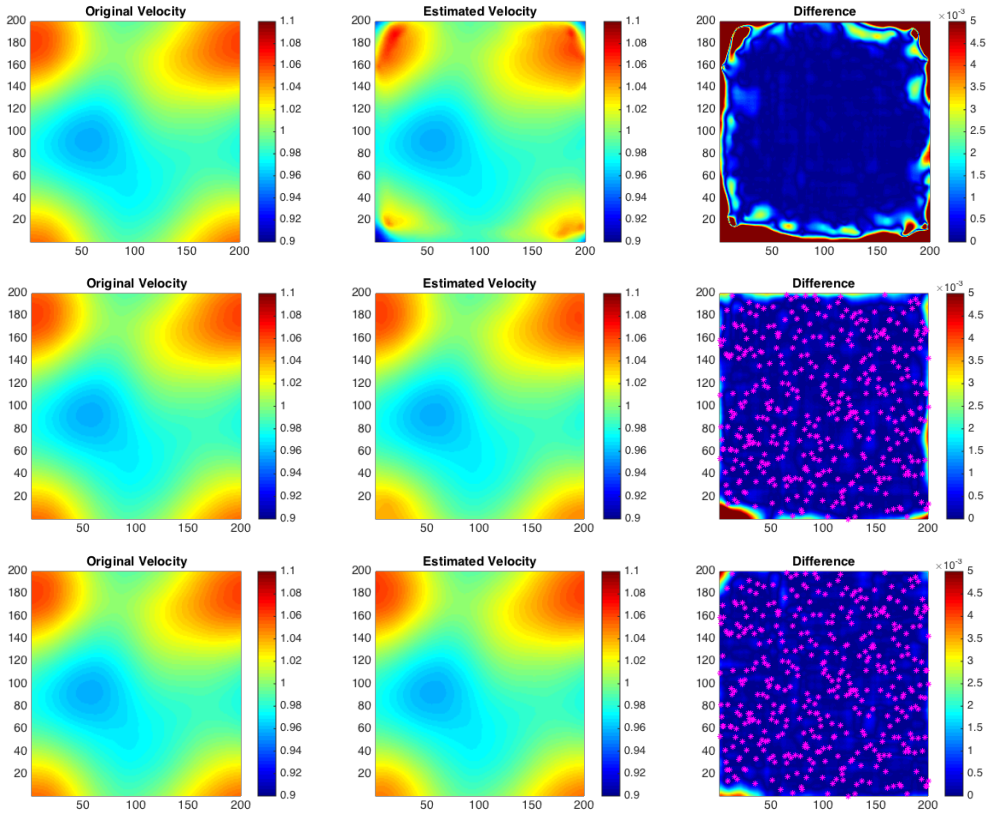

Figure 6.3: Here the first column is the original velocity profile, the second is the reconstructed velocity and the third is the difference between the reconstructed and the original velocity. First row is obtained using the Spline interpolation scheme, the second one uses the Matérn correlation functions with $\upsilon = 3/2$ and the third uses the Matérn correlation function with $\upsilon = 5/2$. All the results are for the same 400 sensors which are represented in pink.

The results in Figure 6.3 confirm once again the superiority of the Kriging interpolation over the deterministic Spline interpolation for the larger set of 400 sensors. We can also observe that in the bottom-left corner of the domain, in which we have a poor sensor coverage even for this number of sensors, we have a better reconstruction from the Matérn-5/2 than the Matérn-3/2.

6.2.2 Reconstruction of small scale velocity details

In the previous sections we were able to show that the Kriging interpolation method with the Matérn correlation function and $\upsilon = 5/2$ gives us the most successful reconstructions of

the velocity model that we used. However that velocity profile lacks of small scale velocity details and we will investigate how the Kriging interpolation performs when we add small scale perturbations to the velocity profile. We use the same medium as the one used in the previous chapter (it has $\sigma = 0.01$ and $l = 1Km$).

We do not expect to reconstruct such small scale details of the velocity profile with only 40 sensors or even with 400 sensors. In the previous chapter we discovered that the sensor density must be at the order of the small scale variations in order to successfully reconstruct them. However, it will be interesting to see how the accuracy of the reconstruction increases with the number of sensors. In Figure 6.4 we can see the reconstruction for different numbers of sensors.

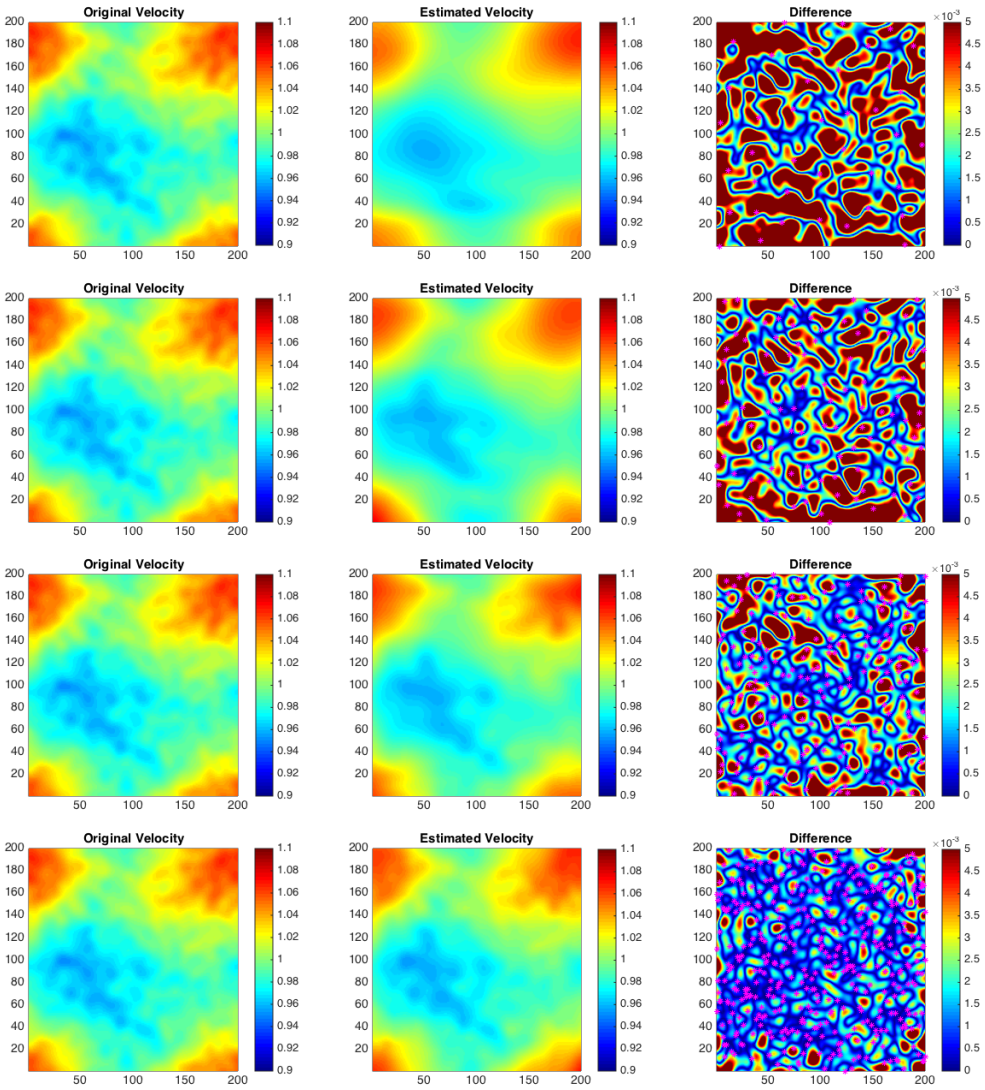

Figure 6.4: Here the first column is the original velocity profile, the second is the reconstructed velocity and the third is the difference between the reconstructed and the original velocity. First row is obtained using 40 sensors, the second is for 100 sensors the third for 200 sensors and the fourth for 400 sensors. All the reconstructions use Kriging interpolation with the Matérn-5/2 correlation function.

We observe in fact that the reconstruction fails to some degree to resolve the fine details of the velocity profile. It gets better and better as the number increases which is expected. Using 40 sensors we get a reconstruction which seems like a smoothed version of the desired velocity profile. When using 400 sensors, we recover most of the details although we still have a lot of error. In Figure 6.5 we compare the Spline interpolation with the Kriging interpolation for 400 sensors.

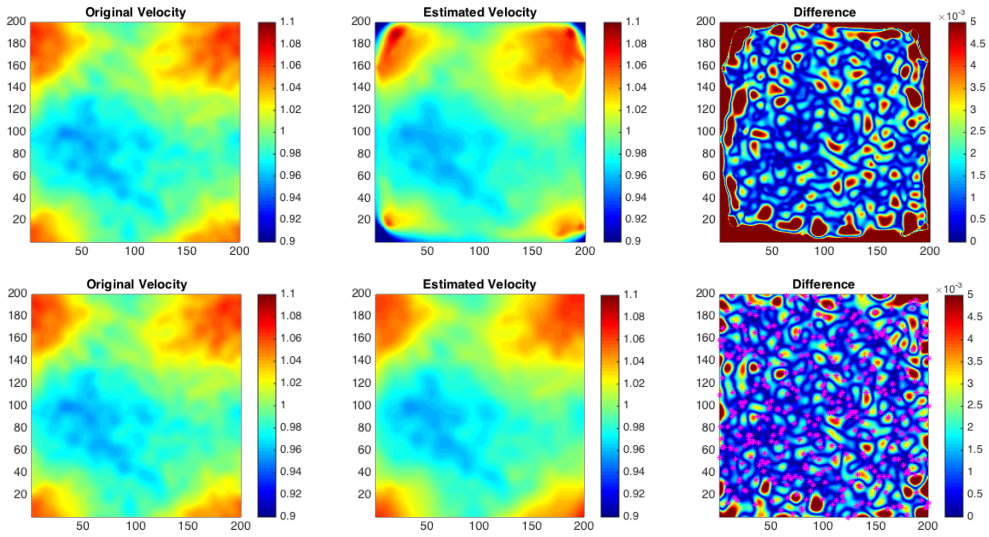

Figure 6.5: Here the first column is the original velocity profile, the second is the reconstructed velocity and the third is the difference between the reconstructed and the original velocity. First row is obtained Spline interpolation, the second uses Kriging interpolation with the Matérn correlation function and the $\upsilon = 5/2$. Both reconstructions contacted on the same set of 400 sensors.

We confirm again that the Kriging interpolation performs better near the boundary in comparison with the Spline interpolation. Also, we observe that Kriging outperforms the Spline interpolation in the interior of the domain as well, as Kriging resolves the small scale details of the velocity profile with a smaller overall error.

6.3 Discussion

In this chapter we studied a modification of the Eikonal tomography method described in the previous chapter. We where able to demonstrate the advantage of using the Kriging interpolation in comparison to the deterministic interpolation methods. These results are preliminary work, and though they are very encouraging, the investigation is still in process.

One of the aspects of the methodology of Eikonal tomography that haven't been studied in this thesis is the actual travel-time measurement. Whenever we process real data from seismic stations we can filter the data in different frequency bands prior to the cross correlation process. The different frequency bands correspond to different travel-paths, typically lower frequencies penetrate deeper in the earth's crust.

Another aspect which is work in process, is the correlation frequency band of the recordings and the detail of the velocity profile we can reconstruct. The common wisdom in this case is, the higher the frequency the smaller the detail we can reconstruct. We are in the process of investigating this claim using noise recordings computed by solving numerically the wave

equation (2.1) in the time domain using the code Montjoie (http://montjoie.gforge.inria.fr/).

As future work we want to investigate the possibility of computing the velocity profile of areas within Greece using data from the National Unified Seismic Network of Greece and the methodology suggested in this chapter.

Part III

Application in structural health monitoring

Chapter 7

The bell tower in Perugia

In this chapter we propose a computationally efficient method for vibration-based structural health monitoring (SHM) of civil structures based on the continuous measurement of their dynamic response in operational conditions. The method is inspired by the stretching technique used in geophysics (see Section 3.1) for detecting variations in the velocity of the earth from seismic noise recordings and follows the current trend of using a very limited number of sensors permanently installed on site for the purpose of damage detection.
In the SHM setting, the proposed method allows to identify small permanent shifts in the natural frequencies of the structure in a changing environment, which is achieved by maximizing the correlation coefficient between a reference waveform, computed in a training reference period in which the structure is assumed to be undamaged, and a shifted version of the same waveform evaluated at the current time. The comparison is performed in the frequency domain and the waveform of interest is obtained from cross-correlations of the ambient vibration measurements. More specifically, in the case of multiple sensors, the waveform can be either the cross-power spectral density of the signals recorded by a pair of sensors, or the largest singular value of the spectral matrix of the measurements. The effect of the environmental fluctuations is mitigated by averaging the cross-correlations in the time domain over a proper period of time, before taking their Fourier transform to estimate the spectral densities. This time domain averaging is carried out in a relatively long period of time for estimating the reference waveform, while it is carried out in a shorter time for estimating the current waveform.
The main advantages of the proposed methodology compared to more traditional vibration-based approaches, such as those based on automated operational modal analysis and multivariate statistical techniques to reduce the effects of changes in environmental and operational conditions, are its lower sensitivity to environmental fluctuations, resulting in a quite shorter training period length, and its lower computational cost, which could be compatible with a direct integration within smart sensors with embedded electronics. The performance of the method is illustrated in the case study of an Italian historical monumental bell-tower that has been monitored for more than one year.

7.1 Introduction

In this chapter we propose a novel vibration-based SHM method with low computational cost, potentially suitable to be implemented without the need for large computational capacities. The method is inspired by the stretching technique, popular in geophysics where it is used to process seismic noise recordings with the purpose of detecting variations in the velocity of the earth. In particular, the method has been used for volcano monitoring and seismic fault monitoring [38, 1, 20]. The proposed Stretching Method (SM) uses continuous recordings of monitoring data ensuing from a small number of sensors installed on site, and provides a direct measurement of changes in natural frequencies of the structure with compensation for environmental effects and without the need for addressing the task of modal identification. This is achieved by searching for a maximum correlation coefficient between the reference first singular value line of the spectral matrix of the measurements and a shifted version of the same quantity evaluated at the current time. A key feature of the method is its very low sensitivity to changes in environmental parameters, which is achieved by averaging cross-correlations in time, before taking their Fourier transforms to estimate the spectral densities.

After presenting the mathematical setting of the method, the paper also illustrates its practical application in the case of a historic masonry bell-tower that has been monitored by the authors for more than one year [66]. The results demonstrate that the stretching method is competitive with other well-established techniques for SHM in terms of minimum detectable frequency shift, while being superior in terms of reduction of computational cost, as well as reduction of the length of the initial training period that is necessary for starting the monitoring task.

The rest of the chapter is organized as follows. First of all, a review of an SHM methodology based on automated modal identification and multivariate statistical analysis is given. Then, the newly proposed strectching method is presented and its main computational advantages in comparison with the reference method are discussed, as well. The second part of the paper presents the application to the case study bell-tower. Finally, the paper is ended with main conclusions.

7.2 Classical method based on changes in natural frequencies

A classical vibration-based SHM methodology is described in this section and used, in the second part of the paper, as a benchmark to demonstrate the effectiveness of the proposed stretching method. The method, here referred to as the "reference SHM method", consists of the continuous modal identification of the structure in operational conditions and on a multivariate statistical analysis of identified natural frequencies, using the tools of Principal Component Analysis (PCA), in order to remove the effects of changes in environmental and operational conditions, and of Novelty Analysis (NA), in order to detect anomalies in the structural behavior possibly related to developing damage pattern. Documented applications

demonstrating the effectiveness of this method can be found, for instance, in [17].
The reference SHM method comprises four different steps, as sketched in Figure 7.1: (i) permanent acquisition of the dynamic response of the structure in operational conditions, (ii) continuous identification and tracking of natural frequencies, (iii) cleansing procedure for removing environmental and operational effects from identified natural frequencies and for the extraction of damage-sensitive features and (iv) novelty analysis for damage detection.
The first step consists in the permanent acquisition of structural vibration signals, typically using accelerometers, and in their remote transmission and storage. The proper choice of sensing hardware and sensors' layout, considering the peculiarities of the monitored structure, are crucial in this stage.
The second step consists of the continuous estimation of the natural frequencies of vibration from acquired vibration signals and on tracking their evolution in time. The adopted output only modal identification technique and its calibration on the basis of the specific case study are essential for the effectiveness of the SHM system.
The third stage aims at processing the identified natural frequencies in such a way to extract quantities that are insensitive to changes in environmental and operational conditions. To this aim, an unsupervised learning technique based on the tool of PCA is adopted. This method consists of the linear remapping of the original natural frequency data into the space defined by the orthonormal basis of the Principal Compontents (PCs) and to the backward transformation to the original space by retaining only some of these PCs. From a mathematical point of view, natural frequencies are first collected in matrix $\mathbf{Y}$, where the row number denotes the order of the mode, while the column number denotes the observation. Then, the following transformation is carried out:

$$\mathbf{X} = \mathbf{T}^T\mathbf{Y} \tag{7.1}$$

where $\mathbf{T} \in \mathbb{R}^{n\times n}$ is termed the "loading matrix", n being the number of identified natural frequencies of the structure. Matrix $\mathbf{T}$ is computed through the singular value decomposition of the covariance matrix of the natural frequencies identified in the so-called "training period", t_0. This last is a reference period during which the structure can be considered undamaged and experiences the normal environmental and operational conditions. After application of Eq. (7.1), the backward transformation is carried out using a dimensionally reduced loading matrix, $\hat{\mathbf{T}} \in \mathbb{R}^{l\times n}$, where only the first l PCs are retained. The following residual error matrix, $\mathbf{E}$, is then computed as

$$\mathbf{E} = \mathbf{Y} - \hat{\mathbf{T}}^T\hat{\mathbf{T}}\mathbf{Y} \tag{7.2}$$

Considering that the PCs provide ordered contributions to the variance of the natural frequencies, if l is sufficiently large, the backward transformation retains most of such variance, which is typically associated to changes in environmental and operational conditions. It follows that matrix $\mathbf{E}$ contains quantities that are almost insensitive to environmental and operational factors, thus being suitable to be used for detecting anomalies in the dynamic behavior of the structure. The crucial aspects in the third stage of the reference SHM method are the choice of the length of the training period, t_0, needed for a proper estimation of

matrix $\mathbf{T}$, and the number of retained PCs, l. Literature results suggest that, in the case of significant environmental effects, t_0 should be equal to about one year, which is a practical limit of the SHM method. The number of retained PCs can be roughly chosen as the number of external factors, e.g., temperature, humidity, wind speed, traffic intensity, and more, that are expected to mostly affect the tracked natural frequencies, but its choice is not unique and generally nothing but trivial.
The fourth step of the procedure consists of the novelty index analysis, finalized at detecting anomalies in the form of statistical outliers in the observed values of the residual errors, Eq. (7.2). This task is pursued by using some proper statistical distance measuring the deviation of the actual value of the residuals with respect to their distribution observed during the training period. In the adopted reference SHM method, the popular T^2-statistical distance is considered and employed as defined in Eq. 7.3 [49]:

$$T^2 = r \cdot (\overline{\mathbf{E}} - \overline{\overline{\mathbf{E}}})^T \cdot \mathbf{\Sigma}^{-1} \cdot (\overline{\mathbf{E}} - \overline{\overline{\mathbf{E}}}) \tag{7.3}$$

where $\overline{\mathbf{E}}$ is the mean of the residuals computed in the subgroup of the last r observations, r being an integer parameter, named group averaging size, while $\overline{\overline{\mathbf{E}}}$ and $\mathbf{\Sigma}$ are the mean values and the covariance matrix of the residuals, respectively, which are statistically estimated in the reference training period, t_0. Under the assumption that a damage produces a change in the distribution of $\mathbf{E}$, it is detected as a stable cloud of values of T^2 greater than a fixed Upper Control Limit (UCL), here statistically defined as the value of T^2 corresponding to a cumulative frequency of 95% in the training period.

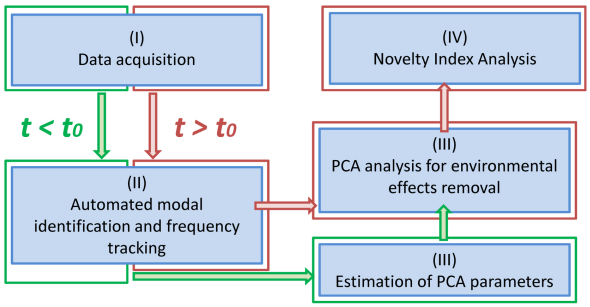

Figure 7.1: Conceptual scheme of the reference SHM method for damage detection highlighting tasks carried out before and after the training period, t_0.

7.3 The new proposed method

As recalled in the Introduction, the SM is widely used in geophysics to detect velocity variations in the earth from seismic noise recordings. In the geophysical context, relative velocity changes, $\mathrm{d}v/v$, are sought in the propagation medium using cross-correlations of noise, recorded at seismic stations. The noise in this context is microseismic activity caused

by natural phenomena, such as the interaction of water waves with the coast. The cross-correlations are time-dependent waveforms, homologous to waves travelling from one station to the other. To be more precise, the key idea that is exploited in SM and, more generally, in passive correlation based techniques [63, 32], is that the impulse response corresponding to the signal received at one point when a delta-pulse is emitted from another point can be obtained from the cross-correlations of ambient noise recordings at the two points. This important result has been observed experimentally in [72] and shown theoretically using different techniques such as stationary phase [62] or the Kirchhoff Helmholtz identity [29]. The main assumption needed is stationarity and uniform distribution for the noise sources, while the propagation medium can be open (unbounded), or finite (bounded), in which case a modal based approach is followed. A nice review is presented in [11] where recent advances in ambient noise seismology are summarized. In the context of SHM, the impulse response function (IRF) of a civil structure (the Factor building in the University of California, Los Angeles) was obtained from cross-correlations of ambient noise recordings in [54]. The obtained IRF was used to compute resonance frequencies and attenuation values which agree with previous obtained estimates for the building. In [54] the authors studied the stability of the IRF and obtained stable results using 14 days of data.

From the mathematical point of view, the following results have been obtained (see chapter 2 in [33] and references therein and Section 2.2 of this Thesis): Let us denote $u(t, x_1)$ and $u(t, x_2)$ the solution of the scalar wave equation (for a generalization to vector wave equations see [64]) at the locations of two sensors x_1 and x_2 due to a random excitation that is stationary in time and uniformly distribute in space. The quantity of interest is the empirical cross correlation of these two signals over a time interval $[0, T]$ with time lag τ,

$$C_T(\tau, x_1, x_2) = \frac{1}{T} \int_0^T u(t, x_1) u(t + \tau, x_2) dt. \tag{7.4}$$

What is important is that the empirical cross correlation C_T is a statistically stable quantity, in the sense that for a large integration time T it is independent of the realization of the noise sources. More precisely, the empirical cross correlation C_T is a self-averaging quantity

$$C_T(\tau, x_1, x_2) \overset{T \to \infty}{\longrightarrow} C^{av}(\tau, x_1, x_2), \tag{7.5}$$

in probability with respect to the distribution of the sources where C^{av} is the expectation of the empirical cross correlation C_T (with respect to the distribution of the sources) which is independent of T

$$C^{av}(\tau, x_1, x_2) = \langle C_T(\tau, x_1, x_2) \rangle \,. \tag{7.6}$$

Assuming Gaussian statistics for the noise sources the covariance of the empirical cross-correlation can be shown to tend to zero with rate $1/T$, which implies that the signal to noise ratio of the cross-correlation, defined as the mean divided by the square root of the variance, is proportional to $\sqrt{T}$. The time interval T that controls the quality of the measured cross-correlation is application dependent and has to be chosen appropriately.

In the application of the SM, it is necessary to compute a reference waveform, which characterizes the medium with no variations and is usually obtained by averaging the cross-correlations over a long period of time, of the order of months. The monitored quantity is the current waveform, computed by averaging the cross-correlations of the measurements over a relatively small interval of time, of the order of days. Averaging the cross-correlations of the noise recordings over time is what controls in practice the statistical stability of the method as explained above. The idea in the stretching method is to estimate the optimal stretch $\mathrm{d}t/t = -\mathrm{d}v/v$ which maximizes the correlation coefficient between the current waveform and the reference one. The correlation coefficient is actually employed in the stretching method as a measure of similarity between the two waveforms.

This paper proposes to exploit the idea of maximizing the similarity between two waveforms in the quite different setting of SHM. The quantities of interest here are also obtained from cross-correlations of the recorded signals in time. The time-interval over which the cross-correlations need to be averaged to obtain the reference waveform can be considered as the training period of the method. On the contrary, the time interval used for averaging cross-correlations in computing the current waveform is related to the time needed for a proper early warning of the damage. As it will be shown later on in the application example, 7-9 days represent a sufficiently long training period to obtain the reference quantity and 12-24 hours are typically enough for building the current waveform.

In application to SHM, it is proposed not to use directly cross-correlation waveforms, but, instead, to take their Fourier transforms after time averaging to obtain the waveforms. Under the assumption that the structure behaves as a linear time invariant system subjected to a multiple input white noise process loading, that is random in space and time, this allows to work with power spectral densities, thereby giving to the shift that is estimated by maximizing the correlation coefficient between the current and reference waveforms, the physical interpretation of a permanent shift in the natural frequency of vibration of the structure. More specifically, potential changes in the natural frequencies of a structure are sought by looking for a shift $\Delta\nu$, in the frequency domain, that maximizes the correlation coefficient C_s defined as,

$$C_s(\Delta\nu) = \frac{\int_{\nu_1}^{\nu_2} A^c(\nu+\Delta\nu)A^r(\nu)\mathrm{d}\nu}{\sqrt{\int_{\nu_1}^{\nu_2}(A^c(\nu+\Delta\nu))^2\mathrm{d}\nu \int_{\nu_1}^{\nu_2}(A^r(\nu))^2\mathrm{d}\nu}}, \tag{7.7}$$

where the frequency dependent functions $A^r(\nu)$ and $A^c(\nu)$ are the absolute values of the Fourier transforms of the reference and current time-averaged cross-correlations, respectively, thereby representing cross power spectral densities of two signals. When more than two sensors are available, it is proposed to define $A^r(\nu)$ and $A^c(\nu)$ as the absolute values of the Fourier transforms of the largest singular values of the cross-correlation matrix averaged in the reference or current period, respectively. In Eq. (7.7), it is assumed that the current quantity is a shifted version of the reference one. By operating in this way and by restricting the integration in the frequency range $[\nu_1, \nu_2]$ containing a single degree of freedom bell function on the first singular value, the estimate of $\Delta\nu$ essentially represents the estimate of a permanent shift in the natural frequency of the structure that is contained in such an

interval. Because different natural frequencies undergo different shifts as a consequence of the occurrence of a damage, different computations are carried out by restricting the integral in Eq. (7.7) in different frequency intervals. It should also be noted that, if the structure has two closely spaced modes, the shifts of the two closely spaced natural frequencies can be computed by separately looking at the first and second singular values. Assuming that the dependence of $\Delta\nu$ on ν is slow, we approximate it by a constant value in each frequency range of interest $[\nu_1, \nu_2]$.

To summarize, the proposed method is fully output only. The computation of the reference cross-correlations requires a few days of measurements and during that period the structure is assumed to be in undamaged conditions. This is analogous to the training period of the classical SHM method described in the previous section. The reference cross-correlations are used for the identification of the natural frequencies of the structure. The monitoring quantity, i.e., the current one, is also computed by averaging the cross-correlations of the measurements but over a smaller period of time. This "local in time" averaging reduces the effect of environmental conditions on the data and increases the sensitivity of the method. Finally, permanent variations in the natural frequencies are monitored by computing $\Delta\nu$ that maximizes Eq. (7.7). Different quantities, A^r, A^c, as well as different frequency ranges of interest $[\nu_1, \nu_2]$, can be defined depending on the natural frequency of the structure that has to be identified and monitored. This is application dependent and will be specified for the particular case considered in this chapter in the next section.

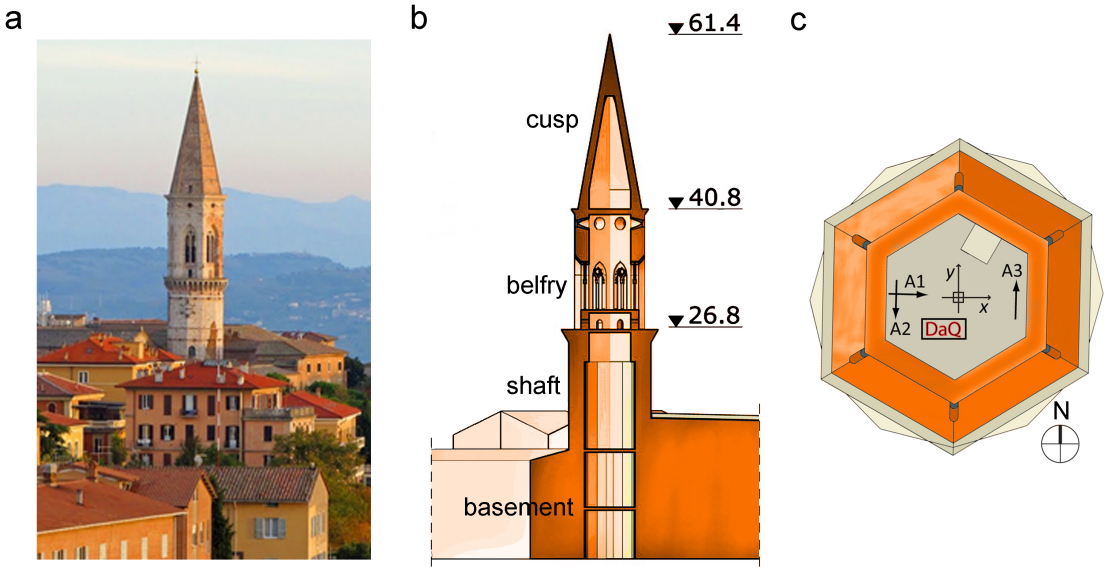

Figure 7.2: The bell-tower of the Basilica of San Pietro and the vibration-based monitoring system (dimensions in m): photography of the tower (a); sectional view with main geometrical information (b); position of the three accelerometers (A1, A2 and A3) and of the data acquisizion system (DaQ) at the base of the cusp at a height of 40.8 m (c).

7.4 Application to a historic bell-tower

7.4.1 The tower

The case study considered in this paper to illustrate the performance of the SM for vibration-based SHM is the bell-tower of the Benedictine Abbey of San Pietro, shown in the photograph of Figure 7.2 (a), that can be considered one of the major monuments of the city of Perugia, Italy. It was built in the 13th century, but was subjected to various interventions in later times, including a total rebuilt at the end of the 14th century and the final restoration in the 15th century. Besides other interventions along the centuries, mostly to repair damages caused by lightnings, those made in the 20th century are especially noteworthy. In particular, in 1932 the metallic structure supporting the four bells at about the three quarters of the shaft was constructed, while in 2002 the damages provoked by the Umbria-Marche Earthquake of 1997, mostly affecting the belfry and the cusp, were repaired.
As shown in the sectional view of Figure 7.2 (b), the total height of the tower is 61.4 m, but the slenderness of the structure is reduced by the surrounding buildings, that restrain the tower up to about 17 m. Four major structural parts can be identified in the structure, namely basement, shaft, belfry and cusp, as depicted in Figure 7.2 (b). The external and internal surfaces of the walls are made of regular stone masonry blocks with some brick replacements, while the internal core of the walls is made of heterogeneous material. The internal surface of the belfry and the external cover of the cusp are made of brick masonry.

7.4.2 The vibration-based monitoring system

A simple vibration-based monitoring system was recently installed on the tower by the authors and continuous monitoring data started to be acquired on December 9th, 2014. The system simply comprises three high sensitivity piezoelectric uni-axial accelerometers model PCB 393B12 (10 V/g sensitivity) and two temperature sensors (thermocouples type K). The accelerometers have been placed at the base of the cusp, with the configuration shown in Figure 7.2 (c), allowing to detect bending vibration modes in the two reference orthogonal directions, x and y, as well as torsional modes. One of the two thermocouples is placed inside the cusp and the other in the belfry, to provide useful data for removing the effects of changing temperature on identified modal properties. However, considering that the SM does not need any information on environmental conditions and so does the reference SHM method, temperature measurements are not used in this work.
Acceleration monitoring data are continuously recorded by means of a data acquisition system composed of a carrier, model cDAQ-9184, and by a NI 9234 data acquisition module having 24-bit resolution, 102 dB dynamic range and anti-aliasing filters. Data are sampled at 40 Hz and stored in separate files in a host computer located inside the tower every 30 minutes. Data processing is carried out remotely, by downloading the data from the host PC located inside the tower using the INTERNET.
The dynamic response of the tower is typically produced by micro-tremors and by wind loading. The tower is also occasionally excited by the four swinging bells that play with a

daily regularity in the early morning.

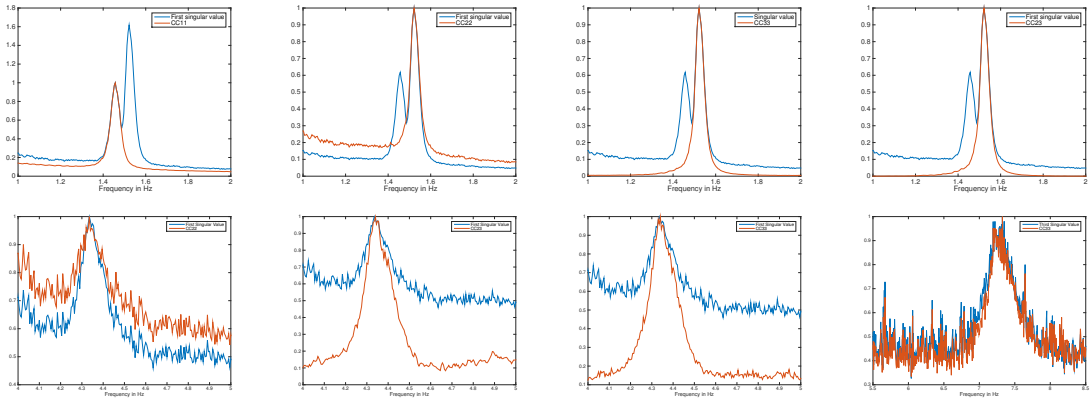

Figure 7.3: Modal values at different quantities. From left to right: (top): 1.46 Hz at the first singular value and $|\mathbb{CC}_{11}(\nu)|$, 1.51 Hz at the first singular value and $|\mathbb{CC}_{22}(\nu)|$,$|\mathbb{CC}_{33}(\nu)|$,$|\mathbb{CC}_{23}(\nu)|$. (bottom): 4.33 Hz at the first singular value and $|\mathbb{CC}_{22}(\nu)|$, $|\mathbb{CC}_{23}(\nu)|$, $|\mathbb{CC}_{33}(\nu)|$ and the 7.3 Hz at the third singular value and the $|\mathbb{CC}_{33}(\nu)|$. NOTE: all the quantities at this figure are normalized by their maximum.

7.4.3 Data processing for SHM: reference method

In the reference SHM method, automated modal identification is carried out by a Stochastic Subspace Identification (SSI) procedure [51, 67], ad hoc implemented in a MatLab [65] code and applied to each file containing 30-minutes of structural response sampled at 40 Hz. In SSI calculations, models of order ranging from 40 to 60 with step increments of 2 are identified in each data set, by varying the number of output block rows of the block Henkel matrix of the output acceleration data from 140 to 200 with step increments of 10. A procedure for noise modes elimination and clustering of the modes is then applied to extract the mean values and confidence intervals of the identified modal properties. A modal tracking procedure is finally applied to identified modal properties, in such a way to track their evolution in time on the basis of their similarities. For the details on the modal identification procedure, the interested reader is referred to [67].

7.4.4 Data processing for SHM: stretching method

The data of each measurement file containing 30-minutes of structural response sampled at 40 Hz are filtered using a bandpass filter in the frequency range $[0.1 - 12.0]$ Hz. From the filtered data we compute the cross-correlation matrix whose elements $\mathbb{CC}_{i,j}$, $i, j = 1, \ldots, 3$ are,

$$\mathbb{CC}_{i,j}(\tau) = \frac{1}{T}\int_0^T d_i(t+\tau)d_j(t)\mathrm{d}t, \quad i, j = 1, \ldots, 3. \tag{7.8}$$

Here $d_i, \quad i = 1, \ldots, 3$ are the data recorded at the three accelerometers and T is the length of the recordings. We only store the central 200s long part of the cross-correlations which corresponds to a frequency sampling rate of 0.005Hz.

Building the reference quantities

The SM requires two quantities: the reference and the current one. Using the cross-correlations computed above we first build the reference quantity using all the available data which correspond to a period of six months. Remark that in practice we do not need such a long period to compute the reference quantity. As we will see in the following, averaging over one week of data is sufficient for the purposes of SHM. The averaging process is done in the time domain. Then, using the fast Fourier transform (FFT) algorithm we obtain the reference spectral matrix $\mathbb{CC}^r(\nu)$ whose i, j element $[\mathbb{CC}^r(\nu)]_{i,j} = \mathbb{CC}^r_{i,j}(\nu)$ is the Fourier transform of the cross correlation function between the signals recorded by sensors i and j at frequency ν. To identify the modal frequencies we apply the simple Frequency Domain Decomposition (FDD) technique, performing the singular value decomposition of the 3×3 matrix $\mathbb{CC}^r(\nu)$ frequency by frequency. Since $\mathbb{CC}^r(\nu)$ is symmetric, it admits a symmetric SVD (which is the same as the eigenvalue decomposition)

$$\mathbb{CC}^r(\nu) = U(\nu)\Sigma(\nu)U^T(\nu) \tag{7.9}$$

where by $U^T(\nu)$ we denote the transpose of $U(\nu)$. The matrix $\Sigma(\nu)$ is a real diagonal matrix with the singular values (eigenvalues) placed on the diagonal. Assuming that the eigenvalues are ordered from largest to smallest, we denote them as $\sigma_1(\nu) > \sigma_2(\nu) > \sigma_3(\nu)$.

Modal identification

By inspection of the singular values of the $\mathbb{CC}^r$ matrix, as well as amplitudes of the matrix elements $\mathbb{CC}^r_{ij}$, it was possible to identify five natural frequencies, that are in good agreement with the mean values of those identified by SSI during monitoring, as described in [66] and as reported in Table 7.1. In Figure 7.3 we can see that all the natural frequencies are present in more than one quantity. Moreover, the first two natural frequencies, which are closely spaced, both appear in the largest singular value, $\sigma_1(\nu)$, which makes their monitoring more difficult if one selects $\sigma_1(\nu)$ as the quantity of interest. Instead, we propose to monitor the first natural frequency using $|\mathbb{CC}_{11}(\nu)|$ and the second one using $|\mathbb{CC}_{22}(\nu)|$. We also observe that the third natural frequency can be monitored using $|\mathbb{CC}_{23}(\nu)|$ or $|\mathbb{CC}_{33}(\nu)|$ since these are the quantities in which the third natural frequency is observed with higher signal to noise ratio (SNR). The fifth natural frequency can be monitored using either $|\mathbb{CC}_{33}(\nu)|$ or $\sigma_1(\nu)$. The natural frequency of 4.9Hz is present in $|\mathbb{CC}_{12}(\nu)|$ but with a lower SNR than the other ones.

Mode number	f_m by SSI [Hz]	f_m by SM [Hz]	Mode Type
1	1.47	1.46	Fx1
2	1.53	1.51	Fy1
3	4.34	4.33	T1
4	4.96	4.90	Fy2
5	7.28	7.30	Fy3

Table 7.1: Mean natural frequencies of the bell-tower, f_m, identified by SSI during the monitoring period from December 10-th 2014 to February 29-th 2016 and compared to those obtained by the SM building the reference quantities by time averaging in the period from 28 Oct 2014 to 1 April 2015 (in mode type F and T stand for flexural and torsional, respectively, the number of the modal order and x and y are the reference axes in Figure 7.2).

7.5 Results and discussion

7.5.1 Frequency tracking by the stretching method

In order to illustrate the performance of the SM, it is demonstrated, at first, that it allows tracking the time evolution of the natural frequencies of a structure and, in particular, to closely identify frequency shifts due to changes in environmental conditions. To this aim, the first natural frequency of the bell tower, at 1.46Hz, is considered. The reference quantity $|\mathbb{CC}^r_{11}(\nu)|$ is used for tracking this natural frequency and built as described above using five months of monitoring data. The current quantity, $|\mathbb{CC}^c_{11}(\nu)|$, is instead computed using consecutive data windows corresponding to a 30 minute long file.

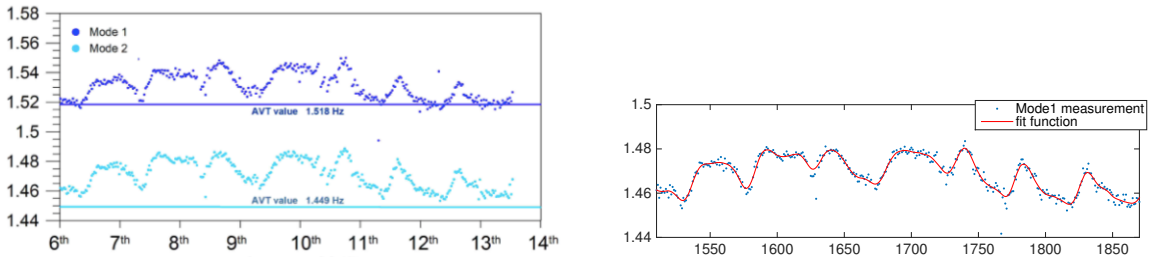

Figure 7.4: The comparison between the results of the reference SHM method and the stretching method. We monitored the natural frequency at 1.46 Hz using $|\mathbb{CC}_{11}(\nu)|$.

The frequency range used for the SM, Eq. (7.7), has been chosen as $[\nu_1, \nu_2] = [1.3\ ,\ 1.7]$Hz. The result of the SM is the value of $\Delta\nu$ that, at the current time, maximizes the correlation between the reference and the current waveforms. Such $\Delta\nu$ can be interpreted as the shift between the current natural frequency of the structure and its average value in the reference period, f_m, obtained from the peak of the reference waveform. It follows that the current natural frequency can be estimated as $f_m + \Delta\nu$. Figure 7.4 shows a typical comparison between the current natural frequency of mode Fx1 estimated by the SM in a few consecutive

days and the same natural frequency independently estimated by the automated output only SSI-based modal identification procedure presented above. The results highlight a very good match between the two estimates and confirm that the SM is a convenient alternative to SSI for frequency tracking. It should be noted that the relatively large daily oscillations exhibited by natural frequency time series are associated with the effects of changing environmental conditions and, primarily, of ambient temperature.

7.5.2 Statistical properties of Stretching Method

Having demonstrated that the SM can be used for frequency tracking, where no reduction of environmental variations is carried out, the statistical properties of the method are now investigated in order to obtain compensation of such environmental effects. To do so, the first quantity of interest is the correlation coefficient, C_s, defined by Eq. (7.7), which is a measure of similarity between the current and the reference waveforms. The current quantity used to produce the results in Figure 7.4 was obtained by cross-correlating data recorded over 30min (one data window). Instead, if the number of data windows used to compute the current cross-correlation is increased, changes in the estimated quantity, $\Delta\nu$, are reduced, which means that the effects of changes in environmental conditions are mitigated. With the purpose of achieving a proper compensation of such environmental effects, it is therefore of interest to investigate how the estimate of $\Delta\nu$ is affected by the number of data windows (30min data sets) used for computing the current quantity.

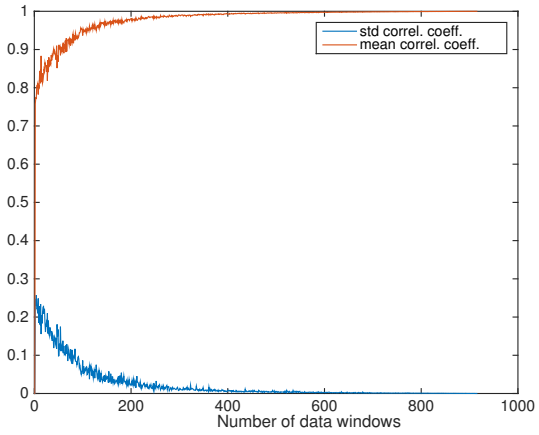

Figure 7.5: The mean and the standard deviation of the correlation coefficient between the reference $|\mathrm{CC}^r_{11}(\nu)|$ and the current $|\mathrm{CC}^c_{11}(\nu)|$ obtained using an increasing number of data windows. The frequency interval is $[1.3 - 1.7]$ Hz.

To this aim, the mean and the standard deviation of the correlation coefficient between the reference $|\mathrm{CC}^r_{11}(\nu)|$ and the current $|\mathrm{CC}^c_{11}(\nu)|$ waveform are computed, at first, by increasing the number of data windows used for the computation of $|\mathrm{CC}^c_{11}(\nu)|$. The plot in Figure 7.5 is obtained using 100 realizations of the current quantity for each value of randomly (not

serially) selected data windows. As shown in Figure 7.5 the mean of the correlation coefficient increases with the number of data windows, while its standard deviation decreases. This implies that the similarity between the two waveforms improves as more data sets are used for estimating the current quantity and that, in other words, the quality of the measured variation, $\Delta\nu$, improves.

The second quantity of interest in the investigation of the statistical properties of the SM is the actual measurement, $\Delta\nu$, of the frequency shift. In this regards, the results presented in Figure 7.6 show that the standard deviation of $\Delta\nu$ decreases as the number of data sets used to compute the current cross-correlation is increased and so does the mean value of $\Delta\nu$. These results, obtained by using $|\mathbb{CC}_{11}(\nu)|$ and the band [1.3 , 1.7]Hz in Eq. (7.7), demonstrate that increasing the number of data sets results in $\Delta\nu$ being less sensitive to variations in environmental conditions. In order to further illustrate this result, Figure 7.7 shows a comparison of $f_m + \Delta\nu$ as obtained by the SM measurement using single data sets and 48 data sets (1 day) to build the current quantity. These results show that the estimate of $\Delta\nu$ is much more stable and relatively insensitive to environmental conditions as the number of data sets is increased.

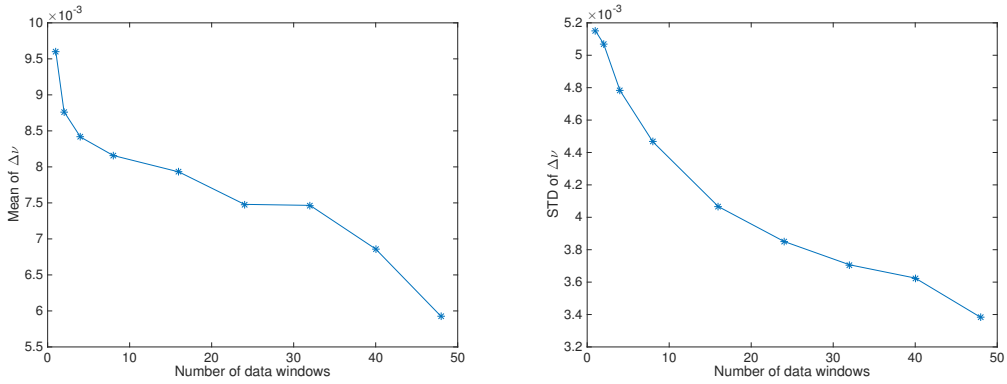

Figure 7.6: The mean and the standard deviation of the measurement $\Delta\nu$ for the first modal value, with the stretching method, using a different number of data windows to obtain $|\mathbb{CC}^c_{11}(\nu)|$.

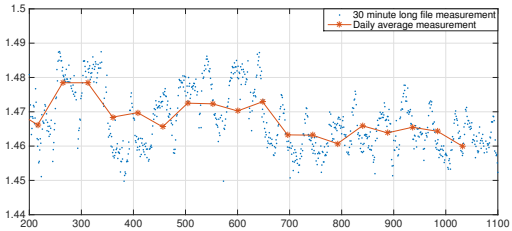

Figure 7.7: The measurement of the 1.46 Hz modal value using 48 data windows (1-day) to build the current quantity of $|\mathbb{CC}^c_{11}(\nu)|$ and comparison with the single 30 minute long file.

One of the main advantages of the SM is the small amount of time required to build a reliable reference quantity, that is, the relatively short length of the training period of the method. Indeed, the results of Figure 7.5 show that 7 to 9 days (336 to 432 data windows) represent a sufficiently long training period to build a reference quantity that is quite similar to the one that has been built using the entire six month period of data. In order to further illustrate the stability of the current quantity when appropriately averaged, Figure 7.8 shows a plot of the current largest singular value line of the spectral matrix, computed using one week of data in winter and one in summer for the purpose of time averaging of cross-correlations. These results show that the plots are quite similar and that the actual value of the 1.46Hz modal frequency remains the same.

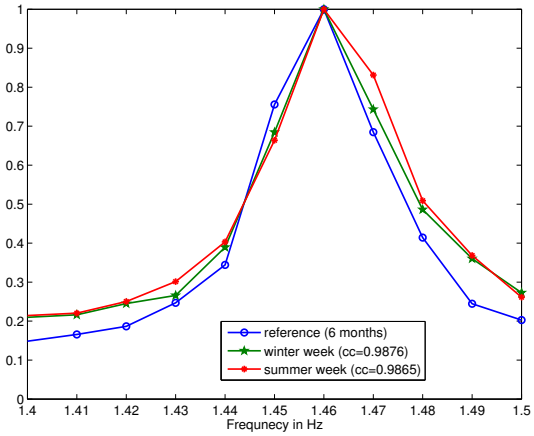

Figure 7.8: The reference cross-correlation compared to two current ones obtained using one week of data during summer and winter. The value of cc is the correlation coefficient between the reference and the current quantities.

7.5.3 Detection of permanent natural frequency shifts.

The final purpose of the SM proposed in this paper is allowing detection of small permanent natural frequency shifts that could be associated with a change in the structural behavior, such as a developing damage pattern. To this aim, analyses are carried out in this section by artificially inserting permanent frequency shifts in the monitoring data and then checking for their detectability by the SM.

For each 30 minute long file that belongs in the period we want to add the artificial shift we perform the following steps: First we compute the singular value decomposition (see equation (7.9)). We then define the modified singular values $\widetilde{\sigma}_i(\nu)$ by introducing a shift $\delta\nu$ as:

$$\widetilde{\sigma}_i(\nu) = \sigma_i(\nu + \delta\nu), \quad i = 1, 2, 3 \,, \tag{7.10}$$

for all frequencies in the interval $[\nu_1, \nu_2] = [1.3 \ , \ 1.7]$Hz. The last step is to recompose the correlation matrix using again the equation (7.9) with the modified singular values, *i.e.*,

using $\widetilde{\Sigma}(\nu)$ instead of $\Sigma(\nu)$. The elements of this modified correlation matrix are used for estimating the artificially introduced shift.

The SM reveals to be very powerful in terms of its sensitivity, i.e., its ability to allow detection of very small permanent changes in $\Delta\nu$. The sensitivity of the SM actually depends on the current quantity and the number of data windows used to build it. This is shown in the results of Figure 7.10 (left plot), which contains plots of the relative error in the estimation of permanent frequency shifts of increasing magnitude by varying the number of data sets used for building the reference quantity. The relative errors are computed over 150 measurements and for 4 different values of $\Delta\nu$. The results of Figure 7.10 demonstrate that the accuracy in the estimation of $\Delta\nu$ increases as the number of data windows used for the computation of the current quantity is increased. Here we used 5 months of data for the reference quantity.

To further illustrate this we plot in Figure 7.9 the time history of the raw, modified and estimated value of the first natural frequency for a period of 25 days. The modified data are obtained by introducing a shift from day 75 and on. For the plot on the left we inserted a shift of 1% in the first natural frequency and we estimated it using one day of data for the current quantity. For the right plot we decreased the shift to 0.1% and increased the number of days to 4 for the computation of the current quantity. In both cases we used 5 months of data for the computation of the reference quantity. We observe that by increasing to 4 the number of days used for the computation of the current quantity, the oscillations in the value of the first natural frequency decrease significantly and we can estimate very accurately a permanent shift of 0.1%.

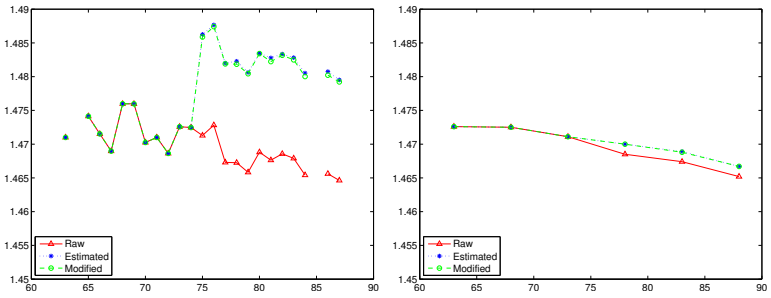

Figure 7.9: Time history of the raw, modified and estimated value of the first natural frequency for a period of 25 days where we introduce a shift from day 75 and on. We use 5 months of data for the computation of the reference quantity. For the plot on the left we insert a shift of 1% in the first natural frequency and we estimate it using one day of data for the current quantity while for the right plot we decrease the shift to 0.1% and increase the number of days to 4 for the computation of the current quantity. In both cases the estimation of the frequency shift is very good.

More quantitively, the results of Figure 7.10 (right plot) demonstrate that, for the considered case study, a shift $\Delta\nu = 0.0625$Hz of the first natural frequency can be detected with a relative error of less then 1% using 5 months for computing the reference quantity,

2 weeks for computing the current quantity and using one single acceleration sensor. The smallest permanent perturbation that can be detected using two weeks of data for computing the current quantity is $\Delta\nu = 0.0156$Hz, which is limited by the frequency sampling rate of 0.005Hz adopted in the presented case study. This can be further reduced to detect even smaller frequency variations if deemed necessary.

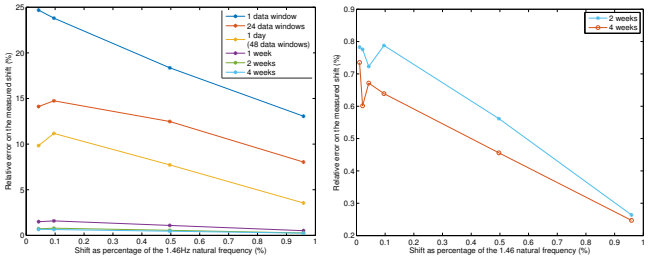

Figure 7.10: Statistically measured relative error on the measured shift, $\Delta\nu$, for four values of added shift, computed using an average over 150 measurements. The current quantity, $|\mathbb{CC}^c_{11}(\nu)|$, is computed using one (blue), 24 (red), 48 (orange) data windows, 1 week (purple), 2 weeks (green) and 4 weeks (light blue)of data. We observe that the accuracy of the method increases as we increase the number of data windows used in the computation of $|\mathbb{CC}^c_{11}(\nu)|$. The relative error of the method also decreases as the value of the actual variation that we are seeking for increases. On the right we plot only the results using 2 and 4 weeks of data for smaller values of shifts. The relative error remains below 1% for all the considered values of shifts.

7.6 Conclusions

We have proposed a novel method for vibration-based SHM of civil structures, which has been inspired by the stretching technique that is commonly adopted in geophysics for revealing variations in the velocity of the earth using seismic noise recordings.

The proposed method is based on continuous measurements of the dynamic response of a structure, typically using a small number of sensors installed in the field, and allows to track the evolution in time of the natural frequencies of vibration of the same structure with proper compensation for environmental effects. This is achieved by maximizing the correlation coefficient between a reference quantity, expressed in the frequency domain, and a shifted version of the same quantity evaluated at the current time. This results into a single-parameter maximization problem, where the parameter is the frequency shift that is introduced in the current quantity. By a proper choice of the quantity of interest, this shift results to be an estimate of the deviation of a natural frequency with respect to normal conditions, and can thus be used as a damage sensitive feature. To this aim, we propose to use the first singular value of the spectral matrix of the measurements as the quantity of interest.

In order to illustrate its performance, the proposed method has been applied to the case study of a continuously monitored historic masonry bell-tower in Italy. The results have

shown that the stretching method is able to allow detection of frequency shifts of the order of 0.1%, which are comparable with frequency shifts that can be detected by well-known multivariate statistical analysis techniques applied to time series of automatically identified modal frequencies. However, the stretching method has demonstrated superior performance in terms of length of the training period, as a few days were seen to be sufficient to properly estimate the reference singular value line and to compensate for environmental effects. Furthermore, the stretching method is far less computationally demanding in comparison to approaches based on automated modal identification, as it basically skips the task of modal identification and modal tracking. This circumstance would allow an easy implementation of the method within smart sensors with embedded electronics for on-board and online computations, in a general framework of real time structural health monitoring.

In conclusions, the proposed stretching method is seen to be a convenient alternative to existing signal processing techniques for vibration-based structural health monitoring, with advantages in terms of drastic reduction of the training period length and of computational burden.

Bibliography

[1] D. Acarel, F. Bulut, M. Bohnhoff, and R. Kartal. Coseismic velocity change associated with the 2011 van earthquake (m7.1): Crustal response to a major event. *Geophys. Res. Lett.*, 41:4519–4526, 2014.

[2] K. Aki. Space and time spectra of stationary stochastic waves, with special reference to microtremors. *Bull. Earthquake Res.*, Inst. 35:415–457, 1957.

[3] A. Alvandi and C. Cremona. Assessment of vibration-based damage identification techniques. *J Sound Vib*, 292(1-2):179–202, 2006.

[4] Andrea Bellino, Alessandro Fasana, Luigi Garibaldi, and Stefano Marchesiello. Pca-based detection of damage in time-varying systems. *Mech Syst Signal Proc*, 24:2250–2260, 2010.

[5] G. D. Bensen, M. H. Ritzwoller, M. P. Barmin, A. L. Levshin, F. Lin, M. P. Moschetti, N. M. Shapiro, and Y. Yang. Processing seismic ambient noise data to obtain reliable broad-band surface wave dispersion measurements. *Geophysical Journal International*, 169:1239–1260, 2007.

[6] James G Berryman. Analysis of approximate inverses in tomography i. resolution analysis of common inverses. *Optimization and Engineering*, 1(1):87–115, 2000.

[7] A. Brencich and D. Sabia. Experimental identification of a multi-span masonry bridge: the tanaro bridge. *Constr Build Mater*, 22:2087–2099, 2008.

[8] F. Brenguier, M. Campillo, C. Hadziioannou, N. M. Shapiro, R. M. Nadeau, and E. Larose. Postseismic relaxation along the San Andreas fault at Parkfield from continuous seismological observations. *Science*, 321(5895):1478–1481, 2008.

[9] F. Brenguier, N. M. Shapiro, M. Campillo, V. Ferrazzini, Z. Duputel, O. Coutant, and A. Nercessia. Towards forecasting volcanic eruptions using seismic noise. *Nature Geoscience*, 1(2):126–130, 2008.

[10] JMW Brownjohn. Structural health monitoring of civil infrastructure. *Phil. Trans. R. Soc. As.*, 365(1851):589–622, 2007.

[11] M. Campillo and P. Roux. 1.12 - crust and lithospheric structure - seismic imaging and monitoring with ambient noise correlations. In Gerald Schubert, editor, *Treatise on Geophysics (Second Edition)*, pages 391 – 417. Elsevier, Oxford, second edition edition, 2015.

[12] Michel Campillo, Haruo Sato, Nikolai M. Shapiro, and Robert D. van der Hilst. New developments on imaging and monitoring with seismic noise. *C. R. Geoscience*, 343(8–9), 2011.

[13] Filippo Casarin and Claudio Modena. Seismic assessment of complex historical buildings: Application to reggio emilia cathedral, italy. *Int J Archit Herit*, 2(3):304–327, 2008.

[14] Sens-Schönfelder Christoph and Larose Eric. Lunar noise correlation, imaging and monitoring. *Earthquake Science*, 23(5):519–530, 2010.

[15] D. Clarke, L. Zaccarelli, N.M. Shapiro, and F. Brenguier. Assessment of resolution and accuracy of the moving window cross spectral technique for monitoring crustal temporal variations using ambient seismic noise. *Geophys. J. Int.*, 186:867–882, 2011.

[16] Andrea Colombi, Julien Chaput, Florent Brenguier, Gregor Hillers, Philippe Roux, and Michel Campillo. On the temporal stability of the coda of ambient noise correlations. *Comptes Rendus Geoscience*, 346:307–316, 2014.

[17] G. Comanducci, F. Ubertini, and A. L. Materazzi. Structural health monitoring of suspension bridges with features affected by changing wind speed. *J Wind Eng Ind Aerodyn*, 141:12–26, 2015.

[18] A. Curtis, P. Gerstoft, H. Sato, R. Snieder, and K. Wapenaar. Seismic interferometry - turning noise into signal. *The Leading Edge*, 25:1082–1092, 2006.

[19] U. Dackermann, W.A. Smith, and R.B. Randall. Damage identification based on response-only measurements using cepstrum analysis and artificial neural networks. *Struct Health Monit*, 13:430–444, 2014.

[20] E. Daskalakis, C. P. Evangelidis, J. Garnier, N. S. Melis, G. Papanicolaou, and C. Tsogka. Robust seismic velocity change estimation using ambient noise recordings, 2016. arxiv:physics.geo-ph/160205695.

[21] A Deraemaeker, Reynders E., G De Roeck, and J Kullaa. Vibration-based structural health monitoring using output-only measurements under changing environment. *Mech Syst Signal Proc*, 22(1):34 – 56, 2008.

[22] N. Dervilis, K. Worden, and E.J. Cross. On robust regression analysis as a means of exploring environmental and operational conditions for shm data. *Journal of Sound and Vibration*, 347:279 – 296, 2015.

[23] 2009 Dirk-Jan Kroon. Accurate fast marching.

[24] Z. Duputel, V. Ferrazzini, F. Brenguier, N. Shapiro, M. Campillo, and A. Nercessian. Real time monitoring of relative velocity changes using ambient seismic noise at the Piton de la Fournaise volcano (La Réunion) from January 2006 to June 2007. *J. of Volcanology and Geothermal Res.*, 184:164–173, 2009.

[25] Z. Duputel, V. Ferrazzini, F. Brenguier, N. Shapiro, M. Campillo, and A. Nercessian. Real time monitoring of relative velocity changes using ambient seismic noise at the Piton de la Fournaise volcano (La Réunion) from January 2006 to June 2007. *J. of Volcanology and Geothermal Res.*, 184:164–173, 2009.

[26] C. P. Evangelidis and N. S. Melis. Ambient Noise Levels in Greece as Recorded at the Hellenic Unified Seismic Network. *Bull. Seismol. Soc. Am.*, 102(6):2507–2517, 2012.

[27] Charles R. Farrar and Keith Worden. *Structural Health Monitoring: A Machine Learning Perspective*. John Wiley & Sons, Ltd, 2012.

[28] CR Farrar and K Worden. An introduction to structural health monitoring. *Phil. Trans. R. Soc. As.*, 365(1851):303–315, 2007.

[29] J. Garnier and G. Papanicolaou. Passive sensor imaging using cross correlations of noisy signals in a scattering medium. *SIAM J. Imaging Sciences*, 2:396–437, 2009.

[30] J. Garnier and G. Papanicolaou. Resolution analysis for imaging with noise. *Inverse Problems*, 26:074001, 2010.

[31] J. Garnier and G. Papanicolaou. Role of scattering in virtual source imaging. *SIAM J. Imaging Sci.*, 7:1210–1236, 2014.

[32] J. Garnier, G. Papanicolaou, A. Semin, and C. Tsogka. Signal-to-noise ratio estimation in passive correlation-based imaging. *SIAM Imaging Science*, 6:1092–1110, 2013.

[33] J. Garnier and G. Papanicoloau. *Passive Imaging with Ambient Noise*. Cambridge University Press, 2016.

[34] Carmelo Gentile, Antonella Saisi, and Alessandro Cabboi. Structural identification of a masonry tower based on operational modal analysis. *Int J Archit Herit*, 9(2):98–110, 2015.

[35] P. Gouédard, L. Stehly, F. Brenguier, M. Campillo, Y. Colin de Verdière, E. Larose, L. Margerin, P. Roux, F. J. Sánchez-Sesma, N. M. Shapiro, and R. L. Weaver. Cross-correlation of random fields: mathematical approach and applications. *Geophysical Prospecting*, 56:375–393, 2008.

[36] Pierre Gouedard, Huajian Yao, Fabian Ernst, and Robert D. van der Hilst. Surface wave eikonal tomography in heterogeneous media using exploration data. *Geophysical Journal International*, 2012.

[37] A. Grêt, R. Snieder, R. C. Aster, and P. R. Kyle. Monitoring rapid temporal change in a volcano with coda wave interferometry. *Geophys. Res. Lett.*, 32(L06304), 2005.

[38] C. Hadziioannou, E. Larose, A. Baig, P. Roux, and M. Campillo. Improving temporal resolution in ambient noise monitoring of seismic wave speed. *Journal of Geophysical Research: Solid Earth*, 116(B7):2156–2202, 2011.

[39] Céline Hadziioannou, Eric Larose, Olivier Coutant, Philippe Roux, and Michel Campillo. Stability of monitoring weak changes in multiply scattering media with ambient noise correlation: Laboratory experiments. *J of the Acoustical Soc of America*, 125(3688), 2009.

[40] Salvador Ivorra and Francisco J. Pallarés. Dynamic investigations on a masonry bell tower. *Eng Struct*, 28(5):660 – 667, 2006.

[41] K.I. Konstantinou, C.P. Evangelidis, W.-T. Liang, N.S. Melis, and I. Kalogeras. Seismicity, vp/vs and shear wave anisotropy variations during the 2011 unrest at Santorini caldera, southern Aegean. *Journal of Volcanology and Geothermal Research*, 267(0):57 – 67, 2013.

[42] E. Lagios, V. Sakkas, F. Novali, F. Bellotti, A. Ferretti, K. Vlachou, and V. Dietrich. Squeesar™ and {GPS} ground deformation monitoring of Santorini volcano (1992–2012): Tectonic implications. *Tectonophysics*, 594(0):38 – 59, 2013.

[43] F.-C. Lin, M.H. Ritwoller, and R. Snieder. Eikonal tomography: surface wave tomography by phase front tracking across a regional broad-band seismic array. *Geophys. J. Int.*, 177:1091–1110, 2009.

[44] F Magalhães, A Cunha, and E Caetano. Dynamic monitoring of a long span arch bridge. *Eng. Struct.*, 30(11):3034 – 3044, 2008.

[45] F. Magalhães, A. Cunha, and E. Caetano. Vibration based structural health monitoring of an arch bridge: From automated oma to damage detection. *Mech Syst Signal Proc*, 28:212 – 228, 2012.

[46] Filipe Magalhães, Alvaro Cunha, and Elsa Caetano. Online automatic identification of the modal parameters of a long span arch bridge. *Mech Syst Signal Proc*, 23(2):316 – 329, 2009.

[47] Ueli Meier, Nikolai M. Shapiro, and Florent Brenguier. Detecting seasonal variations in seismic velocities within los angeles basin from correlations of ambient seismic noise. *Geophysical Journal International*, 181(2):985–996, 2010.

[48] AAi Mosavi, D Dickey, R Seracino, and S Rizkalla. Identifying damage locations under ambient vibrations utilizing vector autoregressive models and mahalanobis distances. *Mech Syst Signal Proc*, 26:254 – 267, 2012.

[49] L.E. Mujica, J. Rodellar, A. Fernandez, and A. Guemes. Q-statistic and t2-statistic pca-based measures for damage assessment in structures. *Structural Health Monitoring*, pages 539–553, 2010.

[50] Andrew V. Newman, Stathis Stiros, Lujia Feng, Panos Psimoulis, Fanis Moschas, Vasso Saltogianni, Yan Jiang, Costas Papazachos, Dimitris Panagiotopoulos, Eleni Karagianni, and Domenikos Vamvakaris. Recent geodetic unrest at Santorini caldera, Greece. *Geophysical Research Letters*, 39(6):n/a–n/a, 2012.

[51] Van Overschee and De Moor. *Subspace Identification for Linear Systems: Theory - Implementation - Applications*. Kluwer Academic Publishers, 1996.

[52] G. Poupinet, W. Ellsworth, and J. Frechet. Monitoring velocity variations in the crust using earthquake doublets: An application to the calaveras fault, california. *J. Geophys. Res.*, 89(B7):5719–5731, 1984.

[53] G. A. Prieto, M. Denolle, J. F. Lawrence, and G. C. Beroza. On amplitude information carried by the ambient seismic field. *Comptes Rendus Geoscience*, 343:600–614, 2011.

[54] G. A. Prieto, J. F. Lawrence, Chung A. I, and M. D. Kohler. Impulse response of civil structures from ambient noise analysis. *B.S.S.A*, 100(5A):2322–2328, 2010.

[55] L.F. Ramos, L. Marques, P.B. Lourenço, G. DeRoeck, A. Campos-Costa, and J. Roque. Monitoring historical masonry structures with operational modal analysis: two case studies. *Mech Syst Signal Proc*, 24:1291–1305, 2010.

[56] A. Ratdomopurbo and G. Poupinet. Monitoring a temporal change of seismic velocity in a volcano: application to the 1992 eruption of mt. merapi (indonesia). *Geophys Res Lett.*, 22(7):775–778, 1995.

[57] Edwin Reynders, Jeroen Houbrechts, and Guido De Roeck. Fully automated (operational) modal analysis. *Mechanical Systems and Signal Processing*, 29:228 – 250, 2012.

[58] V. Saltogianni, S. C. Stiros, A. V. Newman, K. Flanagan, and F. Moschas. Time-space modeling of the dynamics of Santorini volcano (Greece) during the 2011–2012 unrest. *J. Geophys. Res. Solid Earth*, 119:8517–8537, 2014.

[59] G. T. Schuster. *Seismic interferometry*. Cambridge University Press, Cambridge, 2009.

[60] N. M. Shapiro, M. Campillo, L. Stehly, and M. Ritzwoller. High resolution surface wave tomography from ambient seismic noise. *Science*, 307:1615–1618, 2005.

[61] Nikolai M. Shapiro and Michel Campillo. Emergence of broadband Rayleigh waves from correlations of the ambient seismic noise. *Geophys. Res. Lett.*, 31:L07614, 2004.

[62] R. Snieder. Extracting the Green's function from the correlation of coda waves : a derivation based on stationary phase. *Phys. Rev. E*, 69:046610, 2005.

[63] R. Snieder and K. Wapenaar. Imaging with ambient noise. *Physics Today*, 307:1615—1618, 2010.

[64] R. Snieder, K. Wapenar, and U. Wegler. Unified Green's function retrieval by cross-correlation; connection with energy principles. *Phys. Rev. E*, 75:036103, 2007.

[65] Inc. The MathWorks. *MATLAB R2012a*. Natick, Massachusetts, United States, 2012.

[66] F Ubertini, G Comanducci, and N Cavalagli. Vibration-based shm of a historic bell-tower using output-only measurements and multivariate statistical analysis. *Struct Health Monit*, in press, 2016.

[67] F. Ubertini, C. Gentile, and A.L. Materazzi. Automated modal identification in operational conditions and its application to bridges. *Eng Struct*, 46:264–278, 2013.

[68] K. Wapenaar, D. Draganov, R. Snieder, X. Campman, and A. Verdel. Tutorial on seismic interferometry: Part 1 - basic principles and applications. *Geophysics*, 75:A195–A227, 2010.

[69] K. Wapenaar, E. Slob, R. Snieder, and A. Curtis. Tutorial on seismic interferometry: Part 2 - underlying theory and new advances. *Geophysics*, 75:A211–A227, 2010.

[70] R. L. Weaver, C. Hadziioannou, E. Larose, and M Campillo. On the precision of noise correlation interferometry. *Geophysical Journal International*, 185(3):1384–1392, 2011.

[71] Richard Weaver, Berenice Froment, and Michel Campillo. On the correlation of non-isotropically distributed ballistic scalar diffuse waves. *J. Acoust. Soc. Am.*, 136(4):1817–1826, 2009.

[72] R.L. Weaver and O.I. Lobkis. Ultrasonics without a source : thermal fluctuation correlations at MHz frequencies. *Phys. Rev. Lett.*, 87(13):134301, 2001.

[73] K Worden, H Sohn, and CR Farrar. Novelty detection in a changing environment: regression and interpolation approaches. *J Sound Vib*, 258(4):741 – 761, 2002.

[74] AM Yan, G Kerschen, P. De Boe, and JC Golinval. Structural damage diagnosis under varying environmental conditions part i: a linear analysis. *Mech Syst Signal Proc*, 19(4):847 – 864, 2005.

[75] AM Yan, G Kerschen, P De Boe, and JC Golinval. Structural damage diagnosis under varying environmental conditions part ii: local pca for non-linear cases. *Mech Syst Signal Proc*, 19(4):865 – 880, 2005.

[76] Z. Zhan, V.C. Tsai, and R.W. Clayton. Spurious velocity changes caused by temporal variations in ambient noise frequency content. *Geophys. J. Int.*, 194:1574–1581, 2013.